Chem. Rev. **2005,** *105,* 2279−2328

Theoretical Perspective on the Structure and Mechanism of Cytochrome P450 Enzymes[†]

Sason Shaik,*[,‡] Devesh Kumar,[‡] Samuël P. de Visser,*[,§] Ahmet Altun,[||] and Walter Thiel*[,||]

Department of Organic Chemistry and the Lise-Meitner-Minerva Center for Computational Quantum Chemistry, The Hebrew University of Jerusalem, 91904 Jerusalem, Israel, School of Chemical Engineering and Analytical Science, The University of Manchester, P.O. Box 88, Sackville Street, Manchester M60 1QD, United Kingdom, and Max-Planck-Institut für Kohlenforschung, Kaiser-Wilhelm-Platz 1, D-45470 Mülheim an der Ruhr, Germany

Received October 11, 2004

Contents

1. Introduction

Cytochrome P450 is one of the most versatile enzymes in nature.[1] It uses dioxygen and two reducing equivalents to catalyze a great variety of stereospecific and regioselective oxygen insertion processes into organic compounds.[2−16] These processes are of vital importance in biosystems, where the enzyme participates in detoxification and biosynthe-

---

[†] This review is dedicated to Bernard Meunier, a prominent organometallic and P450 chemist, on the occasion of his election as President of the CNRS.

* To whom correspondence should be addressed. S.S.: phone, +972-2-6585909; fax, +972-2-6584680/6585345; e-mail, sason@yfaat.ch.huji.ac.il. S.P.V. e-mail, sam.devisser@manchester.ac.uk. W.T.: e-mail, thiel@mpi-muelheim.mpg.de.

[‡] The Hebrew University of Jerusalem.

[§] The University of Manchester.

[||] Max-Planck-Institut für Kohlenforschung.

10.1021/cr030722j CCC: $53.50

Sason Shaik was born in 1948 in Iraq. The family immigrated to Israel in the Exodus of the Iraqi Jewry. He received his B.Sc. and M.Sc. degrees in Chemistry from Bar-Ilan University and Ph.D. degree from the University of Washington under Nicholaos D. Epiotis. In 1978/9 he spent a postdoctoral year with Roald Hoffmann at Cornell University. In 1980 he started his first academic position as a Lecturer at Ben-Gurion University, where he became Professor in 1988. He subsequently moved to the Hebrew University, where he is currently Director of The Lise Meitner-Minerva Center for Computational Quantum Chemistry. Among the awards he has received are the Lise-Meitner-Alexander von Humboldt Senior Award in 1996–1999, the 2001 Israel Chemical Society Prize, and the 2001 Kolthoff Award. His research interests are in the use of quantum chemistry and, in particular, valence-bond theory to develop paradigms which can pattern data and lead to the generation and solution of new problems. He started his P450 research in 1998 and has been fascinated ever since!

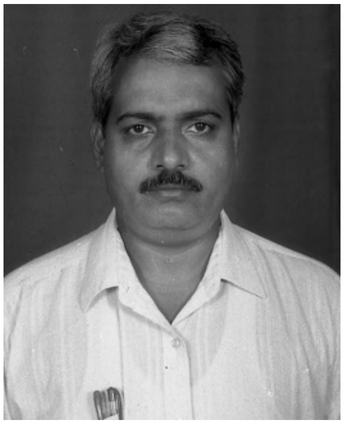

Devesh Kumar was born in India in 1965. He received his B.Sc. degree from the L. N. Mithla University and M.Sc. and Ph.D. degrees in Physics from the D. D. U. Gorakhpur University, India. He worked at the Centre for Liquid Crystal Research and Education, Nagarjuna University, India as a research associate (from July 2001 to March 2002) before joining Professor Sason Shaik at the Hebrew University of Jerusalem as a postdoctoral fellow in May 2002. His main research interests are theoretical studies of conformations and interactions of mesogens and enzyme catalysis.

Sam de Visser was born in The Netherlands in 1968. He received his B.Sc. degree from the College of Zeeland and M.Sc. and Ph.D. degrees from the University of Amsterdam (The Netherlands) in Organic Mass Spectrometry. Thereafter, he moved to the field of Theoretical Chemistry and performed postdoctoral research with Professor Michael A. Robb at King's College London (1997–1999) and Professor Sason Shaik at the Hebrew University of Jerusalem (1999–2004). He then moved to the United Kingdom, where he obtained a Lectureship position at the School of Chemical Engineering and Analytical Science of the University of Manchester. He is the recipient of a Ramsay Memorial Fellowship (1997, 1998) of the Royal Netherlands Academy of Arts and Sciences and won the Lise-Meitner-Minerva Junior Award (2003). His main research interests are theoretical studies of enzyme catalysis.

Ahmet Altun was born in Turkey in 1975. He received his B.Sc. (1996), M.Sc. (1999), and Ph.D (2003) degrees in Physics from Dokuz Eylül University (Izmir), Fatih University (Istanbul), and Gebze Institute of Technology (Izmit), respectively. He worked at Fatih University as a research assistant (1997–2003) before joining Professor Walter Thiel's theory group at the Max-Planck-Institut für Kohlenforschung as a postdoctoral fellow in 2003. His research interests include quantum-chemical calculations for QSAR, pharmacophore identification and pharmacophore-based bioactivity prediction, spectral parameters of organic and inorganic compounds, and enzymatic reactions catalyzed by metalloproteins. He is also experienced in synthesis and thermal and spectral characterization of transition-metal complexes. Currently, he is active in QM and QM/MM studies on cytochrome $P450_{cam}$.

sis. Furthermore, its drug metabolism and involvement in brain chemistry (after brain trauma) make this enzyme a target for the drug industry and biomedical research.[16−18] Finally, since activation of inert C−H bonds is a Holy Grail of chemistry,[19] the facility with which P450s carry out this process makes this enzyme superfamily a model for creative mimetic chemistry[20] designed to generate powerful and robust catalysts that can perform C−H activation. With all these features it is no wonder that the area has become a very active arena of research that led to important insights and generated lively debates over the nature of the various species of the enzyme and their reactivity patterns. Many of the experimental-mechanistic and structural aspects have been covered in a recent *Chemical Reviews* paper,[21] two monographs,[1] and a variety of other reviews.[2−16] The interested readers may consult these sources as well as a web site dedicated to these enzymes.[22]

Figure 1 shows a snapshot of $P450_{cam}$, a bacterial enzyme that hydroxylates camphor, with the camphor molecule placed over the active species of the

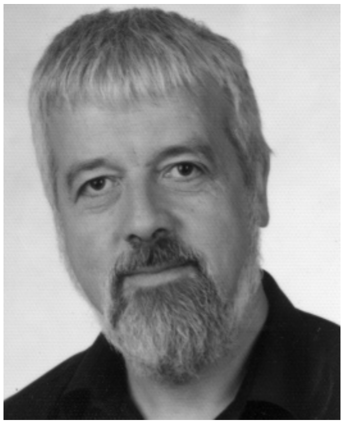

Walter Thiel was born in Treysa, Germany, in 1949. He studied chemistry at the University of Marburg and received his Ph.D. degree in 1973. After two postdoctoral years at the University of Texas at Austin with Michael Dewar he returned to Marburg and obtained the Habilitation in 1981. He was Professor at the University of Wuppertal from 1983 to 1992, Visiting Professor at the University of California at Berkeley in 1987, and Full Professor of Chemistry at the University of Zürich from 1992 to 1999. He is now Director at the Max-Planck-Institut für Kohlenforschung in Mülheim an der Ruhr and affiliated with the University of Düsseldorf as an Honorary Professor. He received the Heisenberg Fellowship in 1982, the Alfried-Krupp-Award in 1988, and the WATOC Schrödinger Medal in 2002. His research area is theoretical and computational chemistry, both method development and applications.

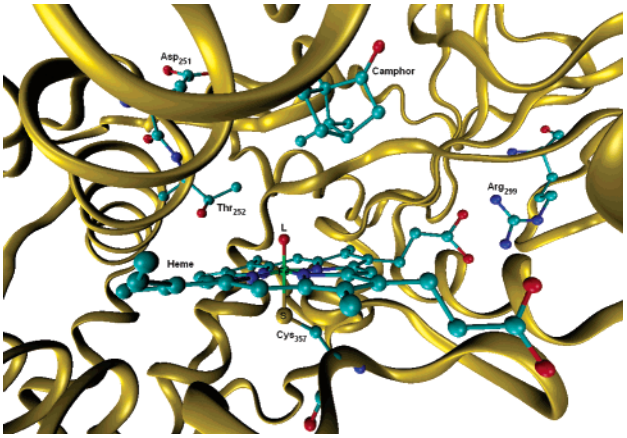

Figure 1. Close-up of the active site of P450$_{cam}$ as taken from the X-ray structure (pdb code: 1DZ9) of Schlichting et al.[28] with some essential groups highlighted.

enzyme. In most P450 enzyme forms (isoforms) the active species and the substrate are accommodated within the same protein pocket that sometimes possesses a special substrate binding machinery.[23] There are some structural features that are common to all P450 isoforms. The active species of the enzyme is an iron ion ligated to a protoporphyrin IX macrocycle and two additional axial ligands: one, called proximal, is a thiolate from a cysteinate (Cys$_{357}$) side residue of the protein, and the other, called distal, is a variable ligand, labeled as L in Figure 1. The distal ligand L changes during the catalytic cycle of the enzyme and thereby activates the enzyme's main function. When the distal ligand becomes an oxo group and the porphyrin a radical cation, the species is called Compound I (Cpd I). Cpd I has not been observed experimentally in the cycle of cytochromes P450 but is generally accepted to be the reactive species of the enzyme and one of the most potent oxidants known in Nature; it specializes in [O]-insertion into a great number of nonactivated bonds of organic molecules. The residues labeled as Asp$_{251}$ (aspartate) and Thr$_{252}$ (threonine), in Figure 1, play a key role in the conversion of the initial form of the enzyme to Cpd I by activating a protonation machinery that transforms the dioxygen molecule to the oxo ligand. Hydrogen bonds between Cys$_{357}$ and the neighboring residues are essential for fine-tuning the properties of Cpd I. Two arginine residues that form salt bridges with the propionate side chains of the porphyrin (Figure 1 shows only one of them, Arg$_{299}$) may also affect the reactivity of Cpd I. Having such structural information available[14,24−28] is an important prerequisite for the theoretical studies on cytochrome P450 that are described in the present review.

A great deal has happened in theory since the pioneering quantum mechanical (QM) calculations of P450-related species[29−31] using semiempirical and ab initio techniques. Since then, advances in density functional theory (DFT) have provided improved computational methods that combine reasonable accuracy with speed. More recently, such treatments have been interfaced with molecular mechanical (MM) approaches, leading to hybrid quantum mechanical/molecular mechanical [QM(DFT)/MM] methods that enable one to study the active species in their native protein environment.[32] All these developments have had a considerable impact on the field and led to an ever-growing surge of theoretical activity. It was therefore deemed timely to review the theoretical results and insights provided by these methods. Some of the material covered in previous reviews[18,21,33−37] is included here too in order to create a unified survey. We start with a brief summary of the available theoretical methods (section 2) and then describe the various species in the catalytic cycle (section 3) and the principal mechanisms by which the enzyme transfers oxygen to organic compounds (section 4).

2. Theoretical Methods

Theoretical chemistry offers a hierarchy of methods for calculating potential-energy surfaces (PES) ranging from accurate ab initio approaches to simple classical force fields. The QM methods provide electronic structure information and can be applied to the study of complete reaction pathways. The MM methods disregard the electrons and employ empirical potential-energy functions that refer to a given molecular topology, and they are therefore suitable for studying related structures such as conformers but not for chemical reactions.[38] Among the QM methods one distinguishes ab initio, density functional, and semiempirical approaches which differ in philosophy, accuracy, and computational speed (see below). As a crude generalization, there is an inverse relationship between the speed of a method and its reliability/accuracy, such that the ab initio methods, which are the most time consuming, are generally the most accurate while MM methods are the fastest and also the least accurate.

Ab initio QM methods aim at the solution of the Schrödinger equation and thus focus on the wave function of the system. After selecting the level of ab initio theory to be applied and the one-electron basis set for representing the wave function, everything else is calculated from scratch. The lowest ab initio level, Hartree–Fock (HF) theory, describes the *N*-electron wave function by a single determinant built from the occupied orbitals, which are variationally determined by minimizing the energy. HF calculations do not incorporate electron correlation and are therefore normally not adequate for transition-metal compounds. If the HF determinant can still represent the electronic structure in a qualitative sense, single-reference treatments of electron correlation may be sufficient, the preferred choice being CCSD(T) (coupled cluster theory with single and double excitations and perturbative triple excitations). In more complicated cases, multireference approaches are necessary, such as the complete active space self-consistent field (CASSCF) method and its augmentation by second-order perturbation theory (CASPT2) or multireference configuration interaction (MRCI). Unfortunately, CCSD(T), CASSCF, CASPT2, and MRCI calculations are generally too demanding for P450 species, especially if one wishes to optimize geometries of such large molecules or study their potential-energy surfaces for a given reaction. Very few calculations at these levels exist for P450 or related heme species.[30,31,39,40] A recent short review provides a state-of-the-art discussion of the application of these methods to transition-metal and enzymatic complexes.[41]

In DFT methods the electron density plays the central role because the energy and all molecular properties are derived from the density. In the Kohn–Sham (KS) formalism an auxiliary wave function is used to obtain the electron density. Even though this auxiliary wave function has a single-determinantal form, the corresponding energy expression incorporates electron correlation through the exchange-correlation terms. Consequently, the computational effort for DFT is much smaller than for correlated ab initio treatments and actually quite similar to HF theory, but the accuracy of DFT is much better than that of HF and sometimes even competitive with the CASPT2 method.[41–43] Currently, DFT calculations are easily possible for systems up to 100 atoms, and one can thus investigate the potential-energy surfaces of models of enzymatic reactions in considerable detail and with good accuracy.

DFT applications require the choice of a suitable exchange-correlation functional and one-electron basis set. There is a myriad of functionals available, ranging from the local functionals (LDA, local density approximation) via gradient-corrected functionals (GGA, generalized gradient approximation) and hybrid functionals (with admixture of HF exchange) to more advanced forms. Some of these functionals are derived from first principles and are thus parameter free, while others involve a semiempirical calibration against theoretical or experimental reference data. In practice, gradient-corrected functionals such as BP86, BLYP, and BPW91 are often applied and considered suitable also for enzymatic species, but the preferred choice are hybrid functionals such as B3LYP or B3PW91.[41,42] In particular, B3LYP is quite successful in reproducing experimental enthalpies of formation with mean absolute deviations of 3 kcal mol^{-1} for the G2/97 test set and 4–5 kcal mol^{-1} for the larger G3/99 test set.[44] B3LYP also performs well for a number of other properties,[45] although reaction barriers are often rather difficult to reproduce. Thus, even though B3LYP is generally considered to be the preferred DFT approach for carrying out biological and P450-related research,[41,42] one must not be too enamored with the numerical results and treat the absolute values of barriers with some caution. For open-shell species one has the choice between the restricted (ROB3LYP) and the more general unrestricted (UB3LYP) approach. There are general arguments that favor an unrestricted Kohn–Sham (UKS) treatment,[46] which has the added advantage that it can be applied to high-spin and low-spin situations while some ROKS implementations are restricted to the high-spin case.

Semiempirical QM methods are based on wave mechanics, but many of the terms appearing in the ab initio QM formalism are neglected to speed up the calculations. In an attempt to compensate for the resulting errors, most of the remaining terms are not calculated analytically but taken from experiment or calibrated against reliable experimental or theoretical data. For organic and main-group compounds there exist well-established semiempirical methods such as MNDO, AM1, and PM3, which combine computational speed with reasonable accuracy. For transition-metal compounds with their more demanding electronic structure and for iron, in particular, successful general-purpose parametrizations have not yet been developed, however, and one must therefore resort to system-specific parametrizations for P450-related work; this strategy has been followed in a recent PM3 study on iron complexes.[47] SAM1 is another less established semiempirical method that has been applied to compute the complete catalytic cycle in P450 model compounds; while providing some interesting insights, SAM1 apparently fails to describe the geometry and electronic structure of the critical Cpd I species.[48] The INDO/S method mainly targets electronically excited states and has been used to characterize some P450 intermediates, e.g., with regard to their multiplet splittings.[49] In view of their limited accuracy, we will not attempt full coverage of semiempirical studies in P450 research, although we may occasionally mention some pertinent results.

MM force-field methods express the total energy of a molecular system as a sum of bonded energy terms, electrostatic terms, and van der Waals interactions. The bonded energy terms normally consist of harmonic stretching and bonding potentials and periodic torsion potentials; they contain equilibrium geometry parameters and force constant parameters that are determined from experimental data for all relevant atom and bond types that occur in the molecules of interest.[38] The nonbonded electrostatic interactions involve classical electrostatics; for proteins, usually the partial charges are kept fixed during the calculations. The van der Waals interactions are normally represented by a Lennard–Jones potential with attractive $1/r^6$ and repulsive $1/r^{12}$ terms. Since MM calculations are cheap, they can be used to run molecular dynamics (MD) simulations to study multiple conformations, sample an entire potential-energy surface, and determine free energies. They require modest resources and hence can be applied to large systems, such as an entire enzyme, and they have been used in P450 research, for instance, to explore the entrance and exit channels of substrates/products into an enzyme,[50–54] the preferred location of substrate binding,[55,56] and the dynamics of large substrates within the pocket.[57]

The QM/MM method[32,58,59] combines the advantages of QM and MM approaches; the practical choice for P450 and similar metalloenzymes uses DFT for the QM region, hence DFT/MM. In QM/MM calculations the system is divided into two subsystems. The smaller subsystem involves the electronically important part (i.e., the active species) that is computed with a QM method. The larger subsystem comprises the protein/solvent environment, which is treated classically by any of the established MM force fields. There are several strategies for handling the interactions between the QM and MM subsystems[60] ranging from simple mechanical to electronic and polarized embedding schemes. In the case of the polar protein environment, an electronic embedding is generally considered necessary, so that the QM/MM interactions involve electrostatic and van der Waals terms. The electrostatic interactions are incorporated into the QM calculations by including the MM charges into the QM Hamiltonian, so that the QM subsystem is polarized in response to the electric field and hydrogen-bonding machinery of the protein environment. The van der Waals QM/MM interactions are treated classically, normally using standard MM parameters for the QM atoms, although it is considered legitimate to re-optimize these parameters to achieve some fine-tuning.[61] Another critical feature in QM/MM approaches is the treatment of the boundary in cases where the QM/MM division requires cutting through covalent bonds, as in P450 enzymes.[62] Again, there are several options for dealing with the problems caused by such cuts. The most common approach is to satisfy the valency at the dangling bond by a link atom, typically hydrogen,[59,63] but it is also possible to use specifically parametrized boundary atoms,[64] pseudobonds,[65] or frozen orbitals.[66–69] For any of these options one needs to be careful with the treatment of electrostatics at the QM/MM boundary.[70–72] In practice, the link atom approach is currently dominant, and its results have been judged to be the best,[62] although the available alternatives also work well if proper care is exercised.[71,73]

Different QM/MM calculations may differ in the choice of QM and MM methods, in the treatment of the QM/MM interactions and the QM/MM boundary (see above), and also in the techniques used for exploring the potential-energy surface. In studies of enzymatic reactions, one would ideally like to perform a proper sampling of configurational space in order to derive free-energy quantities, but this is currently only affordable with semiempirical QM/MM approaches and not with the computationally more demanding DFT/MM methods. Therefore, DFT/MM investigations of enzymatic reactions normally involve geometry optimizations along appropriately chosen reaction paths, followed by a more precise location of the relevant stationary points; special optimization techniques are available for this purpose.[74] This procedure leads to representative structures for reactants, transition states, and products, but it is clear that many such structures will exist in an enzyme which will differ in the detailed conformation of the protein/solvent environment. In the absence of proper sampling, one may get an idea of the corresponding variations by performing several such optimizations starting from different initial geometries. One obvious starting point for minimization is the experimental X-ray structure. Others may be generated by following standard classical biomolecular simulation protocols that start from the experimental X-ray structure and involve an initial equilibration of the system followed by a classical MD run from which suitable snapshots are selected as starting points for DFT/MM optimizations. In current practice, up to about five snapshots are normally studied. In this connection one should be aware of several other technical issues in the setup of the DFT/MM calculations that may influence the results obtained: these include the size of the overall system studied (only part of the enzyme or full enzyme with or without surrounding water layer), the size of the QM region (minimal active region or inclusion of side chains and neighboring residues), the size of the region that is optimized (outer part of the system normally fixed), the presence of water molecules and counterions within the protein (number and location), the treatment of charged residues at the surface of the protein (neutralized or screened by surrounding solvent), and the protonation state of ionizable residues such as aspartic and glutamic acid or histidine (assigned by standard empirical rules or by visual inspection or by explicit $\mathrm{p}K_\mathrm{a}$ calculations, e.g., of Poisson–Boltzmann type[75]). It should be emphasized that most of these issues are relevant not only for QM/MM optimizations but also for QM/MM sampling techniques that aim at free-energy results. This long list of technical issues indicates that there are no routine “black-box” procedures for QM/MM calculations and that great care is needed to perform QM/MM studies on enzymatic reactions and assess the results from different QM/MM approaches. As experience accumulates in the QM/MM community, it is anticipated that standard canonical procedures will evolve and be generally accepted. However, compared with QM studies on small gas-phase molecules, QM/MM work on enzymes will remain more taxing because of the sheer complexity of enzymes.

2.1. Notations and Abbreviations

DFT methods are not very sensitive to the quality of the basis set, and a double-ζ (DZ) basis set gives

Scheme 1. Different Model Systems and Their Abbreviations

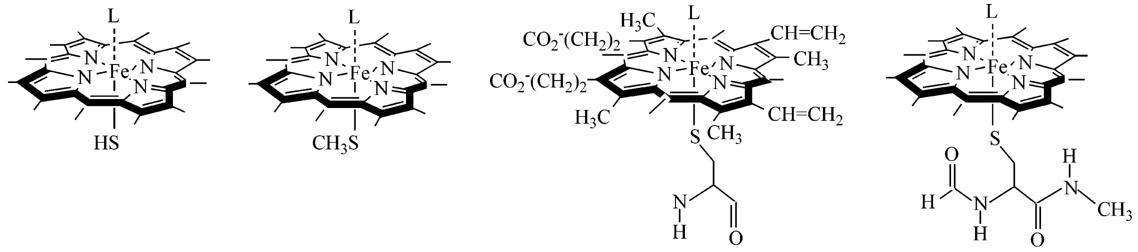

Por,SH Por,SMe PPIX,SCys Por,ext-SCys

already qualitatively correct results. The Jerusalem group (S.S., D.K., and S.P.D.V.) has successfully used such a double-ζ basis set, describing iron by an effective core potential and the LACVP basis[76,77] and the other atoms by the 6-31G basis, hence, LACVP-(Fe),6-31G(H,C,N,O,S) or LACVP-DZ in a simpler notation. The label DFT(B3LYP)/LACVP-DZ will thus refer to a B3LYP calculation with the LACVP-(Fe),6-31G(H,C,N,O,S) basis set. Larger basis sets will be either denoted in this type of terminology, e.g., TZ (triple ζ), or specified explicitly. QM/MM methods based on DFT will be labeled as DFT(functional)/MM, with the chosen functional given in parentheses, e.g., B3LYP or BP86. Restricted B3LYP calculations of open-shell systems will be denoted as ROB3LYP, while we will refer to unrestricted UB3LYP treatments simply by B3LYP.

2.2. Coverage, Sources of Computational Results, and Models of the Enzyme

Most of the older theoretical literature on P450 up to the year 2000 can be found in the reviews of Loew and Harris[33] and Loew;[78] these data are summarized here only briefly. The complete catalytic cycle of P450 was modeled by Rydberg et al.,[79] Shaik et al.,[37,80,81] and Hata et al.[82] using unrestricted B3LYP. Rydberg et al.[79] also calculated the species appearing in the catalytic cycles of horseradish peroxidase and catalase models with various axial ligands, but these are beyond the scope of this review. QM/MM studies of several species in the cycle of P450$_{\mathrm{cam}}$ as well as of the mechanisms of protonation and C−H hydroxylation during the cycle were carried out by the Mülheim and Jerusalem groups,[83−88] who used DFT-(B3LYP)/MM with the ChemShell program.[72] Related QM/MM work was reported by Guallar et al.,[89,90] who employed the DFT(ROB3LYP)/MM method.[68,69] Several groups have extensively studied reaction mechanisms of P450 models by means of B3LYP calculations. C−H hydroxylation for a variety of substrates was investigated mostly by the Jerusalem group[91−98] and by Yoshizawa et al.[99−105] Double-bond epoxidation was addressed by de Visser et al.[93,94,106−108] and Kamachi et al.[105] Benzene hydroxylation was covered by two groups,[109,110] and sulfoxidation was studied by Sharma et al.[111] These publications, and a few others, will form the basis for the discussion in the following sections.

Since the complete enzyme cannot be described by DFT, one usual practice among the workers in the field is to truncate the active species and calculate model systems. Generally, these models truncate the heme to porphine by removing all side chains of the protoporphyrin IX macrocycle. A less extensive truncation uses octamethyl porphyrin.[112] The cysteinate ligand is modeled either as thiolate (SH^-), methyl mercaptide (SCH_3^-), or cysteinate anion ($CysS^-$) and in some cases as an extended cysteinate (ext-SCys), augmented by the peptide bonds of the adjacent Leu$_{358}$ and Leu$_{356}$ residues. DFT(B3LYP)/MM calculations[83] showed that gas-phase calculations using SH^- give generally better agreement with the DFT/MM calculations than SCH_3^- or even the full cysteinate ligand. Many of the calculations reported below, especially those on reaction mechanisms, used the simplest model with porphine and SH^- as the thiolate ligand or porphine and SCH_3^-. The main model systems and their notations are summarized in Scheme 1.

3. Catalytic Cycle of P450 Enzymes

Cytochrome P450 is a nanomachine that operates by means of the catalytic cycle depicted in Figure 2.[113] The iron−heme group is shown only for **1**, whereas in the rest of the cycle the heme is depicted by two bold horizontal lines, and the cysteinate ligand is abbreviated as SCys. The cycle begins with the resting state (**1**) in which a water molecule is bound to the ferric ion in the distal side. In this hexacoordinated Fe^{III} complex the d-block orbitals of the iron contain five electrons, predominantly in the low-spin doublet configuration. The entrance of the substrate (for example, an alkane, AlkH) displaces the water molecule, leaving a pentacoordinated ferric−porphyrin (**2**). With a coordination number of five, the iron moves from a position almost in the plane of the heme to a position below the heme and becomes predominantly a sextet high-spin species. The ferric complex (**2**) is a slightly better electron acceptor than the resting state and can therefore take up an electron from a reductase protein, leading to a high-spin ferrous complex (**3**). Subsequent binding of molecular oxygen yields the ferrous dioxygen complex (**4**), which has a singlet spin state and is a good electron acceptor. This, in turn, triggers a second reduction of the system to generate the ferric−peroxo anion species (**5**). This second reduction is believed to be, though not always, the rate-determining step in the catalytic cycle.[114] Since the ferric peroxo complex (**5**) is a good Lewis base, it gets quickly protonated to form the ferric−hydroperoxide species (**6**) that is also called Cpd 0. The resulting Cpd 0 is still a good

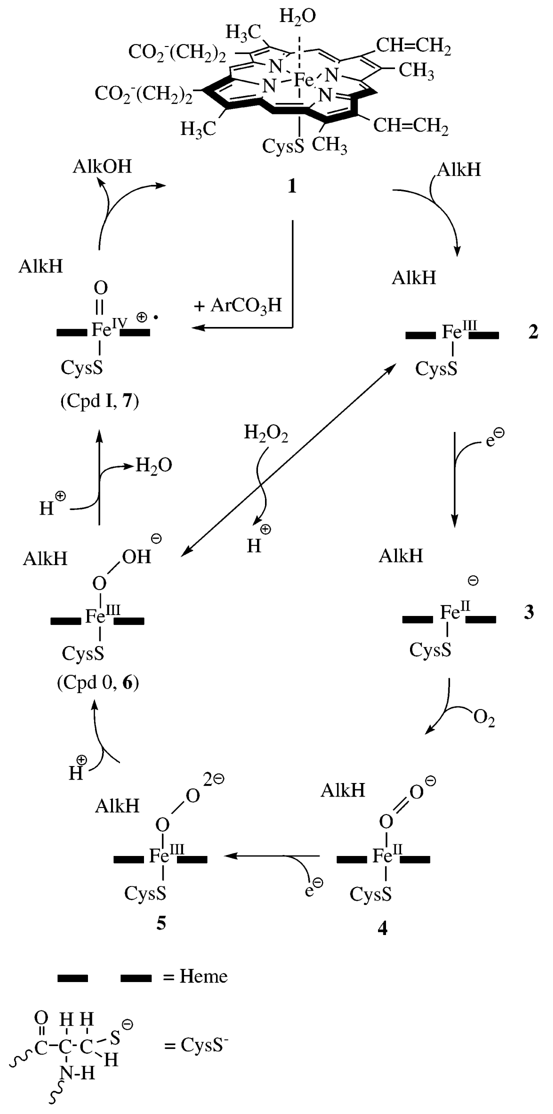

Figure 2. Schematic representation of the catalytic cycle of P450. (Reprinted with permission from ref 37. Copyright 2004 Kluwer Academic/Plenum Publisher.)

Lewis base and abstracts an additional proton to form Cpd I (**7**) and water. This species then transfers an oxygen atom to the substrate; in this case the alkane is converted thereby to an alcohol. After this catalytic reaction the alcohol exits the pocket, water molecules enter in, and the enzyme restores the resting state by binding a water molecule. There is uncertainty about the details of the cycle starting from **5** and onward back to **1**; *Cpd I is elusive, its protonation mechanism is still not fully characterized, and the mechanism of substrate oxidation is still highly debated*. Thus, theory has an important role here as a partner of experiment.

In brief, the efficiency of the catalytic cycle is dominated by a few key factors. First is the donor ability of the thiolate ligand, which is referred to as the "push" effect,[115] and seems to be crucial for the operation of the catalytic cycle. Second is the protonation and hydrogen-bonding machinery of the distal side that converts Cpd 0 into Cpd I and prevents the generation of hydrogen peroxide and other oxygen-wasting species (processes that result in a loss of the reducing equivalents, NADH or NADPH, are called "uncoupling" reactions). Third is the access of water molecules into the pocket, which needs to be well controlled. On one hand, water molecules seem to be important for protonation,[116] but on the other hand, too much water leads to uncoupling;[117,118] this will also be influenced by the tightness of substrate binding by the enzyme.[119] Finally, as shown in Figure 3, the interactions of the three amidic groups of Gln$_{360}$, Gly$_{359}$, and Leu$_{358}$ with the sulfur atom of the cysteinate ligand (only one of these has the geometry of a classical hydrogen bond) and also of Gln$_{360}$ to the carbonyl group of the cysteine[24,28] appear to be essential for the stability and activity of the enzyme.[120,121] These features are addressed in the next subsections that summarize the theoretical studies of the different species in the catalytic cycle (structures **1**−**7**).

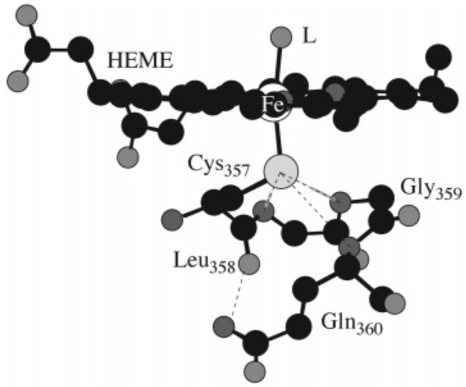

Figure 3. Hydrogen-bonding-type interactions of the cysteine ligand in P450.

3.1. d-Block and Key Orbitals of Species in the Catalytic Cycle

All the species in the cycle, Figure 2, possess a dense orbital manifold and hence many closely lying spin and electromeric states. It is, therefore, important to begin with an orbital picture of these P450 species. Figure 4 shows high-lying occupied and low-lying virtual orbitals of several key species in the catalytic cycle. Since Cpd I (**7**) is involved in the reactivity, we begin on top of the figure with its orbitals; on the left-hand side we show the five metal d-type orbitals, in the center, a high-lying mixed porphyrin−thiolate orbital, and a typical ligand lone-pair orbital on the right-hand side. The d-block is split into the characteristic three-below-two sets, which are nascent from the purely octahedral t_{2g} and e_g sets with an additional splitting of t_{2g} into one-below-two. The lowest three orbitals are, in increasing energy order, the nonbonding $\delta(d_{x^2-y^2})$ orbital and the two π^*_{FeO} (π^*_{xz} and π^*_{yz}) orbitals; the latter two involve antibonding interactions between the metal $3d_{xz,yz}$ and the $2p_{x,y}$ atomic orbitals on oxygen. The two high-lying virtual orbitals of Cpd I are σ^* orbitals; one (σ^*_{xy}) describes the Fe−N antibonding interactions and the other ($\sigma^*_{z^2}$) those along the O−Fe−S axis. In species where only one oxygen orbital can mix efficiently with the iron d orbitals, such as **1**, **5**, or **6**, or in systems without a distal ligand, like **2**, one of the π^* orbitals becomes a nonbonding d_{xz} orbital and the t_{2g} splitting becomes

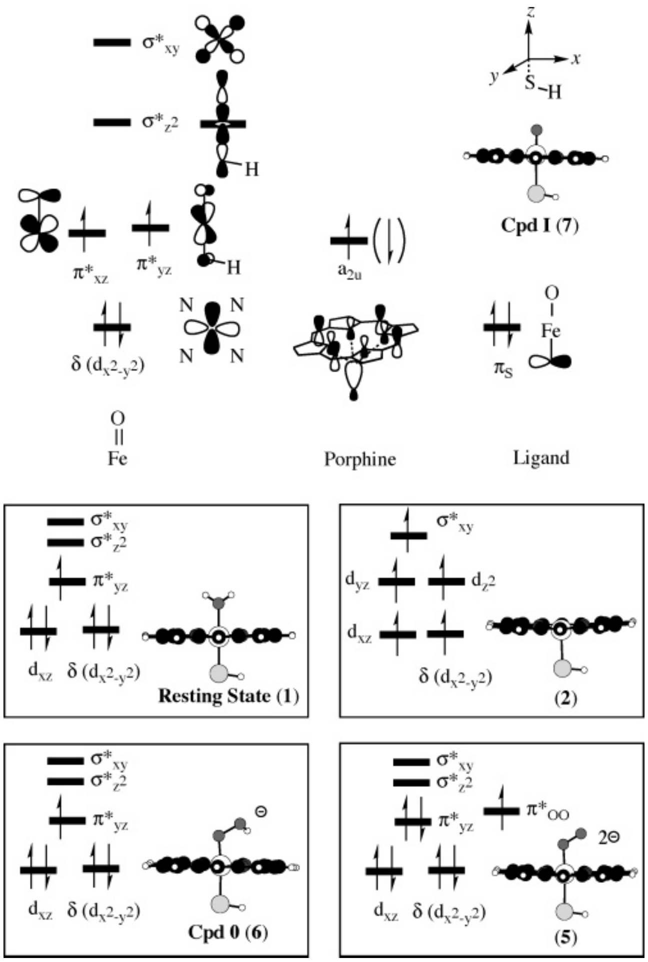

Figure 4. Orbital occupation of Cpd I (top). Shown below are the orbitals of the resting state (**1**), the pentacoordinated ferric complex (**2**), the ferric peroxo complex (**5**), and Cpd 0 (**6**).

two-below-one. The electronic configurations that represent the ground states of **1**, **2**, **5**, and **6** are shown in the insets at the bottom of Figure 4.

One particular orbital in Figure 4, labeled a_{2u}, requires some special comments. This orbital is a high-lying nonbonding porphyrin orbital that mixes strongly with the σ_S orbital located on the axial ligand; in Cpd I this orbital is singly occupied. The mixing is particularly strong with a thiolate ligand,[112,122] but with a weaker donor ligand, such as imidazole,[123] the mixing is negligible. Another high-lying orbital is a sulfur lone pair, labeled in Figure 4 as π_S.

3.2. Resting State (1)

The resting state (**1**) is the most thoroughly studied species. According to electron spin−echo envelope modulation (ESEEM) spectroscopy it has a doublet ground state.[124] Using an early variant of the QM/MM technique, Harris and Loew[49,125] calculated the resting state of P450 by initially minimizing the X-ray structure with molecular mechanics and subsequently ran INDO/ROHF/CI semiempirical calculations with and without the incorporation of the electric field of the protein. Without the electric field the sextet was the ground state (3.84 kcal mol^{-1} below the doublet), but this ordering was reversed in favor of the doublet (by −1.59 kcal mol^{-1}) when the electric field was included. It was concluded[49] that this reversal also characterizes the situation in the enzyme; a synthetic ferric aqua complex with a thiophenoxide axial ligand[126] was found to have a sextet ground state, in support of this conclusion.

Single-point DFT calculations of Green[127] with B3LYP on a model system containing iron porphine and a methyl mercaptide axial ligand (Por,SMe; in Scheme 1) disputed these results. It was shown that with increasing size of the basis set (6-311+G* and larger), the ground state changed from a sextet state to the expected doublet state. Therefore, it was surmised that the doublet ground state is an intrinsic property of the resting state species. However, more recent results of Rydberg et al.[79] using the same model system but employing geometry optimization (B3LYP with a polarized all electron double-ζ basis set on Fe, 6-31+G* on oxygen, and 6-31G* on all other atoms) yielded a sextet ground state, lying 0.36 kcal mol^{-1} lower than the doublet state and much lower than the quartet state. The near-degeneracy of the doublet and sextet spin states of **1** is consistent with the experimental observation of spin equilibrium of the doublet ground state with a sextet state.[128−130]

Filatov et al.[131] studied the simplest model system (Por,SH in Scheme 1) using partial geometry optimization and the BP86 pure density functional and found a doublet ground state. They further investigated two orientations of the water ligand, in the upright and tilted configurations, and found a preference for the tilted one, by 6.6 kcal mol^{-1}, due to internal hydrogen bonds of the water hydrogens with the nitrogen atoms of the porphine. These conformations were subsequently reoptimized using DFT-(B3LYP)/LACVP-DZ.[37,132] The results depicted in Figure 5a show that the energy difference between the two conformations drops to only 1.1 kcal mol^{-1} in favor of the tilted conformation, thereby suggesting that hydrogen bonding with the protein residues can tip the balance in favor of the upright conformation.[37]

In the most extensive study of the resting state of P450$_{cam}$ to date, Schöneboom and Thiel[85] reported DFT/MM calculations for the entire system (ca. 28 500 atoms, with protein/water environment) using two different QM regions for the thiolate ligand (HS and ext-SCys), two different protonation states (for Asp$_{297}$), three different density functionals (BLYP, B3LYP, and BHLYP), two different basis sets, and six different snapshots as starting points for the QM/MM optimization. The relative energies of the spin states were strongly affected by the choice of the functional, consistent with previous computational experience[133,134] on other iron complexes: BLYP overestimates the stability of the low-spin states, BHLYP artificially favors high-spin states, and only B3LYP gives realistic multiplet splittings. The results were less dependent on the other choices (such as protonation state or snapshot).

Some representative DFT(B3LYP)/MM data for the resting state[85] are summarized in Figure 5b. Concerning the optimized geometries, the water ligand is tilted also in the protein but less so than in the

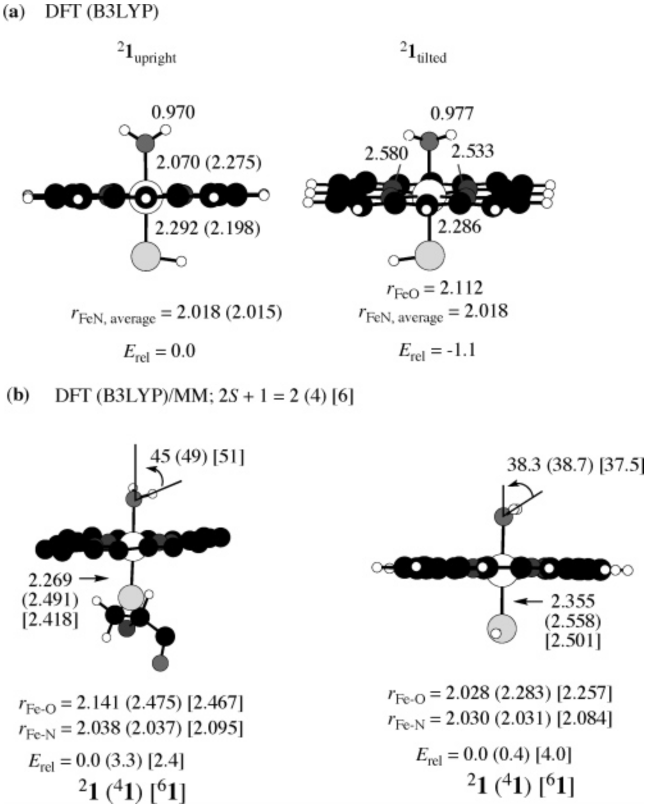

Figure 5. (a) Optimized geometry parameters of the doublet resting state with upright and tilted conformations of the axial water ligand, and relative energies (in kcal mol^{-1}) of these two conformers in the gas phase. Results out of parentheses (Por,SH model) from de Visser et al.[132] and in parentheses for the SMe,Por model from Rydberg et al.[79] (b) DFT(B3LYP)/MM geometry parameters (Por,ext-SCys and Por,SH models) of each spin state of the resting state (**1**) and relative spin-state energies taken from ref 85. $r_{\text{Fe-N}}$ is the average distance of the four Fe–N bonds. The spin states are indicated by superscripts on the left-hand side of the species number **1**. The bond lengths and angles are given in Å and degrees, respectively.

gas phase (by at least 10°) because of hydrogen-bonding interactions with the other water molecules in the pocket. In fact, the calculated tilt in the doublet ground state is in excellent agreement with ESEEM measurements,[124] as may be judged by comparing the calculated distances between the iron and the protons of the bound water molecule, 2.646 and 2.620 Å, to the ESEEM datum of 2.62 Å. Furthermore, the predicted Fe–O (2.141 Å) and Fe–S (2.269 Å) distances for the ground state are, respectively, in reasonable agreement with the X-ray data of 2.28 and 2.25 Å (pdb file: 1PHC).[25] It was noted that the protein environment shortens the Fe–O bond and lengthens the Fe–S bond compared with the gas-phase values.

In agreement with experiment, the DFT(B3LYP)/MM calculations[85] predict a doublet ground state and closely lying quartet and sextet states. As can be seen from the energy differences in Figure 5b, the three states are packed within 4 kcal mol^{-1} or so. A dense spin-state manifold was found also in single-point DFT/MM calculations by Scherlis et al.[135,136] on a fixed geometry of the resting state. This closeness of the spin states is in line with the experimental observation of spin equilibrium.[130] The DFT(B3LYP)/MM energy gaps in Figure 5b are smaller than the corresponding gas-phase DFT(B3LYP) values; especially affected is the quartet state that is greatly stabilized by the protein. Thus, the protein environment indeed has a significant impact on the physical and chemical properties of the species. A closer analysis[85] shows that the protein environment causes energy lowering of the $\sigma^*_{z^2}$ orbital (see Figure 4), which is populated in both the quartet and sextet states. This energy lowering stabilizes both states, which approach the doublet ground state, and leads to stronger binding of the water ligand in these states; the latter ligand is almost detached in the gas-phase quartet and sextet species.

The recently reported[89] DFT(ROB3LYP)/MM relative energies of 0.0/9.5/20.8 kcal mol^{-1} for the doublet/quartet/sextet spin states seem less accurate; this level spacing is much too large for the experimentally observed spin equilibrium. Furthermore, the DFT(ROB3LYP)/MM results indicate that these energy gaps increase relative to the gas-phase DFT values,[89] whereas the qualitative mechanism deduced from the DFT(UB3LYP)/MM calculations[85] implies that these gaps should decrease in the enzyme.

It is interesting to compare **1** to the analogous complex with an axial imidazole ligand. Loew and Dupuis[39] studied this species using CASSCF(5,5) calculations, which correlate the five iron electrons in the five d-type orbitals. The calculations predicted a sextet ground state with $\delta^1\ \pi^*_{xz}{}^1\ \pi^*_{yz}{}^1\ \sigma^*_{z^2}{}^1\ \sigma^*_{xy}{}^1$ configuration, with the quartet and doublet states lying 51.0 and 78.6 kcal mol^{-1} higher in energy. Smaller but still significant gaps between the spin states were obtained by Rydberg et al.[79] using DFT-(B3LYP). These results highlight the fact that the thiolate ligand of **1** is a powerful σ- and π-donor that binds to iron by mixing strongly with its orbitals, leading to high-lying $\sigma^*_{z^2}$ and π^*_{xz}, π^*_{yz} orbitals. This in turn stabilizes the doublet as the ground state by virtue of stronger bonding to iron while condensing all the higher spin states (which enjoy exchange stabilization) into a narrow range of energy.

3.3. Pentacoordinate Ferric–Porphyrin (2) and Ferrous–Porphyrin (3) Complexes

Experimental work suggests that the pentacoordinated ferric complex **2** has a sextet ground state, ^{6}**2**, but there is spin equilibrium with the doublet state, which is very sensitive to the protein environment.[130,137] In the pentacoordinated ferric complex **2** the electronic structure of ^{6}**2** corresponds to the orbital occupancy $d_{x^2-y^2}{}^1 d_{xz}{}^1 \pi^*_{yz}{}^1 \sigma^*_{z^2}{}^1 \sigma^*_{xy}{}^1$ (see orbitals in Figure 4). The doublet state, ^{2}**2**, corresponds to $d_{x^2-y^2}{}^2 d_{xz}{}^2 \pi^*_{yz}{}^1$ and the intermediate spin state, ^{4}**2**, to $d_{x^2-y^2}{}^2 d_{xz}{}^1 \pi^*_{yz}{}^1 \sigma^*_{z^2}{}^1$.

Much like the pentacoordinated ferric complex, the reduced ferrous complex **3**, obtained after electron uptake by ^{6}**2**, is known to have a high-spin quintet state, ^{5}**3**.[129,138] Two alternative electronic configurations are possible, $d_{x^2-y^2}{}^2 d_{xz}{}^1 \pi^*_{yz}{}^1 \sigma^*_{z^2}{}^1 \sigma^*_{xy}{}^1$ and $d_{x^2-y^2}{}^1 d_{xz}{}^2 \pi^*_{yz}{}^1 \sigma^*_{z^2}{}^1 \sigma^*_{xy}{}^1$ (see orbitals for **2** in Figure 4); these may be labeled as ^{5}**3**$_{xz}$ and ^{5}**3**$_{x^2-y^2}$.[81] Closely lying states are the triplet state, ^{3}**3**, with $d_{x^2-y^2}{}^2 d_{xz}{}^2 \pi^*_{yz}{}^1 \sigma^*_{z^2}{}^1$

configuration and a singlet state, $^{1}\mathbf{3}$, with $d_{x^2-y^2}{}^{2}d_{xz}{}^{2}\pi^{*}_{yz}{}^{2}$ occupation.

The orbital occupancies of **2** and **3** suggest that the complexes will differ in their Fe−S bond lengths, since the $\sigma^{*}_{z^2}$ orbital involves antibonding interactions between iron and sulfur. In addition, a delicate balance among orbital energy, exchange stabilization, and modulation thereof by the protein environment will determine the relative energies of the spin state.

The pentacoordinated iron−porphyrin complexes (**2** and **3**) were calculated by Ogliaro et al.[81] using the Por,SH model (Scheme 1) and subsequently by Rydberg et al.[79] using the Por,SMe model. Recently, Altun and Thiel[88] used DFT(B3LYP)/MM to study these species in two different snapshots and a variety of basis sets, and an extensive DFT(B3LYP) study was carried out to benchmark the appropriate basis set for this problem. Altun and Thiel[88] also tested different functionals and showed that the relative state ordering, as may be deduced from experiment, is best reproduced with the B3LYP hybrid functional; BLYP prefers lower spin states, and BHLYP exaggerates the energy differences.

Figure 6a shows in the first line optimized geometric parameters by Ogliaro et al.[81] for the low-lying spin states of **2** and **3**, while the second line shows these parameters for the ground states, $^{6}\mathbf{2}$ and $^{5}\mathbf{3}$, from Rydberg et al.[79] The third line lists the values for the Por,SH model from Altun and Thiel[88] for the largest basis set (B2W) comprised of an all-electron Wachters basis set on iron, augmented with diffuse d functions and polarization f functions, and a 6-31+G* basis set on the atoms that form the coordination sphere of iron (6-31G for the rest). The three sets of results show some scatter, of course, but they agree with regard to the trends, and the computed geometries are in reasonable accord with the experimental X-ray data.[28] Extended basis sets, and the SMe representation of the thiolate ligand, tend to yield shorter Fe−S distances in both $^{6}\mathbf{2}$ and $^{5}\mathbf{3}$ (see Figure 6a), although the results depend less on the choice of the thiolate model (SH or ext-SCys) when using larger basis sets.[88] The computed relative energies of the spin states are given underneath the structural data, in the same ordering (Figure 6a). High-spin ground states are found in all these gas-phase model calculations, and the ferrous complex has a $^{5}\mathbf{3}_{xz}$ ground state with the $^{5}\mathbf{3}_{x^2-y^2}$ state lying only ca. 2 kcal mol^{-1} higher.[81,88]

Figure 6b presents selected results from the DFT(B3LYP/B2W)/MM study[88] for two QM regions (Por,SH and Por,ext-SCys) and one snapshot (snap31). Compared with the gas phase (Figure 6a, line 3), the Fe−S bond becomes longer in the protein environment, especially in the triplet state of the ferrous complex, $^{3}\mathbf{3}$. As in the gas phase, both the ferric and ferrous complexes have high-spin ground states, in agreement with experiment. By contrast, a recent DFT(ROB3LYP)/MM study[89] reports a quartet rather than a sextet ground state for the ferric complex **2**; this discrepancy may be due to the basis set employed[139] because a larger all-electron basis for iron is needed in the DFT(B3LYP/B2W)/MM calculations to produce the correct sextet ground state.[88] According to the DFT(B3LYP/B2W)/MM results[88] the protein inverts the relative ordering of the quintet electromers of the ferrous complex **3**: a $^{5}\mathbf{3}_{x^2-y^2}$ ground state is predicted in the enzyme (one electron in the δ orbital, see Figure 4), which is preferred by 0.5 kcal mol^{-1} over the $^{5}\mathbf{3}_{xz}$ electromer, when the larger QM region is used.

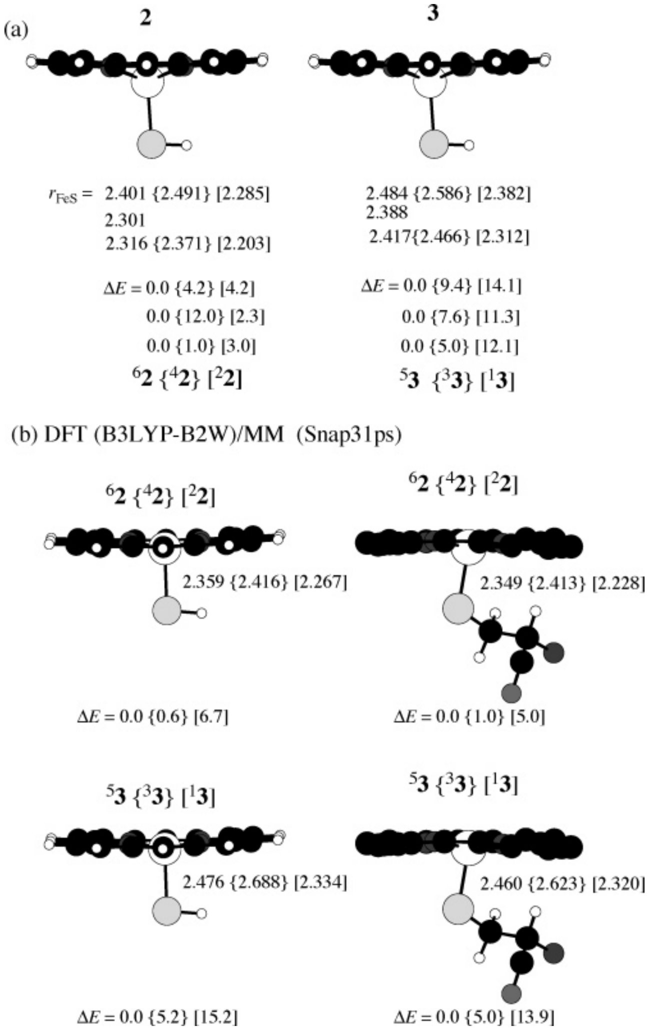

Figure 6. Optimized Fe−S bond lengths of **2** and **3,** and relative energies of the various spin states (in kcal mol^{-1}). The superscripts on the left-hand side refer to the spin multiplicity ($2S + 1$) of the state. (a) B3LYP studies: The top line shows results for the Por,SH model from ref 81 at the B3LYP/LACV3P+*(Fe),6-311+G*(rest)//B3LYP/LACVP-DZ level. The second line in each case gives the data for the Por,SMe model from ref 79 at the B3LYP level with an augmented all-electron DZ basis set. The third line shows the B3LYP/B2W results from ref 88; the Fe−S bond lengths are for the Por,SH model, while the energy data refer to the Por,ext-SCys model. (b) DFT(B3LYP/B2W)/MM results for the small and large QM subsystems.

Table 1 compares the calculated[88] Mössbauer parameters for the complexes with experimental values.[129,138,140] In the ferric complex (**2**) the calculated isomer shifts (δ parameter) for all spin states are close to each other and to the experimental value. Larger discrepancies are found for the quadrupole splitting (ΔE_Q); the computed value for the sextet state best matches the experimental datum. The asymmetry parameter (η) is, however, reasonably

Table 1. Experimental[a] and Computed[b] Mössbauer Isomer Shift δ, Quadrupole Splitting ΔE_Q, and Asymmetry Parameter η of Each State of the Ferric and Ferrous Pentacoordinated P450$_{Cam}$ Complexes[c]

complex	spin state	δ (mm/s)	$\lvert\Delta E_Q\rvert$ (mm/s)	η
ferric	^{6}**2** (exp.)	0.44	0.79	0.6
	^{6}**2**	0.42/0.43	0.40/0.24	0.72/0.69
	^{4}**2**	0.38/0.38	1.74/1.64	0.06/0.14
	^{2}**2**	0.40/0.39	2.42/2.23	0.64/0.77
ferrous	^{5}**3** (exp.)	0.82	2.42	0.8
	^{5}**3** [d]	0.88(0.83)/0.92	4.77(2.83)/4.28	0.08(0.61)/0.07
	^{3}**3**	0.69/0.66	1.74/1.24	0.53/0.52
	^{1}**3**	0.65/0.62	1.83/1.91	0.21/0.09

[a] Referencess 129, 138, and 140. [b] Reference 88. [c] The numbers separated by the sign "/" belong to DFT(B3LYP)/MM and DFT(B3LYP) calculations of the entire protein system and of the gas-phase system at the gas-phase geometry, respectively. The calculations were performed on the optimized geometries of Por,ext-SCys (with and without protein environment) using LACVP basis set on iron and 6-31+G* basis set on the atoms coordinated to iron (6-31G for the rest). In the Mössbauer spectral calculations iron was represented with triply polarized core properties basis set CP(PPP) while SV(P) basis set was assigned to the remaining atoms taking the inner s functions completely uncontracted. [d] The numbers in and out of parenthesis belong to $^5\mathbf{3}_{x^2-y^2}$ and $^5\mathbf{3}_{xz}$ electromers in the protein environment, respectively.

well reproduced for the sextet state. The ferrous complex has a quintet ground state with two electromeric options, $^5\mathbf{3}_{x^2-y^2}$ and $^5\mathbf{3}_{xz}$. Inspection of the Mössbauer data shows that the best fit of the quadrupole splitting and asymmetry parameters unequivocally assigns the ground state as $^5\mathbf{3}_{x^2-y^2}$, with one electron in the $\delta(d_{x^2-y^2})$ orbital. This assignment is consistent with the DFT(B3LYP/B2W)/MM energies (see above).

The experimental values of the reduction potentials of free and putidaredoxin-bound **2** are −170 and −173 mV, respectively.[114,140] Using the potential of the standard hydrogen electrode (−4.43 V)[141] as reference, this implies that the free-energy change ΔG for the reduction $\mathbf{2} + e^- \rightarrow \mathbf{3}$ is −98 kcal mol^{-1}. Approximating ΔG by the energy change ΔE, one would thus expect this reduction to be exothermic by around −98 kcal mol^{-1}. Using suitable gas-phase models, B3LYP calculations predict the conversion of ^{6}**2** into ^{5}**3** to be moderately exothermic: −51.4 kcal mol^{-1} with SH as axial ligand,[81] −37.4 kcal mol^{-1} with SMe as axial ligand,[79] and −46.8 kcal mol^{-1} again with SH as axial ligand.[88] The reduction becomes even more exothermic in a dielectric medium, i.e., −85.5 kcal mol^{-1} with a dielectric constant of $\epsilon = 5.7$[81] and −80.2 kcal mol^{-1} with $\epsilon = 80$,[79] indicating that continuum solvation effects favor the reduced ferrous form by 34 and 43 kcal mol^{-1}, respectively. DFT(B3LYP)/MM calculations[88] yield a similar differential stabilization of 35 kcal mol^{-1} *by a neutral protein environment* (compared with the gas phase) and lead to an overall reduction energy of −81.6 kcal mol^{-1} (QM region, Por,SH; basis set, LACVP-DZ). In these QM/MM calculations it is mandatory to use a neutral protein environment with zero net charge in order to avoid artifacts from unphysical long-range electrostatic interactions that arise in the ferrous complex if the protein environment contains charged residues at the surface.[88] The deviation of around 17 kcal mol^{-1} between the best computed reduction energies and the estimated experimental value has been analyzed and partly ascribed to the limited accuracy of B3LYP electron affinities,[88] but the main cause of the error is probably the lack of configurational sampling. Recent free-energy calculations on reduction potentials in enzymes[142,143] have emphasized the importance of proper sampling and derived QM/MM-based reorganization energies[143] which are substantial and will only partly be captured in an approach relying on geometry optimization.

3.4. "Push" Effect of the Thiolate and Gating of the Catalytic Cycle

Ogliaro et al.[81] used DFT(B3LYP) to study the effect of the thiolate ligand on the reduction process and analyzed the data based on the energy scheme shown in Figure 7a. The scheme compares the reduction energies of the ferric to ferrous porphyrin ($\mathbf{2} \rightarrow \mathbf{3}$) with a model devoid of the thiolate (left) and another model with a point charge replacing the axial ligand (center). Thus, by comparing the reduction energies in the presence of thiolate with the complex devoid of a ligand, one obtains the full effect of the thiolate, which is seen to be very large, about 100 kcal mol^{-1}; *the thiolate makes the reduction much less facile due to its donor ability*. This constitutes a quantitation of the so-called "push" effect of the cysteine. Using a dielectric constant of $\epsilon = 5.7$, the total "push" effect is reduced to 33 kcal mol^{-1}, which is still quite significant.[81]

The energy changes can be further dissected into the quantities ΔE_{field} and ΔE_{QM}, which denote the electrostatic and quantum mechanical contributions. ΔE_{field} measures the effect of merely placing a classical negative charge at the site of the thiolate, while ΔE_{QM} represents the effects due to orbital mixing, charge transfer, and other quantum mechanical effects. It is found that the thiolate effect is mainly of electrostatic origin: ΔE_{field} dominates, while the QM contribution ΔE_{QM} is minimal. This makes sense since the reduction involves filling of the nonbonding $\delta(d_{x^2-y^2})$ orbital, which does not mix with the thiolate or other orbitals.

The catalytic cycle is initiated by the reduction of **2**; the resting state, **1**, is stable toward reduction. To understand this selective gating, Ogliaro et al.[81] also calculated the reduction of the resting state, Figure 7b. In the case of **1**, the "push" effect of the thiolate comprises an electrostatic contribution of 85.6 kcal mol^{-1} and a smaller quantum mechanical contribution of 15.5 kcal mol^{-1}. The latter comes from the mixing of the π^*_{yz} orbital with the lone pair on sulfur,

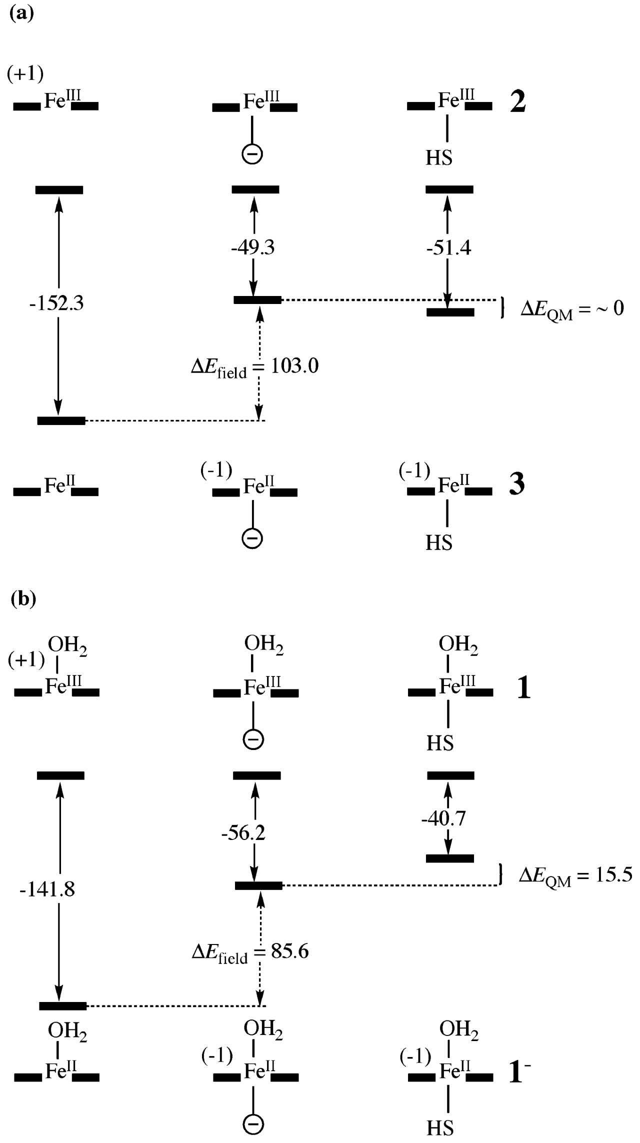

Figure 7. Estimation of the "push" effect of the thiolate on (a) the reduction energy **2** → **3** and (b) the reduction of **1**. All energies are calculated at the UB3LYP/LACV3P+* level of theory. (Reprinted with permission from ref 81. Copyright 2002 Elsevier Inc.)

which is raised in energy. As may be seen by comparing parts a and b of Figure 7, the reduction of the pentacoordinated complex (**2**) is 10.7 kcal mol^{-1} more exothermic than the reduction of the resting state (**1**), compared with an experimental value of about 5 kcal mol^{-1}. This small energy difference is the reason the resting state is not reduced by the reductase. Thus, the presence/expulsion of a water molecule gates the catalytic cycle, as is well understood by the experimental community.[114,144] However, by looking at the energies of these processes it is apparent that without the thiolate ligand, both **1** and **2** could be easily reduced by most reductants. It is the thiolate ligand that controls the gating of the catalytic cycle by making the system a poorer electron acceptor *so that only the pentacoordinated ferric porphyrin can be reduced by the reductase*. Thus, the "push" effect of the thiolate ligand gates the catalytic cycle of P450 enzymes.[81]

3.5. Ferrous Dioxygen (4) and Ferric Peroxo (5) Complexes

Harris et al.[145,146] published the first DFT calculations on the oxygen-bound iron porphyrin complexes (**4** and **5**) using the BPW91 and BLYP functionals with a double-ζ plus valence polarization basis set (DZVP). In agreement with experimental data,[147] the calculations[146] revealed that the most stable form of the ferrous dioxygen species (**4**) is an end-on complex, while a symmetrically bridged isomer is much less stable, by 28 kcal mol^{-1}. The electronic ground state was found to be a singlet, consistent with the fact that it is EPR silent. All subsequent DFT investigations[37,79] confirmed that the ground state $^{1}\mathbf{4}$ is an open-shell singlet with singly occupied π^*_{yz} and π^*_{OO} molecular orbitals (consult Figure 4). The former orbital mixes strongly with the π^* orbitals on the dioxygen group, so that the actual electronic state is a resonating form between Fe^{II}–O$_2$ and Fe^{II}–O$_2^-$. As a result, there is also a low-lying triplet state which is only 1.1,[146] 3.2,[79] or 3.5–3.2 kcal mol^{-1} [37] higher in energy. In fact, the ground state $^{1}\mathbf{4}$ can be viewed as a complex formed between the excited singlet state $^{1}\mathbf{3}$ of the ferrous complex and the $^{1}\Delta_g$ state of O$_2$, attended by electron transfer from iron to dioxygen. On the other hand, coupling of the ground state $^{5}\mathbf{3}$ with singlet or triplet states of molecular oxygen leads to low-lying quintet, $^{5}\mathbf{4}$, or heptet states $^{7}\mathbf{4}$ (9.6 kcal mol^{-1} above $^{1}\mathbf{4}$).[37] Therefore, the O$_2$ binding must occur by a spin-crossing process. The theoretical study of Jensen and Ryde[148] on the oxygen binding process of the corresponding myoglobin complex (with imidazole as an axial ligand) showed indeed the expected state crossing, with a low-lying crossing point (only slightly above the separated reactants, $^{5}\mathbf{3}$ and ^{3}O$_2$), which occurs in a region where the respective surfaces are nearly parallel, with a very small difference in the respective slopes. Using the Landau–Zener model for diabatic crossing probability, this will lead to an efficient crossing even though the spin–orbit coupling is small. Therefore, ^{3}O$_2$ binding is a fast and efficient process in myoglobin. Thus, while the situation in P450 has yet to be elucidated by theory, the study of Jensen and Ryde[148] implies that this may be similar. This is the second point in the cycle where the crossover of spin states is important. More examples will follow later in the cycle.

As shown first by Harris et al.,[145,146] reduction of the ferrous into the ferric–peroxo species fills the π^*_{yz} orbital of $^{1}\mathbf{4}$ and leads to longer Fe–O and Fe–S bond lengths and a decrease of the O–O bond order from 1.20 to 0.87. Both EPR data and DFT calculations yield a doublet ground state $^{2}\mathbf{5}$ with spin densities located on both oxygen atoms. The semiempirical INDO/S/CI calculations predict electronic spectra[145,146] in good agreement with experiment, e.g., a split Soret band.

Pioneering studies of the effect of the protein environment on the stability of $^{1}\mathbf{4}$ and $^{2}\mathbf{5}$ were carried out by Harris and Loew,[149,150] who performed molecular dynamics simulations on both P450$_{cam}$ and P450$_{eryF}$ and found that the ferrous dioxygen complex is stabilized due to a hydrogen bond from the hy-

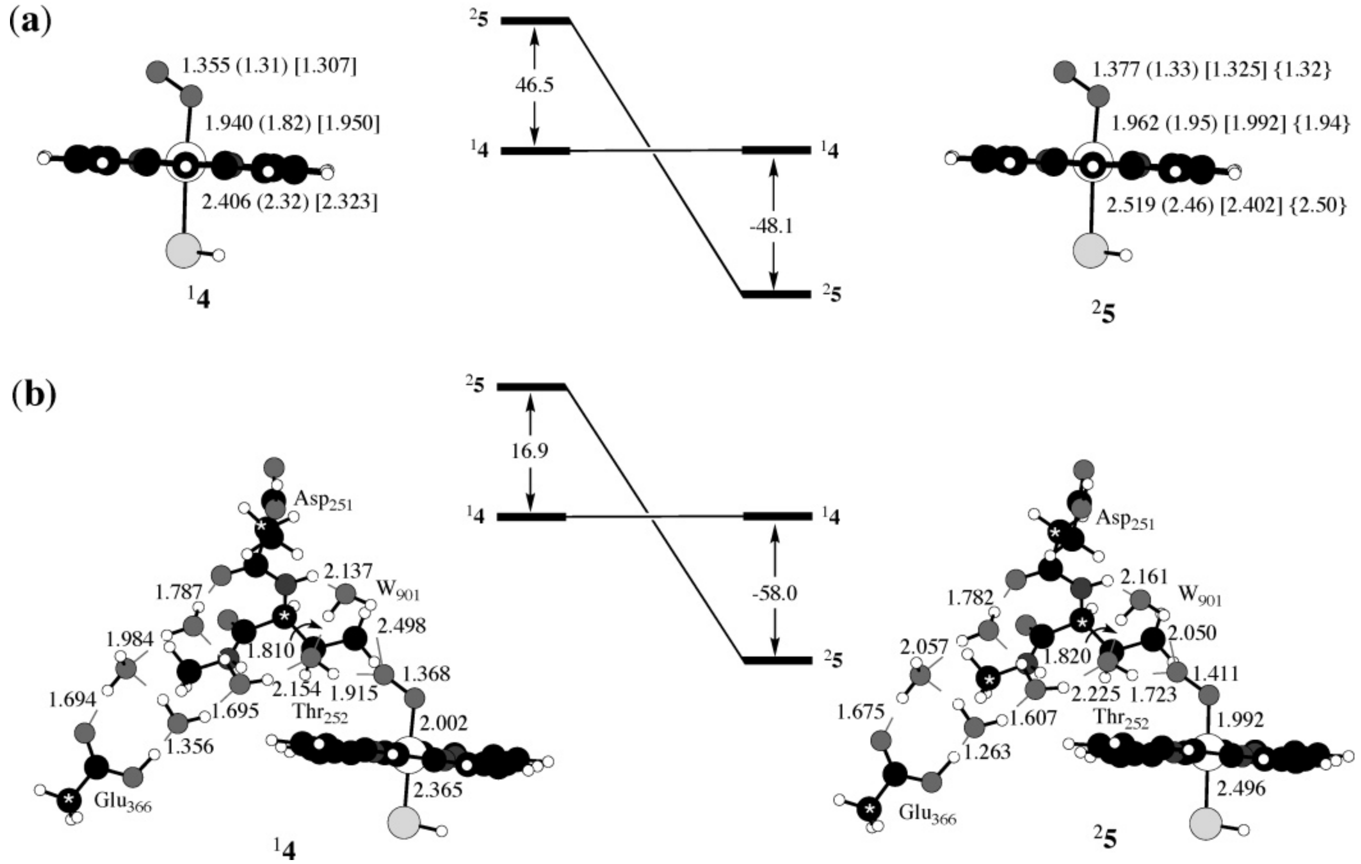

Figure 8. (a) Optimized geometries of ^{1}**4** and ^{2}**5**. B3LYP/LACVP-DZ results for the Por,SH model from ref 132 and BPW91/DZVP results for the Por,SMe model from ref 146 are given out of and in parentheses, respectively. The results in square and curly brackets correspond to the B3LYP/DZ(augmented) results for the Por,SMe model from ref 79 and DFT(ROB3LYP)/MM results (LACVP**(Fe)6-31G*(rest)) basis set) from ref 89, respectively. (b) Optimized geometries of ^{1}**4** and ^{2}**5** using the large Por,SH model of ref 132. The reduction energy (kcal mol^{-1}) of the process ^{1}**4** → ^{2}**5** in a vacuum (left) and for a dielectric constant of 5.7 (right) is given between the structures. Energies include ZPE corrections.

droxyl group of Thr$_{252}$.[149] In P450$_{\text{eryF}}$, this threonine group is not available and a serine amino acid was identified to connect to the distal oxygen via a chain of water molecules.

Figure 8 shows key optimized geometric parameters of ^{1}**4** and ^{2}**5** obtained with different DFT models and methods. Part a of Figure 8 displays the results on the small models (Por,SH and Por,SMe) containing a dioxygen ligand.[37,79,80,89,132,146] The different sets of results show similarities and differences in the three bond lengths. Part b of Figure 8 shows the optimized geometries of ^{1}**4** and ^{2}**5** including a truncated proton-relay machinery of P450[132] which includes the amino acids labeled Asp$_{251}$ and Thr$_{252}$, an acetic acid group replacing Glu$_{366}$, and five sequestered water molecules labeled as W (using the numbering system for P450$_{\text{cam}}$). The addition of the proton-relay machinery lengthens the Fe−O distance and shortens the Fe−S distance compared with the bare small model (Por,SH). Thus, the electrostatic interactions of the dioxygen ligand with the water molecules and the peptide groups apply a *trans*-effect; the Fe−S bond gets shorter due to the weakening of the Fe−O bond. The large model also shows some important changes in the surrounding environment during the reduction from ^{1}**4** to ^{2}**5**, such as the shortening of the hydrogen bonds between the terminal oxygen atom of the O_2 moiety and the hydroxyl group of Thr$_{252}$ to 1.723 Å and between O_2 and W$_{901}$ by 0.445 Å. Moreover, changes occur during the reduction even at farther distances from the iron center. Remarkably, upon reduction the proton connected to the carboxylic acid group of Glu$_{366}$ moves closer toward the neighboring water molecule, from 1.356 to 1.263 Å. With the exception of the O−O distance in ^{2}**5**, the other bond lengths are close to the DFT(ROB3LYP)/MM values[89] obtained with a much larger QM model (PPIX,SCys; see Scheme 1).

The gas-phase reduction energies for the bare species are computed to be endothermic, very much so in the small system and less so in the large model. However, adding the effect of a dielectric medium makes the reduction exothermic for both models. Note that even in the dielectric medium the reduction energy of the larger model is still more exothermic that the respective energy of the smaller model, by 9.9 kcal mol^{-1}. This suggests that the hydrogen-bonding interactions of the amino acid residues and water molecules with the active species are important for the stabilization of **5**.

3.6. First Protonation Step: Conversion of Ferric Peroxo Complex (5) into Cpd 0 (6)

The protonation mechanism converting ^{2}**5** into Cpd 0 (^{2}**6**) was studied first by Harris et al.[145,151,152] on P450$_{\text{eryF}}$ using a combination of DFT and MM techniques. The early DFT calculations of Harris and

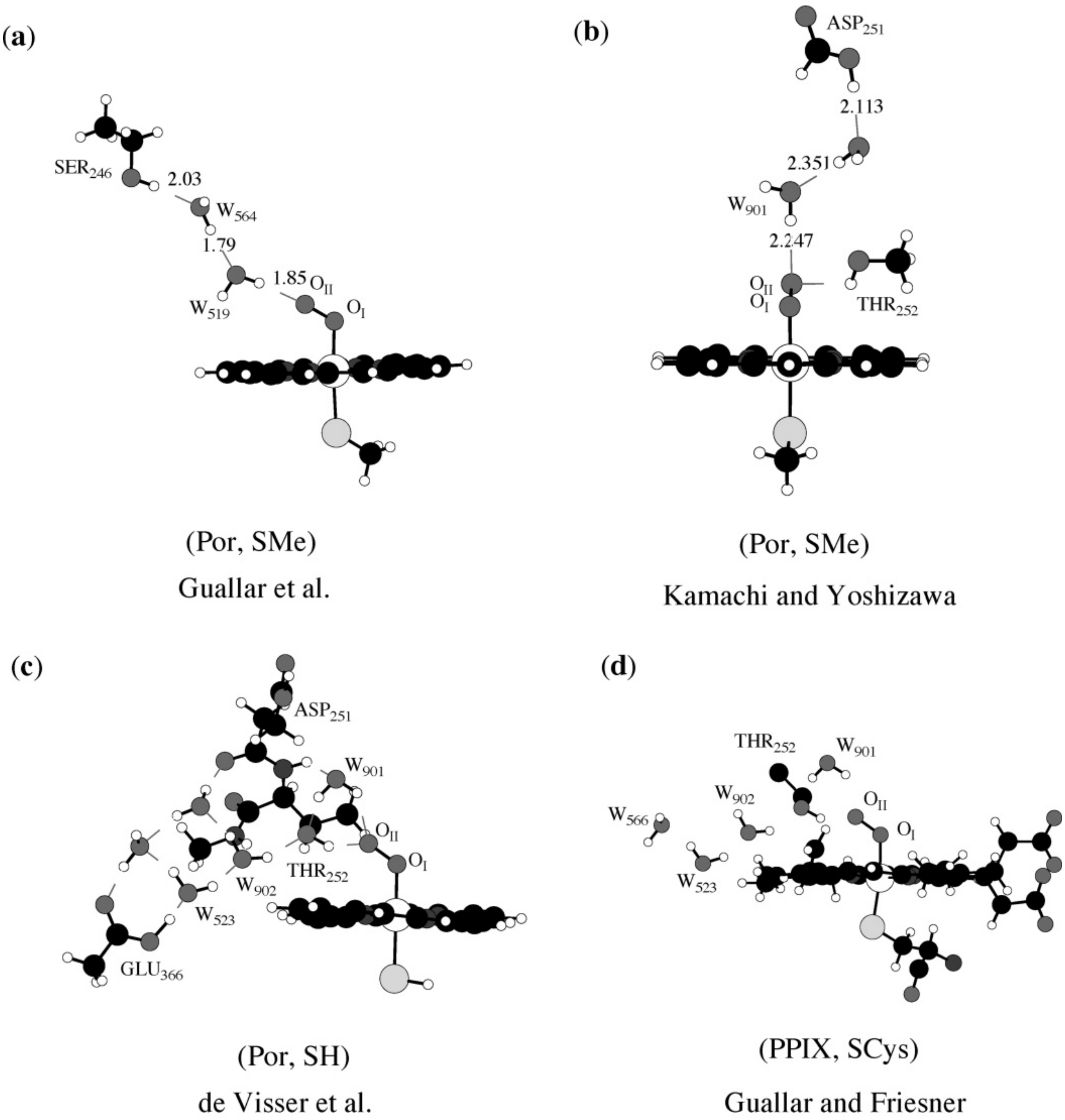

(Por, SMe) Guallar et al.

(Por, SMe) Kamachi and Yoshizawa

(Por, SH) de Visser et al.

(PPIX, SCys) Guallar and Friesner

Figure 9. Protonation models of $^{2}\mathbf{5} \rightarrow {}^{2}\mathbf{6}$ taken from (a) ref 151, (b) ref 104, (c) ref 132, and (d) ref 89. The model used (see Scheme 1) is indicated underneath the heme species in parentheses.

Loew[145] showed that $^{2}\mathbf{5}$ is an extremely strong base, with a proton affinity of 422 kcal mol^{-1}, and may even accept a proton from a nearby water molecule. A subsequent DFT(ROB3LYP)/MM study[151] on the protonation step from $^{2}\mathbf{5}$ to $^{2}\mathbf{6}$ was performed on P450$_{\text{eryF}}$ in combination with a molecular dynamics simulation. Added to this were proton sources with initially only one water molecule (W$_{519}$) but subsequently also a model with two water molecules (W$_{519}$ and W$_{564}$) and a model containing two water molecules and an ethanol molecule in the place of Ser$_{246}$, as shown in Figure 9a. These various calculations showed that the protonation ranges from an endothermic process for the smallest model (+20 kcal mol^{-1}) all the way to an exothermic process for the complete model depicted in Figure 9a ($-$10.7 kcal mol^{-1}). This dramatic change is the result of diminishing repulsion between the doubly negative $^{2}\mathbf{5}$ species and the incipient anion of the protonating species. The calculations ruled out the putative protonation of $^{1}\mathbf{4}$ and predicted a Grotthuss-type mechanism for the protonation of $^{2}\mathbf{5}$ by the array Ser$_{246}$$-W_{564}$$-W_{519}$. The significant kinetic solvent isotope effect (KSIE) measured by Aikens and Sligar[153] for the reduction of $^{1}\mathbf{4}$ is consistent with these results and implies that the protonation occurs rapidly after the electron transfer but almost synchronously with it. Subsequent MD studies[151] showed that the protonation of W$_{519}$ is fast (within 500 fs) and is the rate-determining step that triggers the sequential protonation of W_{564}. In a recent DFT study Harris[152] used B3LYP/LACVP**-(Fe), 6-31G*(H,C,N,O,S) calculations to study the effect of various candidate acids on the protonation of ^{1}**4** and ^{2}**5**. Since a hydronium ion could lead to protonation of both ^{1}**4** and ^{2}**5**, this species was ruled out as a likely proton source. By contrast, water molecules sequestered between the dioxygen moiety and a hydroxyl group of either serine or threonine were selective and able to protonate ^{2}**5** but not ^{1}**4**. Furthermore, Harris[152] found spin selection in the protonation of **5**; the protonation of ^{4}**5** was shown to be more costly than for ^{2}**5** due to the reduced negative charge on the terminal oxygen atom of the quartet species. In the largest model used by Harris[152] the protonation barrier ^{2}**5** → ^{2}**6** dropped to 1.3 kcal mol^{-1}. Thus, the hydrogen-bonding network provides the active center with subtle and spin-selective protonation machinery.

Subsequently, Kamachi and Yoshizawa[104] and de Visser et al.[132] used B3LYP to study the analogous protonation for P450$_{cam}$ with different methods and models. Guallar and Friesner[89] investigated the same process using DFT(ROB3LYP)/MM. These studies used the models shown in Figure 9b–d, all involving alcohol–acid pairs (Thr$_{252}$-Asp$_{251}$ and/or Thr$_{252}$-Glu$_{366}$) and water molecules. The presence of an alcohol–carboxylic acid couple in the vicinity of the active site[144] is a recurring motif in P450 enzymes and is believed to be responsible for the protonation mechanism.[116]

Kamachi and Yoshizawa[104] built a model based on the experimentally suggested mechanism of Vidakovic et al.[116] using two water molecules sequestered between the terminal oxygen atom of the hydroxyl group of Thr$_{252}$ and the carboxylic acid group of Asp$_{251}$, Figure 9b. The protonation machinery is initiated by proton transfer from the carboxylic acid group of Asp$_{251}$ to the nearby water molecule, which protonates the neighboring water molecule and then relays the proton to the terminal oxygen atom to form Cpd 0. The exothermicity for this process is large: −61.5 (−50.1) kcal mol^{-1} for the ^{2}**5** (^{4}**5**) species. It was observed that ^{2}**5** does not survive the acidic environment, and it was therefore necessary to constrain the geometry to prevent spontaneous protonation.

The third proton-relay machinery[132] in Figure 9c explored two protonation mechanisms whereby the proton originates from the carboxylic acid groups of Glu$_{366}$ or Asp$_{251}$. These choices were based on the MD simulations of Taraphder and Hummer,[154] which suggested that a carboxylic acid group is the most likely proton source and identified three contenders in the vicinity of the heme, namely, Asp$_{251}$, Glu$_{366}$, and the propionate side chains of the heme. The propionate side chains of the heme were ruled out[154] since the substrate (camphor) blocks the pathway between the propionate groups and the dioxygen moiety, and there remained only the Asp$_{251}$ and Glu$_{366}$ options. The MD studies further showed that upon rotation of the Asp$_{251}$ side chain the carboxylic acid group can donate a proton to W$_{901}$ and is therefore a strong contender as proton source. The second possible source is the carboxylic acid group of Glu$_{366}$ that forms a connection with the FeO$_2$ group via a chain of water molecules and the hydroxyl group of Thr$_{252}$.

The two protonation mechanisms of de Visser et al.[132] are summarized in Figure 10. The left-hand side shows the Asp$_{251}$-based mechanism. Thus, unlike Kamachi and Yoshizawa,[104] who added a second water molecule that accepts initially the proton from Asp$_{251}$, de Visser et al.[132] tried to trigger the initial protonation by the rotation of the aspartic acid side chain. Indeed, upon rotation of the Asp$_{251}$, which has a barrier of ~3 kcal mol^{-1}, the carboxylic proton is transferred to W$_{901}$ and from there to the distal oxygen of ^{2}**5** to yield Cpd 0 (^{2}**6′**), with a barrier of 3 kcal mol^{-1}. The right-hand branch depicts the mechanism for the proton transfer from the carboxylic acid group of Glu$_{366}$ via two sequestered water molecules (W$_{523}$ and W$_{902}$) and the hydroxyl group of Thr$_{252}$. As can be seen, the pathway of shuttling a proton from the carboxylic acid group of Glu$_{366}$ via W$_{523}$ to W$_{902}$ has a barrier of approximately 3 kcal mol^{-1}; thereafter the proton is relayed quickly to form Cpd 0 (^{2}**6**) with a barrier of 3 kcal mol^{-1}.

Consider now the optimized geometries of Cpd 0 after proton shuttle from Glu$_{366}$ (^{2}**6**) and after Asp$_{251}$ rotation and the transfer of its proton (^{2}**6′**), depicted at the bottom of Figure 10. These two conformations of Cpd 0 are different, especially the OOH group which either donates a hydrogen bond to W$_{901}$ (^{2}**6′**) or accepts a hydrogen bond from W$_{901}$ (^{2}**6**). In addition, the rotated Asp$_{251}$ side chain forms hydrogen-bonding interactions with the amidic nitrogen and with W$_{901}$, resulting in extra stabilization energy of ^{2}**6′** versus ^{2}**6**. As expected, the Fe–S, Fe–O, and O–O distances of ^{2}**6** and ^{2}**6′** are quite similar.

The two mechanisms in Figure 10 appear to be of equal status. However, it should be pointed out that in the enzyme the Asp$_{251}$ rotation causes the breaking of multiple hydrogen bonds, so that the actual barrier for this process may be somewhat higher. If this is true, then the most likely protonation machinery of ^{2}**5** is a subtle process originating from the glutamic acid (Glu$_{366}$) residues and being gated by the hydroxyl group of Thr$_{252}$; the latter residue fixes the O$_2$ group of the Fe–OO moiety by a donating hydrogen bond, thereby preventing auto-oxidation and direct protonation by a chain of water molecules connecting to a carboxylic acid group.

A recent DFT(ROB3LYP)/MM study of Guallar and Friesner,[89] see model description in Figure 9d, considered only the process originating from Glu$_{366}$ and obtained small barriers of 4.0 kcal mol^{-1} (note that the carboxylic acid group was not included in the QM subsystem). Moreover, the alternative mechanism with rotation of the aspartic acid group was not studied; thus, further DFT/MM studies will be required to find out whether the two protonation pathways are indeed competitive in the enzyme.

3.7. Cpd 0: Ferric–Hydroperoxide Complex (6)

As shown by Harris and Loew[145] and subsequently by Ogliaro et al.,[80] the ground state of the ferric–hydroperoxide complex corresponds to the $^2\Pi_{yz}$ state,

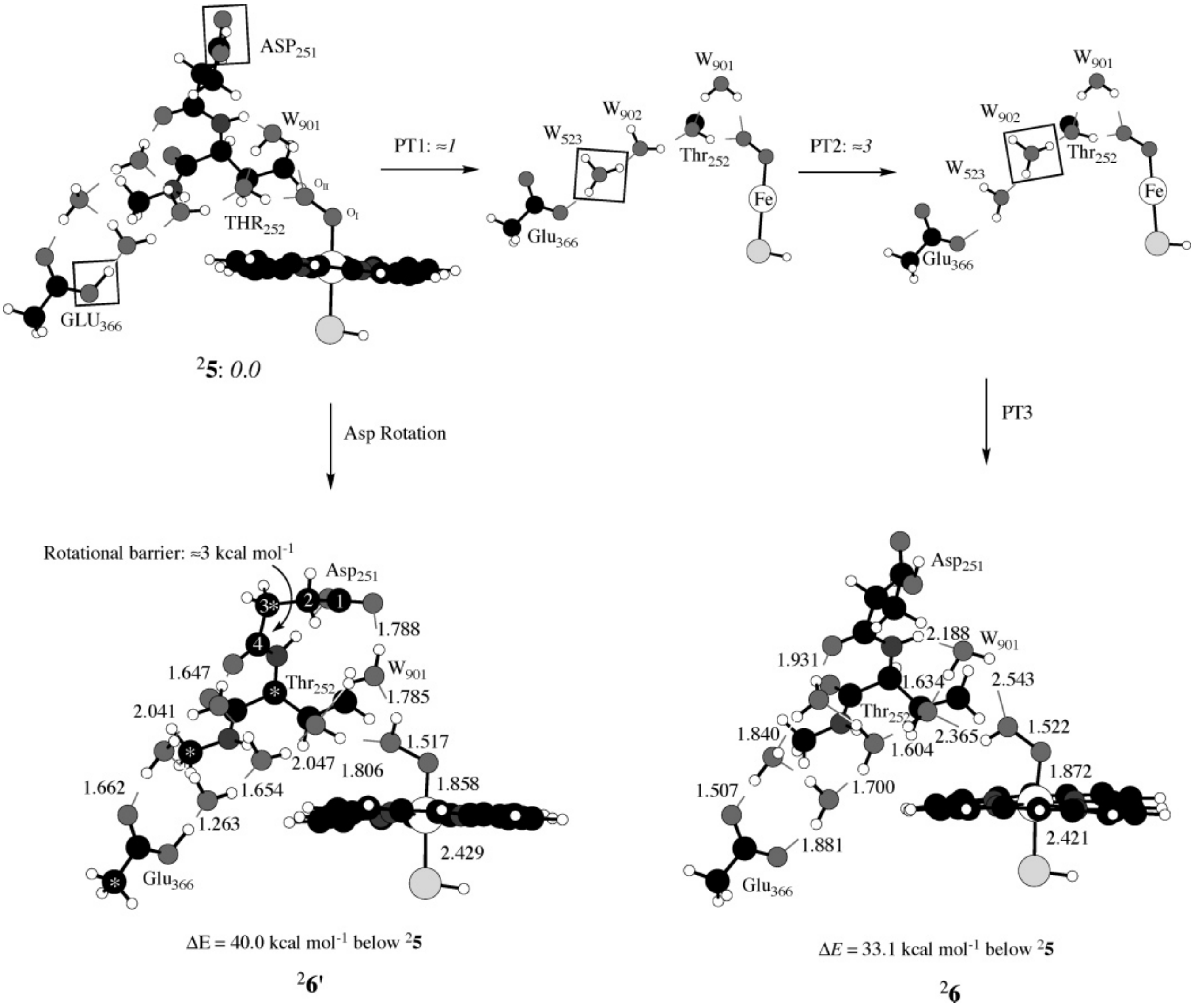

Figure 10. Protonation mechanisms[132] for the conversion of ^{2}**5** into Cpd 0 by Asp$_{251}$ and Glu$_{366}$ pathways, leading to two Cpd 0 conformers (^{2}**6** and ^{2}**6′**). The atoms defining the dihedral angle of Asp$_{251}$ rotation are labeled with numbers 1−4. Relative energies of ^{2}**5**, ^{2}**6′** and ^{2}**6** include ZPE corrections. Barrier heights (no ZPE) estimated from the geometry scans are in kcal mol^{-1} relative to ^{2}**5**. B3LYP/LACVP-DZ data.

^{2}**6**, with a single electron in the π^*_{yz} orbital (Figure 4); the quartet state, ^{4}**6**, lies 14.5 kcal mol^{-1} higher.[80] Optimized key geometric parameters of ^{2}**6** collected from a few sources[79,80,89,105,145] are summarized in Figure 11. Interestingly, the DFT(ROB3LYP)/MM results for the largest system[89] are rather close to the DFT(B3LYP) results for the smallest system.[80] A feature of ^{2}**6** in all the isolated molecule calculations is the characteristic hydrogen bond between the proton of the distal OH group and one of the nitrogen atoms of the porphyrin ring. This feature is common also to the large model ^{2}**6**, generated (Figure 10) by protonation from the Glu$_{366}$ region. By contrast, when the protonation originates from Asp$_{251}$, it occurs from the top (via W$_{901}$), leading thereby to conformer ^{2}**6′** (Figure 10) in which the OH group points upward, donating a hydrogen bond to a water molecule (W$_{901}$ in Figure 10) and accepting one from Thr$_{252}$. The same conformations were reported in the DFT(ROB3LYP)/MM study of Guallar and Friesner.[89] Most likely, the two conformations coexist and may or may not equilibrate depending on the lifetime of **6** and the rotational barrier of the OH group. The DFT(ROB3LYP)/MM study[89] suggests that such an equilibration should be fast.

Three groups[80,82,145] examined also the isomer of **6**, which is protonated on the proximal oxygen atom (labeled in Figure 11 as ^{2}**6**$_{\text{iso}}$). The three groups find ^{2}**6** to be more stable than ^{2}**6**$_{\text{iso}}$ by 18.4, 23.3, and 26.9 kcal mol^{-1}, respectively. Moreover, the protonation studies as described in the previous section (see Figure 10) show that the proximal oxygen atom of ^{2}**5** does not accept a hydrogen bond, thereby implying that the protonation of ^{2}**5** should take place exclusively at the distal oxygen atom to form ^{2}**6**. Hence, ^{2}**6**$_{\text{iso}}$ is not a likely intermediate in the catalytic cycle of P450$_{\text{cam}}$.

3.8. Protonation of Cpd 0 and Formation of Cpd I (7)

DFT calculations of the isolated molecule suggest that Cpd 0 (**6**) is a very strong base with a proton

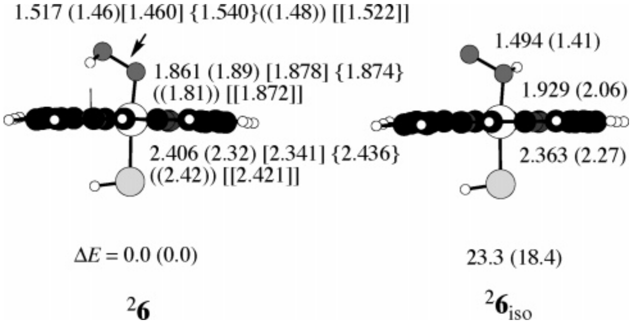

Figure 11. Optimized geometries of Cpd 0 (^{2}**6**) and its isomer ^{2}**6**$_{\mathrm{iso}}$. Geometry data from left to right: DFT-(B3LYP)/LACVP-DZ data[80] for the Por,SH system; DFT-(BPW91)/DZVP data[145] for the Por,SMe system; DFT-(B3LYP)/DZ(aug) data[79] for the Por,SMe system; DFT-(B3LYP)/LanL2DZ data[104] for the Por,SMe system; DFT-(B3LYP/LACVP**)/MM data[89] for the PPIX,SCys system; B3LYP/LACVP-DZ data[132] for the large Por,SH system of Figure 10. Relative energies (kcal mol^{-1}) of the two isomers and geometric features for ^{2}**6**$_{\mathrm{iso}}$ are from the first two sources in the same order as above. (Reprinted with permission from ref 37. Copyright 2004 Kluwer Academic/Plenum Publishers.)

affinity of 334[145] or 330.1 kcal mol^{-1} [80,81] and is expected to accept a proton and collapse to Cpd I without a barrier.[82] EPR/ENDOR studies of Davydov et al.[113] showed that in the T252A mutant of P450$_{\mathrm{cam}}$ Cpd 0 is still formed but no camphor hydroxylation occurs, thus suggesting that the mutation of Thr$_{252}$ prevents the formation of Cpd I. Our recent studies using the large protonation models (see Figure 10 for the situation in the wild-type enzyme) for the T252A and D251N mutants show that the first protonation step to form Cpd 0 still occurs in the mutants but the subsequent protonation to form Cpd I encounters difficulties.[132] Therefore, it appears that the protonation mechanism leading to **6** differs from the one leading to **7**. The latter process in P450$_{\mathrm{cam}}$ is believed to take place due to a sequestered hydronium ion between Asp$_{251}$ and Thr$_{252}$.[116] This process was theoretically modeled by Kamachi and Yoshizawa[104] using B3LYP/LanL2DZ (see Figure 12a). Two water molecules are sequestered between the carboxylic acid group of Asp$_{251}$, the hydroxyl group of Thr$_{252}$, and Cpd 0. The hydroxyl group of Thr$_{252}$ directly donates a proton to Cpd 0, leading to the formation of Cpd I and departure of a water molecule. This process was found to be exothermic by 13.1 and 5.5 kcal mol^{-1} for the quartet and doublet spin states, respectively. The overall reaction starting from the species ^{4,2}**5** and leading to Cpd I (^{4,2}**7**) was found to be exothermic by 74.6 (55.6) kcal mol^{-1}, but no reaction barriers were reported.[104] However, the calculations of de Visser et al.[132] indicate that the hydroxyl group of Thr$_{252}$ cannot be deprotonated in the presence of neighboring water molecules. This casts doubt on the proposition in Figure 12a. Further doubt comes from the experimental observation that mutation of the OH group of Thr$_{252}$ to a methoxy group still leads to camphor hydroxylation.[155] Therefore, it is very likely that Thr$_{252}$ itself does not participate in the mechanism as the protonating acid.

Figure 12b outlines an alternative protonation mechanism of Cpd I formation suggested by de Visser et al.[132] The mechanism starts from the two conformers of Cpd 0 (^{2}**6** and ^{2}**6′** in Figure 10). We recall that these structures were formed from ^{2}**5** by a proton-relay mechanism from Glu$_{366}$ (^{2}**6**) or by rotation of Asp$_{251}$ followed by protonation (^{2}**6′**). One does not know if Glu$_{366}$ and Asp$_{251}$ get protonated again after the first proton transfer and if they do so fast enough. Thus, logical starting points are the situations obtained after the first proton transfer from either Glu$_{366}$ or Asp$_{251}$. Thus, Figure 12b investigates the role of Asp$_{251}$ rotation−protonation of ^{2}**6** as well as the protonation of ^{2}**6′** from Glu$_{366}$, where in each case the other acid is deprotonated. As can be seen, the protonation of Cpd 0 involves small barriers, similar to the ones reported in Figure 10. In the two mechanisms the initial intermediate is the protonated Cpd 0 (H$_2$O−O−Fe complex, ^{2}**6**$_{\mathrm{prot}}$) that undergoes O−O bond cleavage to produce Cpd I. The processes leading from Cpd 0 to Cpd I are slightly endothermic and become even less endothermic with the inclusion of a dielectric medium with a dielectric constant of 5.7. The overall protonation process from ^{2}**5** to ^{2}**7**, however, is exothermic (by -27.3 kcal mol^{-1}) but much less so than reported by Kamachi and Yoshizawa.[104] The DFT(ROB3LYP)/MM results of Guallar and Friesner[89] also indicate a highly exothermic process, but no precise data appear in the paper. In both of these latter studies the proton is transferred directly from the hydroxyl group of Thr$_{252}$. In view of the results of de Visser et al.[132] and the experiments of Kimata et al.[155] with a methoxythreonine mutant that lacks a hydroxyl group and nevertheless performs hydroxylation, the direct protonation by Thr$_{252}$ would seem unlikely. One surprising finding of the study by de Visser et al.[132] is the appearance of a stable protonated Cpd I species, ^{2}**6**$_{\mathrm{prot}}$ in Figure 12b. Such a species has never been detected by experiment. Whether it is a real feature of the catalytic cycle or an artifact of the truncated model will have to be seen by future DFT(B3LYP)/MM calculations.

3.8.1. Protonation Mechanisms in the T252A and D251N Mutants

B3LYP/LACVP-DZ calculations using the T252A and D251N mutants showed that these mutants will be able to form Cpd 0 from ^{2}**5** with similar barriers as the wild-type (WT) enzyme.[132] However, the situation in the T252A mutant suggests that the formation of Cpd I could indeed be slowed. The structure of Cpd 0 in the T252A mutant is shown in Figure 13 after protonation of the terminal oxygen atom via the Asp$_{251}$ rotation mechanism (Figure 10). It is seen that the mutation changes the hydrogen-bonding situation drastically, and the water channel from the Glu$_{366}$ side is now 4.13 Å away from the distal oxygen of **6**, whereas in the WT enzyme the hydroxyl group of Thr$_{252}$ bridges the gap between the water channel and the distal oxygen of **6**. If an additional water molecule enters this space, it may lead to formation of Cpd I, but this may be slow compared with uncoupling reactions (e.g., departure of HOO$^-$ or proximal protonation and formation of H$_2$O$_2$). Further

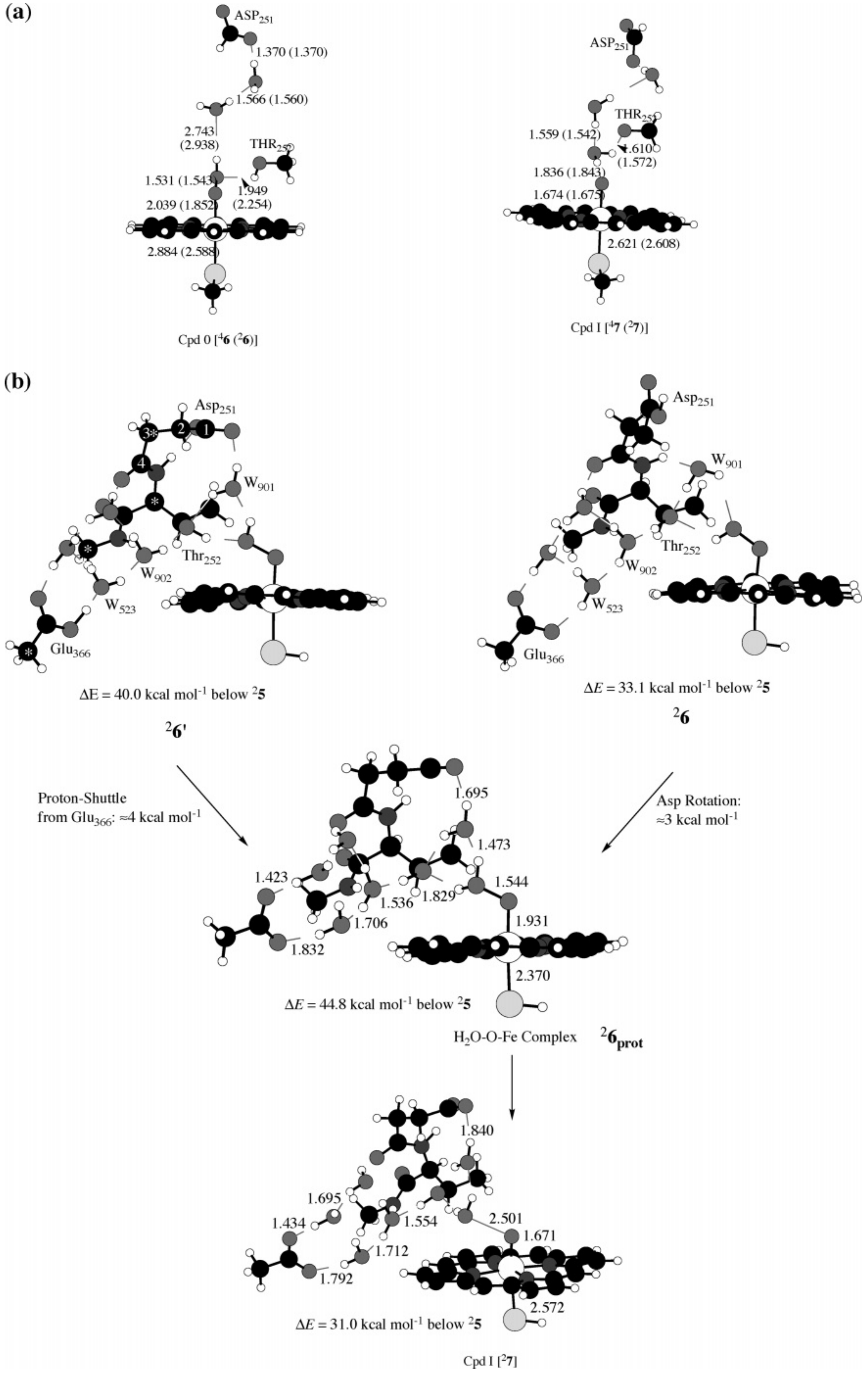

Figure 12. Hydrogen-bonding setup for Cpd 0 and the protonation mechanisms leading to Cpd I: (a) DFT(B3LYP)/LanL2DZ data for the Por,SMe model from ref 104 and (b) DFT(B3LYP)/LACVP-DZ data from ref 132. At the best level (ref 132b), LACV3P++**//LACVP* (with ZPE and solvation corrections), the relative energies for $^2\mathbf{6}'/^2\mathbf{6}_{\mathrm{prot}}/^2\mathbf{7}$ are 0.0/12.6/3.1 kcal mol^{-1}, respectively.

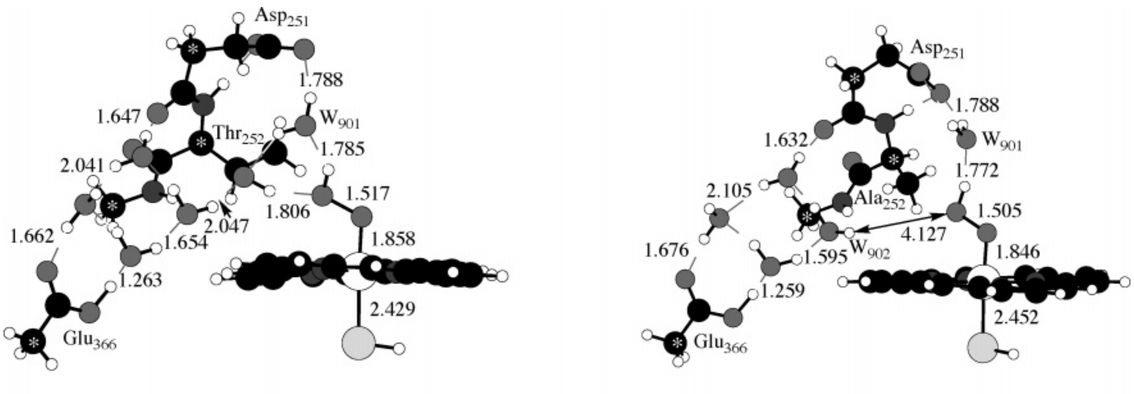

^{2}**6** (WT) ^{2}**6** (T252A Mutant)

Figure 13. Structures of Cpd 0 (for the large Por,SH model) within its environment for the T252A mutant and the wild type (WT) (taken from ref 132).

studies to ascertain the impact of these changes in the mutant are in progress.

3.8.2. Formation of the Ferric–Hydrogen Peroxide Complex

The protonation of Cpd 0 (**6**) on the proximal oxygen leads to formation of the hydrogen peroxide complex; the hydrogen peroxide may then dissociate. The hydrogen peroxide produced by this decoupling reaction in the pocket can be exchanged for a water molecule, which sends the system back to the resting state. Formation of the ferric−hydrogen peroxide complex was found to require only 6 kcal mol^{-1} more energy than formation of Cpd I,[145] so that the competition between these two processes depends on small energy differences. Of course, the formation of the ferric−hydrogen peroxide complex also depends on the availability of suitable protonation machinery. As shown in Figures 10 and 12b, the proton transfers originating from Glu$_{366}$ and Asp$_{251}$ maintain hydrogen-bonding interactions between the terminal OH group of **6** and the hydroxyl group of Thr$_{252}$ and W$_{901}$. On the other hand, the distal oxygen atom does not seem to be engaged in hydrogen bonding, and this may explain why decoupling is not prominent in the WT enzyme. However, mutations may distort the protonation machinery and connect the distal oxygen atom with a proton source, leading to decoupling instead. Clearly, the protonation story is far from being complete or understood and will await an extensive DFT/MM study.

3.9. “Push” Effect on the O–O Cleavage Process

The crucial factor in the O−O bond-breaking process is considered to be the donor strength, i.e., the “push” effect of the thiolate ligand.[3] Ogliaro et al.[81] calculated the proton affinity of a Cpd 0 system with and without the thiolate ligand and found an increase of 81 kcal mol^{-1} in the presence of thiolate. The “push” effect of the thiolate ligand thus regulates the thermodynamic driving force of the protonation machinery by raising the proton affinity, so that moderate acids, as those present in the protein pocket, can participate in the protonation process. This “push” effect was analyzed and found to involve a large electrostatic and a smaller quantum mechanical contribution. The former originates from the negative charge of the ligand, while the latter is the result of mixing of the σ_S sulfur orbital with the a_{2u} porphyrin orbital (see this orbital in Figure 4 above).

The “push” effect not only regulates the protonation but also prevents Cpd 0 from reduction. Thus, Ogliaro et al.[81] calculated a highly endothermic reduction energy of 43.3 kcal mol^{-1}, which turned into an exothermic reduction energy of −35.1 kcal mol^{-1} after removal of the thiolate ligand. This is mainly due to the large field effect of the negative charge on the thiolate. Moreover, the “push” effect causes Cpd 0 to prefer protonation rather than reduction. This was also noted in the study of Rydberg et al.[79]

3.10. Cpd I (7): A Chameleon Species

As mentioned above, Cpd I is elusive in the sense that it does not accumulate in the cycle. Its presence as a transient species was inferred by cryogenic and electronic absorption studies[156−158] and from cryogenic EPR/ENDOR spectroscopy of the alcohol product of camphor hydroxylation starting from deuterated camphor at the C^5−H position.[113] A recent mechanistic study by Dowers et al.[159] used a surrogate oxygen-atom donor to hydroxylate substituted *N*,*N*-dimethylamines and demonstrated that the only competent oxidant in the reaction was Cpd I. Recent X-ray structural evidence for the existence of Cpd I[28] seemed initially very convincing but has subsequently been cast in doubt.[113] The elusiveness of Cpd I has prompted suggestions for alternative oxidant species. One such proposal by Hata et al.[160,161] is the Fe−OH$_2$−O complex, i.e., the ferric−water oxide complex intermediate. Since this species is very high in energy and there does not seem to be a convenient double-protonation mechanism for the proximal oxygen,[132] it does not appear to be a viable solution for the enzyme. Another alternative is Compound II (Cpd II), which is the one-electron reduced species of Cpd I.[80,81,162] Attempts to shunt the cycle by use of peroxyacids followed by EPR detection invariably led to the formation of Cpd II and a protein radical (usually tyrosine).[163−165] However, recent studies on model systems[166−168] imply that while Cpd II species can carry out both C−H hydroxylations and C=C epoxidations, they are still sluggish compared with the corresponding Cpd I species. As such, most of the experimental community views Cpd I as the primary if not sole oxidant species in the cycle.

Because of the uncertainty regarding Cpd I, theory can contribute fundamentally to this area. However, theoretical calculations on Cpd I models in a vacuum led to controversial results about the electronic ground state. In particular, the results depend very much on the choice of the axial ligand. Still, all calculations agree that Cpd I possesses three singly occupied orbitals including the π^*_{xz} and π^*_{yz} orbitals (Figure 4) which give rise to two closely lying spin states, doublet and quartet. In the early CASSCF calculations of Cpd II the two π^* orbitals are also singly occupied.[30] The nature of the third singly occupied orbital, however, appears to depend on the chosen thiolate model and on the interactions of the sulfur atom with the environment.[33,79,83,112,122,131,169–177] In cases, where the cysteinate was modeled by SMe[79,172,173] or SCys without internal hydrogen bonding,[176] the third unpaired electron resides in a π_S lone-pair orbital on the sulfur, giving a $^{4,2}\Pi_S$ ($\pi^*_{xz}{}^1\pi^*_{yz}{}^1\pi_S{}^1$) electronic ground state with a large spin density located on the sulfur ligand and hardly any on the porphyrin ring. By contrast, the choice of SH^- or cysteinate with internal hydrogen bonding leads to $^{4,2}A_{2u}$ electronic states where the a_{2u} porphyrin orbital is singly occupied ($\pi^*_{xz}{}^1\pi^*_{yz}{}^1a_{2u}{}^1$) with spin densities distributed between porphyrin and sulfur. Moreover, with the HS^- ligand the $^{4,2}\Pi_S$ states were found to lie 5 kcal mol^{-1} higher in energy than the $^{4,2}A_{2u}$ states, while with SMe^- all the states are condensed within 1 kcal mol^{-1}.[34,91,122] One must remember that if the ground state of Cpd I had been a $^{4,2}\Pi_S$ state, i.e., with closed-shell porphyrin, it would have looked red, while all known $^{4,2}A_{2u}$ states give a green color. Experiment[178] shows that for chloroperoxidase, which is a thiolate enzyme like P450, the corresponding Cpd I is “green”.

Furthermore, the Fe–S distance was found to depend on the nature of the electronic state and vary as a result of environmental perturbations which were modeled by NH---S hydrogen bonding and a dielectric constant to mimic the effect of the electric field of the protein.[112,171,177] The environmental effects on the geometry and spin densities of Cpd I are depicted in Figure 14, which shows the results of Ogliaro et al.[177] for the system (Por,SH), Rydberg et al.[79] for the system (Por,SMe), and Schöneboom et al.[83] for various QM/MM models. The latter study (Figure 14c) used DFT(B3LYP)/MM calculations of Cpd I of P450$_{cam}$ with different basis sets, three different representations of the cysteine ligand, and a few snapshots from equilibrated MD simulations.

It is seen from Figure 14 that, generally, the FeO moiety bears a spin density (ρ) of around 2 indicative of singly occupied π^*_{xz} and π^*_{yz} orbitals (see Figure 4). The third spin is distributed on the sulfur and porphyrin groups in a manner that varies with different environments and ligand representations. Thus, in the gas phase and without any external interaction, the species has a predominant thiolate radical character; only 44% (Figure 14a) or 24% (Figure 14b) of the spin density is on the porphine.

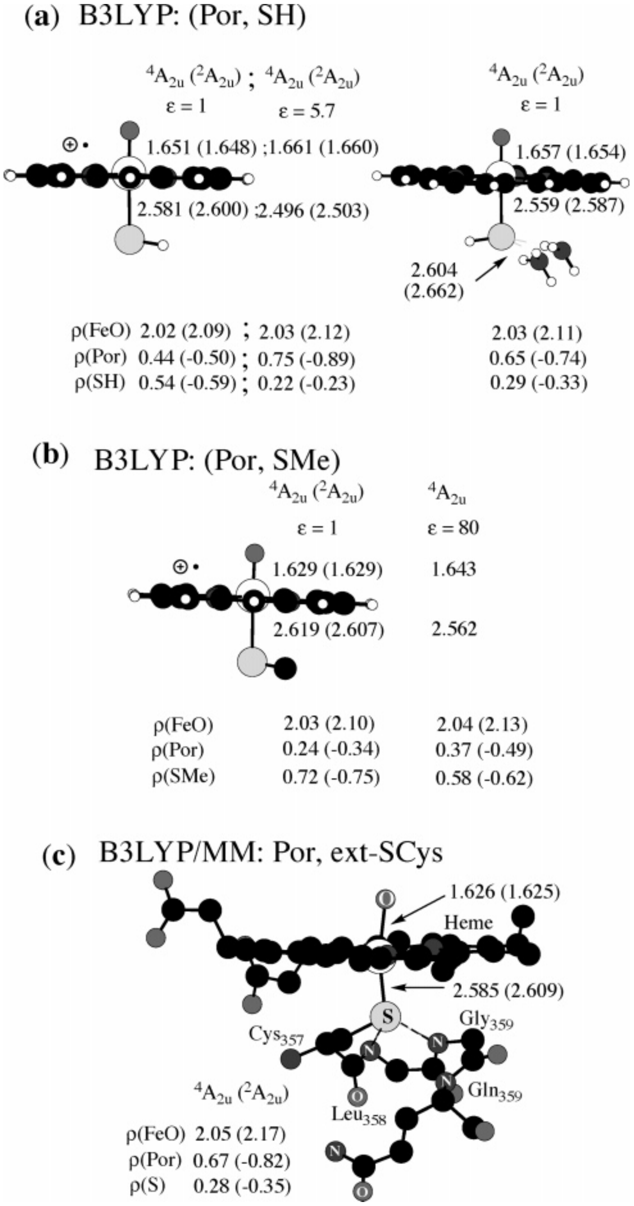

Figure 14. Environmental effects on geometrical parameters and group spin densities (ρ) of Cpd I: (a) model calculations in ref 177 with different dielectric constants ϵ and hydrogen bonding (NH---S), (b) model calculations in ref 79 with different dielectric constants ϵ, and (c) B3LYP/MM calculations in ref 83 for Por,ext-SCys with protein environment (basis set: LACVP for iron, 6-31+G* for the atoms coordinated to iron, and 6-31G for the remaining atoms). The study in c involves different representations of the proximal ligand, all showing the same trends.

External interactions with a dielectric medium (ϵ = 5.7) or NH---S hydrogen bonding (Figure 14a) shift spin density from sulfur to porphyrin; in the case of the Por,SH model, the species acquires a predominant porphyrin radical cationic character (65–75% in Figure 14a). These environmental effects are also found in the DFT(B3LYP)/MM calculations.[83] Thus, the gas-phase species all have predominant sulfur radical character, but in the protein environment Cpd I becomes a predominantly porphyrin radical cationic species (Figure 14c) irrespective of the proximal ligand representation as SH^-, $SCH_3{}^-$, or ext-$SCys^-$. The DFT(B3LYP)/MM calculations further assign the ground state of Cpd I as $^2A_{2u}$, with the $^4A_{2u}$ state lying

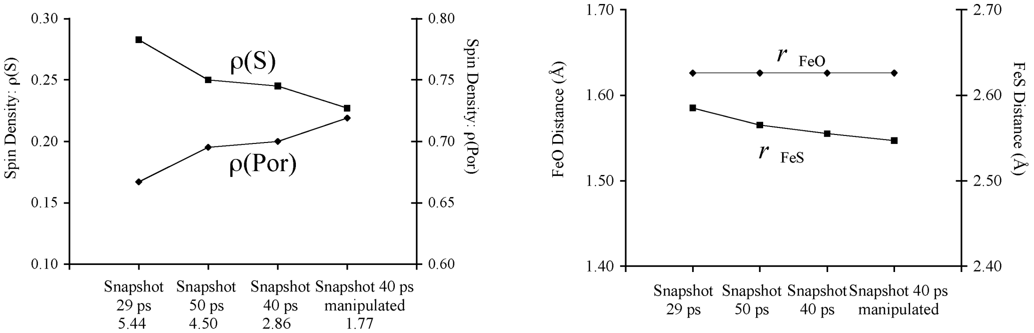

Figure 15. Changes in the spin densities (ρ) on thiolate (S) and porphine (Por) and in the Fe$-$S and Fe$=$O bond lengths as a function of the Gln$_{360}$NH---O$=$C(Cys357) hydrogen-bond distance. All distances are in Å. Data taken from ref 83.

very slightly higher, and this ordering persists irrespective of the proximal ligand representation and the chosen snapshot. Thus, Cpd I of P450$_{\text{cam}}$ resembles the known Cpd I species of chloroperoxidase;[178] it possesses a doublet ground state and should appear "green".

Further inspection of Figure 14 reveals that while most bond lengths stay virtually the same under all conditions, the Fe$-$S distance is shortened significantly by the external perturbation. Thus, relative to the gas phase, the Fe$-$S distance is shortened, in some cases by almost 0.1 Å. These geometric changes exerted by the environment were noted in DFT model studies[112,177] and confirmed by the DFT(B3LYP)/MM study of Cpd I in the native protein.[83]

In view of this sensitivity of the electronic structure and Fe$-$S bond length of Cpd I, Ogliaro et al.[112,177] characterized Cpd I *as a chameleon species* that can change its nature depending on external conditions.[112,177] This property is fleshed out by the DFT(B3LYP)/MM results in Figure 15, which shows the impact of the hydrogen-bonding situation of the cysteinate ligand on the electronic structure of Cpd I and its Fe$-$S bond length. Thus, the different snapshots used in the calculations differ primarily by the Gln$_{360}$ NH---O$=$C hydrogen bond from Gln$_{360}$ to the carbonyl group of cysteinate; the distance is defined in the abscissa of Figure 15. It is seen that as this hydrogen bond gets stronger and stronger, the spin density on the sulfur continually decreases with a concomitant increase in the porphine spin density. At the same time, the Fe$-$S bond length gets shorter and shorter. This shows that Cpd I indeed behaves like a chameleon species that changes its electronic character and Fe$-$S bonding situation in response to the interactions with the protein pocket, which accommodates the species.

The chameleonic nature of Cpd I can be described using the valence-bond (VB) models shown in Figure 16.[34,37,83,122,123,177] Two possible resonance structures contribute to the electronic structure of Cpd I, one in which the porphyrin is closed shell and the thiolate is a radical (state $|\mathbf{a}\rangle$) while the other (state $|\mathbf{b}\rangle$) is an ion pair with a cation radical on the porphyrin and a thiolate anion. In the gas phase $|\mathbf{a}\rangle$ is below $|\mathbf{b}\rangle$ and the energy separation depends mainly on the choice of the axial ligand, e.g., thiolate or methyl mercaptide, etc. However, a dielectric medium and/or hydrogen-bonding interactions will stabilize the ion-pair state $|\mathbf{b}\rangle$, possibly to the extent that it moves below $|\mathbf{a}\rangle$. In this case the mixed state becomes more $|\mathbf{b}\rangle$ like, having more spin density on the porphyrin. Moreover, as shown in Figure 16b, the Fe$-$S bond changes from a weak and long one-electron bond in the gas phase to a stronger and shorter two-electron bond in the protein. Therefore, Cpd I is a mixed-valent state, and as such its Fe$-$S distance and electronic properties depend on the hydrogen-bonding network and polarity of the surrounding enzyme.

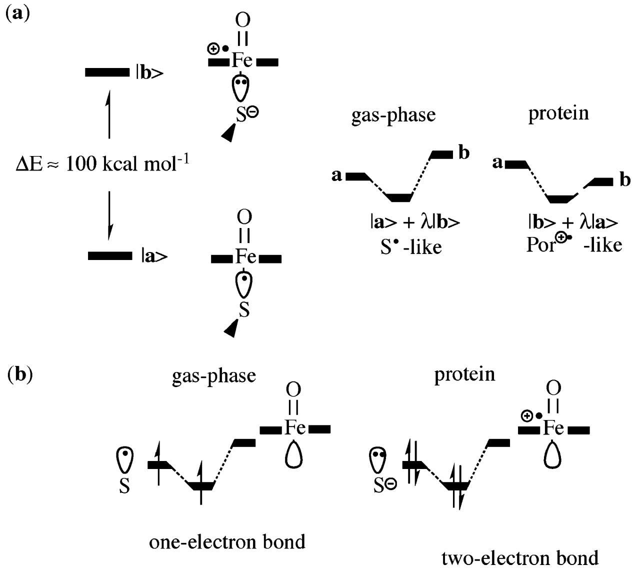

Figure 16. Valence-bond modeling for the influence of the protein environment on the electronic structure of Cpd I:[83,122,123] (a) valence-bond mixing of the contributing structures; (b) Fe$-$S bond orbital, its occupancy, and type of Fe$-$S bond, depending on the electronic situation of the sulfur.

A more recent DFT(ROB3LYP)/MM study by Guallar and Friesner[89] used a larger QM region, which included the propionate side chains, and found that there is considerable spin density on the propionate side chains, propionate A and D, as shown in Figure 17a. Extensive single-point test calculations by Schöneboom et al.[84] and Cohen[179] at their optimized structures did not find any significant spin density at the propionate groups whenever these are properly screened. One such structure is depicted in Figure 17b: the spin density on the propionates is zero *both in the gas phase and in the protein* as long as the propionates are screened by the arginines. It is noteworthy that the available experimental studies

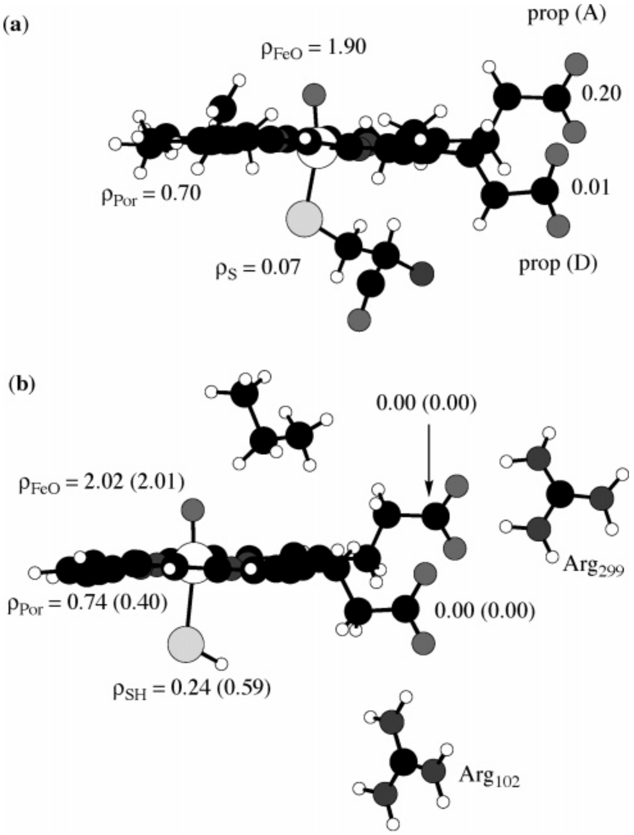

Figure 17. Cpd I species and its spin density: (a) data from ref 89 and (b) data from refs 84 and 179 for the enzyme (gas-phase data in parentheses).

do not report significant spin density on the propionates in other Cpd I species[34] including the case of CPO, which is analogous to P450.[178]

Apart from calculations of Cpd I of P450-type enzymes, results also have been reported on Cpd I species of analogous enzyme systems and catalysts.[42,79,123,171,174−176,180−184] These are however beyond the scope of this review and will not be discussed any further.

3.11. What Factors Make the Catalytic Cycle of P450 Effective?

The theoretical modeling summarized above has revealed several important features regarding the catalytic cycle of P450;[37,79,81,132] these include the “push” effect of the axial ligand, the hydrogen-bonding machinery of the proximal network that stabilizes Cpd I, and the protonation machinery (Thr, Asp, and Glu) that leads to Cpd I formation.

As discussed by Ogliaro et al.,[81] the gating of the cycle by a single water molecule is enabled by the strong electron-donor properties of the thiolate (cysteinate) ligand, i.e., “push” effect. Further into the catalytic cycle the “push” effect elicits the protonation processes of species **5** and Cpd 0 (**6**) and at the same time prevents reduction of these species. In the last step of the catalytic cycle the “push” effect prevents reduction of Cpd I, so *that it preferentially reacts by hydrogen abstraction or bond formation*. Green et al.[185] recently reached the same conclusion based on experimental investigations. Without the “push” effect the resting state (**1**), as well as species **5** and Cpd 0, would undergo reduction rather than following the catalytic cycle to form Cpd I; the latter would participate in electron-transfer reactions once formed. Thus, the thiolate ligand is responsible for the species-selective reduction and thereby creates a stable catalytic cycle.

The hydrogen-bonding network[104,132,151,152] provides a selective machinery for the protonation of **5** while leaving **4** intact, so that the protonation processes can start only after the second reduction step in the catalytic cycle and ultimately lead to Cpd I. The lack of hydrogen-bonding interactions with the proximal oxygen of Cpd 0 indicates[132] that, at least in the WT enzyme, the formation of Cpd I will be favored over hydrogen peroxide generation. Theory also retrieves[132] the experimental findings that the threonine residue Thr$_{252}$ is crucial. This threonine shuttles protons from acidic residues via waters to the ligated dioxygen and thereby plays a key role in the protonation. Its absence (e.g., in the T252A mutant) seems to disrupt this proton relay.

Another aspect is the involvement of two or more spin states in the cycle. As will be seen in the reactivity sections, this two-state character also shapes the reactivity patterns of the enzyme.

3.12. Miscellaneous Species

Many calculations on iron−porphyrin complexes have been performed with ligands that differ from those in the active species of the cycle, for instance, with distal ligands CO,[186] NO,[187,188] or H_2O_2[145] and with imidazole.[189] Calculations on other metal−porphyrin systems were reviewed by Ghosh[190] and Ghosh and Taylor.[40,41] Also reported were studies of oxo−iron porphyrin systems without axial ligand[191,192] and with different axial ligands[79,123] as well as oxo−manganese[180,193] and oxo−cobalt[194] systems. These are not discussed any further in this review.

4. QM and QM/MM Studies of P450 Reactivity Patterns

4.1. Mechanistic Issues and Controversies

The area of P450 reactivity is characterized by a few major unresolved questions that have emerged from experimental studies. These issues concern the nature of the reactive species and the actual mechanisms of oxygen transfer into organic substrates.

The primary reactive species of P450 enzymes is considered to be Cpd I, but this species has so far escaped full experimental characterization (see discussion above). Since there is considerable indirect evidence that a Cpd I species is present in the cycle,[113,159] it is customarily hypothesized that the species is elusive partly due to its high reactivity toward substrate oxidation. Theory can test this hypothesis.

Moreover, recent evidence has suggested the presence of a second oxidant species in the cycle of P450, and while the identity of this second species is unknown, Cpd 0 is generally considered to be the main candidate. The evidence for a second species is indirect and relies on experiments designed to disrupt the protonation machinery that leads to Cpd I. Thus, mutant enzymes in which the proton relay that converts Cpd 0 to Cpd I is disrupted by site-directed mutagenesis[195,196] exhibit different reactivity patterns compared with the WT enzyme, e.g., with 2-butenes the mutant yields more epoxidation products compared with C−H hydroxylation,[195] etc. More compelling evidence is the demonstration that while the T252A mutant of P450$_{cam}$[197] does not hydroxylate camphor, it is capable of epoxidizing the double bond of camphene, albeit more sluggishly than the WT enzyme. Since the catalytic cycle of T252A is thought to terminate at Cpd 0, this necessarily means that Cpd 0 is involved in the epoxidation of an activated double bond but that its reactivity is smaller than that of Cpd I. Curiously, the double mutant of P450$_{cam}$, T252A/D251N, in which the protonation machinery has been disrupted by mutations of both Thr$_{252}$ and Asp$_{251}$, shows partial activity in camphor hydroxylation.[158] Moreover, a recent mechanistic study[159] reports that oxidation reactions thought before to involve Cpd 0 are caused in fact by Cpd I. Thus, the participation of Cpd 0 is still a clouded issue, and theory can at least gauge the reactivity of Cpd 0 vis-à-vis Cpd I.

Other controversial issues are the major disagreements concerning the mechanism of C−H hydroxylation and some key processes in the enzyme.[196,198] The consensus mechanism of C−H hydroxylation by P450 enzymes is the "rebound" mechanism proposed by Groves and McClusky[199] and depicted in Figure 18a. The mechanism involves an initial hydrogen abstraction followed by a rebound of the alkyl radical, on the iron−hydroxo species, to form the ferric−alcohol complex. This mechanism accounts for the observation of a small but detectable stereochemical scrambling and a large kinetic isotope effect (KIE) for C−H vs C−D hydroxylation.

Initial measurements of the lifetime of the radical[200] derived from bicyclo[2.1.0]pentane indicated a short but finite lifetime. Subsequent studies of Newcomb et al.[196,201] with ultrafast radical clocks, however, cast the rebound mechanism into doubt. One of the typical substrates studied by Newcomb et al.[196,201] is shown in Figure 18b along with its corresponding rearrangement route, where the apparent radical lifetime (τ_{app}) is given by the inverse of the rate constant for radical rearrangement ($1/k_R$) times the ratio of rearranged (***R***) to unrearranged (***U***) product yields. These studies led to radical lifetimes of the order of 100 fs, which are much too short for a real intermediate. These short lifetimes rule out the presence of radicals and altogether question the validity of the rebound mechanism. Newcomb et al.[196,201] used also probe substrates, such as the one in Figure 18c, which can distinguish between radical and carbocationic rearrangement. The rearrangement pattern of this substrate suggested that the major reaction intermediate is in fact a carbocation. Therefore, Newcomb et al.[196,201] proposed that C−H hydroxylation proceeds via two oxidant species, Cpd I that leads to concerted oxygen insertion into the C−H bond and Cpd 0 that transfers an OH$^+$ species and generates a protonated alcohol that subsequently undergoes rearrangements typical of a carbocationic species. Very similar problems exist in most of the other reaction mechanisms, but these have not developed into such a focused controversy as in the case of C−H hydroxylation.

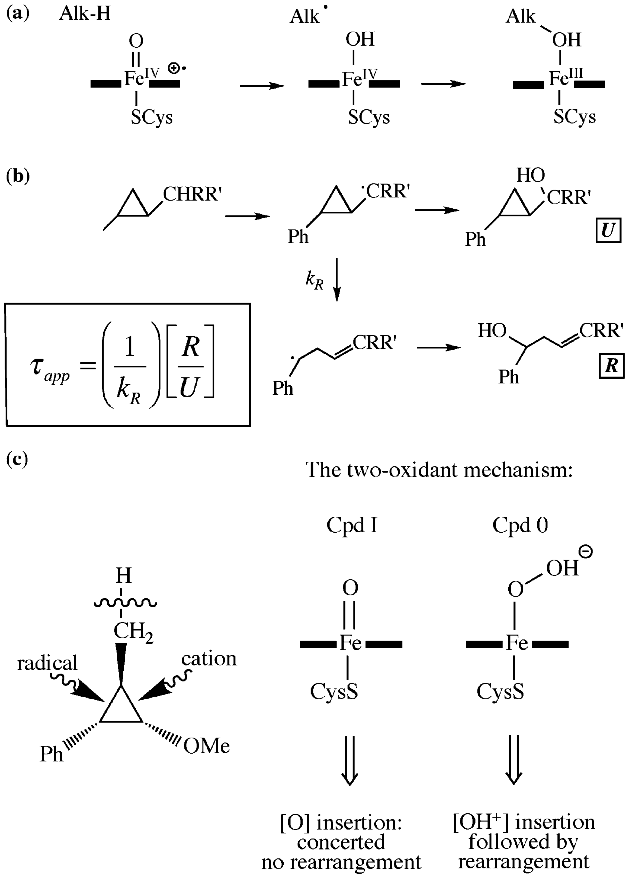

Figure 18. (a) Rebound mechanism.[199] (b) Apparent lifetime (τ_{app}) of a putative radical intermediate from the ratio of rearranged (***R***) to unrearranged (***U***) alcohol products produced from P450 hydroxylation of a substrate probe. (c) Probe that can distinguish between radical and carbocationic rearrangements, and the mechanistic proposal of C−H hydroxylation via two oxidants, Cpd I and Cpd 0.[196]

Theory has been able to complement experiment and shed light on these two main reactivity issues.[35−37,84,202] The following sections provide an updated description of the QM and QM/MM studies of the key reactions catalyzed by P450 enzymes, namely, C−H hydroxylation, C=C epoxidation, benzene hydroxylation, and sulfoxidation. As will be seen, Cpd 0 is a very sluggish oxidant that cannot compete with Cpd I, and hence the simultaneous action of Cpd I and Cpd 0 is not supported by theory. Most of the issues of the field can be understood as outcomes of the reactivity of a single reagent Cpd I with many pathways.[37,202]

As discussed above, the electronic ground state of Cpd I involves a close-lying pair of quartet and doublet spin states (labeled $^{4,2}A_{2u}$) characterized by singly occupied π^*_{xz}, π^*_{yz}, and a_{2u} orbitals. Both spin states will contribute to the reactivity with different reaction barriers and sometimes also different reaction mechanisms, which is characteristic of two-state reactivity, TSR.[35−37,203,204] Furthermore, since the

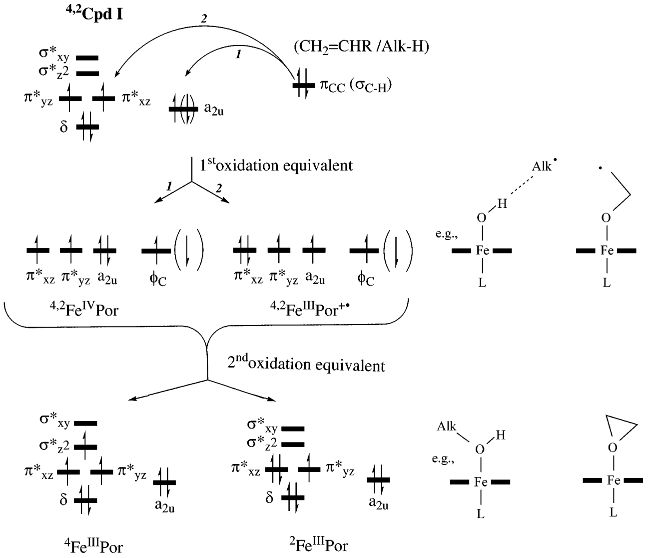

Figure 19. Oxidation states and orbital occupancy diagrams in various stages of reactions of Cpd I, e.g., during alkene epoxidation and alkane hydroxylation. Occupations within parentheses show the alternative spin arrangement, of the odd electron, in the corresponding doublet spin state. (Reprinted with permission from ref 37. Copyright 2004 Kluwer Academic/Plenum Publishers.)

orbital manifold of Cpd I involves several closely lying orbitals and gets denser along the reaction path, other states may also participate in the reactions and give rise to multistate reactivity (MSR).[106,202,205]

4.2. Guide to the Reactivity of Cpd I: Counting Electrons, Spin States, and Electromeric Situations

Before discussing the features of TSR and MSR, it is essential to outline the simple electron counting procedure that relies on the “oxidation state formalism” and is used fruitfully in inorganic chemistry. The major advantage of this formalism is that it enables one to assign the “right number of electrons” to the d-block orbitals of the metal.

The heme of Cpd I effectively contains an Fe^{IV} center and a hole in the porphyrin, (i.e., $Por•^+$), and thus has two oxidation equivalents more than the product state that has an Fe^{III} center and a closed-shell porphyrin. Thus, any reaction of Cpd I will ultimately involve two formal electron-“transfer” events from the substrate being oxidized to the heme. Figure 19 shows the changes in orbital occupancy during these processes, including the d-block orbitals, the a_{2u} orbital of the porphyrin, and the substrate orbital for C−H hydroxylation and C=C epoxidation. Each diagram shows the quartet and doublet spin states; the latter state is indicated using an inverse electron spin in parentheses. On top we give the orbital occupation of ^{4,2}Cpd I, while on the right-hand side we depict the relevant substrate orbital, i.e., π_{CC} is the orbital for the π bond, activated during epoxidation, and σ_{C-H} is the orbital for the C−H bond that is broken during hydroxylation.

The initial bond formation step involves an electron-“transfer” event from the substrate into Cpd I. Two possibilities exist for this “transfer”: (1) into the porphyrin hole (a_{2u} orbital) to generate an Fe^{IV}-type intermediate with a closed-shell porphyrin or (2) into the π_{xz}* orbital to generate an Fe^{III}-type intermediate with a radical cationic situation on the porphyrin ring. In both cases the substrate retains a radical center with a singly occupied orbital labeled ϕ_C. In addition, each of these two electromers will come in two spin varieties, so we might expect involvement of at least four radical intermediate states during the reactions.[36] During the second bond formation an additional electron is “transferred” from the substrate to fill either the a_{2u} orbital or one of the d orbitals of the iron. Filling the π_{xz}* orbital generates the doublet-spin ferric product, whereas filling of the $\sigma^*_{z^2}$ orbital leads to the quartet-spin ferric product. Of course, in synchronous reactions, both “electron-transfer” events will transpire in one step (see later the sulfoxidation mechanism).

It is apparent already from Figure 19 that there are other possible states which are obtained by redistribution of the electrons in this dense orbital manifold. For example, shifting electrons from the ϕ_C orbital of the radical intermediate center into one of the d orbitals will generate a variety of states in which the substrate is a cationic species (see later the C−H hydroxylation of *trans*-2-phenylisopropyl cyclopropane and the epoxidation of double bonds). Since the orbital manifold is dense, many of these states will be accessible and contribute to product formation. As such, *the reactivity of Cpd I will involve two spin states and possibly many electromeric states, hence TSR and MSR.*

4.3. Synchronous vs Nonsynchronous Mechanisms: Preferred Reactivity Paths of Cpd I

Before starting the discussion on TSR and MSR, let us first discard unfavorable reaction pathways. Quite long ago it was argued that the synchronous insertion of the oxygen atom of Cpd I into a bond is a forbidden process.[206] Indeed, a recent DFT(B3LYP)/LACVP-DZ study by de Visser et al.[108] demonstrated that the synchronous epoxidation of a double bond generates a high-energy species that has two imaginary frequencies (a second-order saddle point), as shown in Figure 20. One of these frequencies corresponds to a mode that stabilizes the structure by breaking the synchronicity of bond making and generates the transition state for the nonsynchronous processes, the species designated as TS_E in Figure 20. Furthermore, a DFT(B3LYP)/LACVP-DZ study of camphor hydroxylation by Schöneboom et al.[84] showed that a synchronous oxygen insertion into the C−H bond will require a barrier of ca. 50 kcal mol^{-1}, compared with $\leq$20 kcal mol^{-1} for the nonsynchronous process. Therefore, all subsequent mechanistic discussion will consider only the nonsynchronous processes.

4.4. DFT Studies of C−H Hydroxylation by Cpd I of P450: Two-State Reactivity (TSR)

Many DFT studies were performed to elucidate the mechanism of C−H hydroxylation and resolve the controversy around the radical clock data. The first few studies used methane as the substrate,[91,92,207]

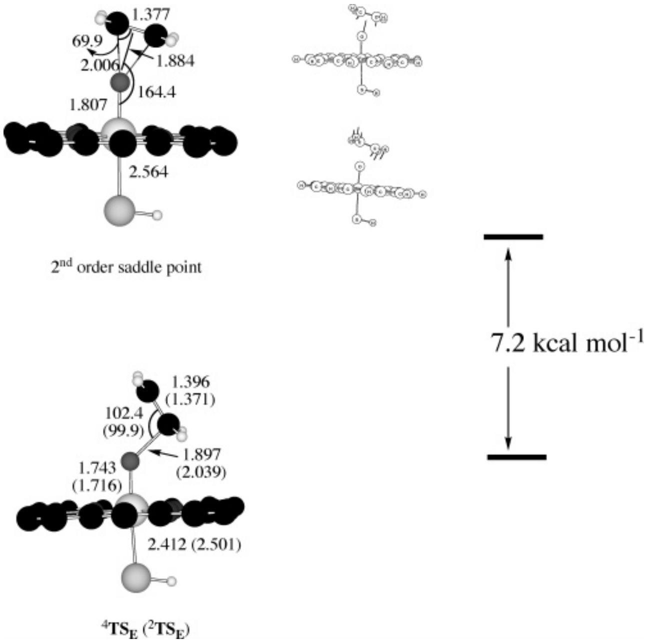

Figure 20. Transition states for the synchronous and nonsynchronous epoxidation processes of ethene. The synchronous process involves a second-order saddle point with two imaginary modes, shown in the figure. The rotational mode lowers the energy and leads to the real transition state (TS) for the nonsynchronous process. (Reprinted with permission from ref 108. Copyright 2001 The Royal Society of Chemistry.)

while later investigations employed more realistic molecules.[93−98,104] The most recent studies involve DFT/MM modeling of camphor hydroxylation by P450$_{cam}$.[84,86,89,90,179] Altogether, there are by now studies of more than 10 different substrates, which lead to a general and unified mechanistic picture.

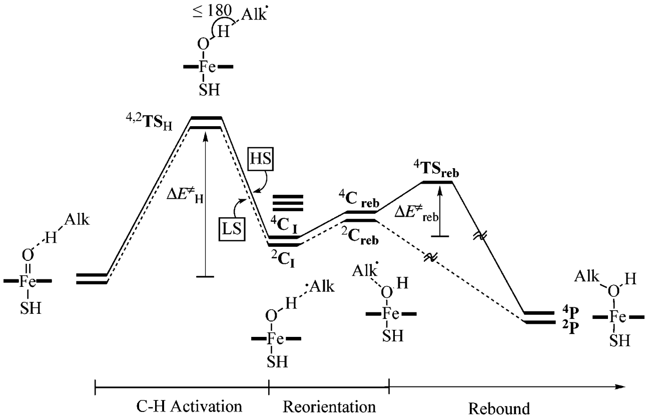

Figure 21. Typical reaction profile for C−H hydroxylation (Alk-H is the substrate) showing two-state reactivity (TSR) due to the closeness of the two spin-state profiles. After the bond-activation phase there are five intermediate states, which differ in the electromeric identity of the iron−hydroxo species (consult Figure 22). The lowest ones, labeled as $^{2,4}C_I$, participate in the rebound; the LS intermediate has a barrier-free rebound, while the HS species has a significant barrier via the $^4TS_{reb}$ species. This latter barrier is shown for one of the ^4C_I species that has the lowest barrier. (Reprinted with permission from ref 36. Copyright 2004 Wiley-VCH Verlag GmbH & Co. KgaA Weinheim.)

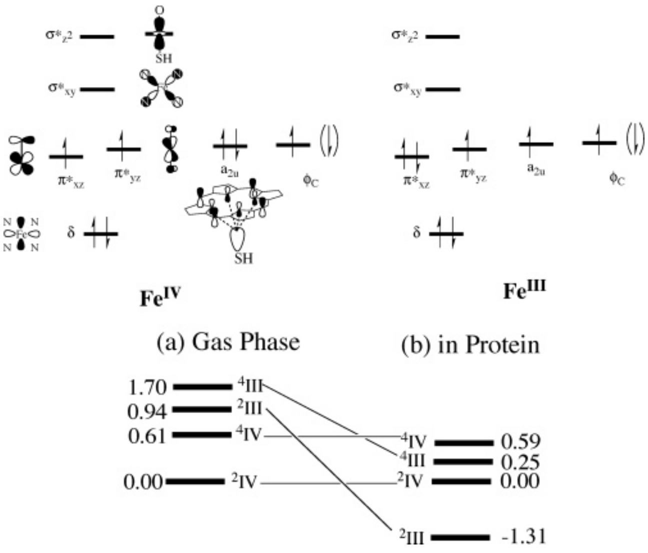

Figure 22. Orbital and occupation diagram for four out of five $^{2,4}C_I$ species at the rebound junction of Figure 21. There exists a second Por•$^+$Fe(III)/Alk• electromer with a doublet spin state and antiparallel spins in a_{2u} and π^*_{yz} orbitals. This state is not shown but is discussed in ref 36. (a) Relative B3LYP energies (kcal mol^{-1}) for camphor hydroxylation in the gas phase from ref 84 (see Supporting Information, section C3). (b) Relative DFT(B3LYP)/MM energies (kcal mol^{-1}) for the first four states in P450$_{cam}$, taken from the DFT(B3LYP)/MM calculations in ref 84 for snapshot 29 and R1/B1 model (see Supporting Information, section A).

A typical potential-energy profile for C−H hydroxylation is shown in Figure 21; this scenario emerged from numerous B3LYP calculations using the Por,SH model system (Scheme 1) for Cpd I[36,91] as well as from DFT(B3LYP)/MM calculations of camphor hydroxylation using a variety of snapshots, basis sets, and thiolate ligand representations.[84,179] The reaction coordinate exhibits three phases: a hydrogen-abstraction phase (bond activation), reorientation of the alkyl moiety to a rebound position, and a rebound process that generates the ferric−alcohol complex. The bond-activation phase involves the high-spin (HS) and low-spin (LS) bond-activation transition states ($^{4,2}TS_H$), which originate in the two spin states of Cpd I. The LS species ^2TS_H lies slightly below the HS one; generally, the two bond-activation transition states are close in energy to within 2 kcal mol^{-1} or less. This phase generates the clusters C_I, which involve an alkyl radical (Alk•) weakly coordinated to the iron−hydroxo species. As discussed above (Figure 19) and further specified in Figure 22, there exist five states that differ in the total spin (doublet and quartet), in the oxidation state of the iron and the porphyrin, and in the spin arrangement within the moieties. The energy ordering of these states depends on the environment (see four of these in Figure 22); in the gas phase the preferred species is the PorFe(IV)−OH/Alk• electromer, while the protein environment or a dielectric medium favor the Por•$^+$Fe(III)−OH/Alk• electromer. In any event, these states are energetically very close (within 4 kcal mol^{-1} or less) and expected to participate in the subsequent rebound step.[36,84] The reorientation phase brings the alkyl radical to a rebound position at a small energy cost of less than 1 kcal mol^{-1}, sometimes as small as 0.2−0.3 kcal mol^{-1}. Because of the flatness of the reorientational surface, usually this phase has not been studied in great detail with the exception of the DFT(B3LYP)/MM study of Schöneboom et al.,[84] wherein the rotational barrier was estimated as 0.3 kcal mol^{-1} based on two-dimensional mapping of the rebound surface. Subsequently, the spin states bifurcate; the LS state exhibits a barrier-free rebound, while the HS state has a barrier and a genuine transition state ($^4TS_{reb}$) for rebound. The rebound barrier was found to depend on the electromeric identity of the ^4C_I cluster; the PorFe(IV)−OH/Alk• species has the lowest barrier, while the Por•$^+$Fe(III)−OH/Alk• species has the highest one.[36]

It follows therefore that C−H hydroxylation involves interplay of HS and LS reactivities; the HS mechanism is truly stepwise with a normal radical lifetime due to the rebound barrier, while the LS profile is effectively concerted with a radical intermediate that has no barrier for rebound. By now the Jerusalem group has studied the hydroxylation reaction of Cpd I of P450 with the following substrates: methane,[91] ethane, propane, propene, benzene, toluene, ethyl benzene, camphor,[98] *trans*-2-phenylmethyl cyclopropane, and *trans*-2-phenylisopropyl cyclopropane.[95−97] Generally, the reaction mechanism follows the same profile as depicted in Figure 21 and only the relative energies vary.

B3LYP studies of C−H hydroxylation by Yoshizawa and co-workers[99−104] and Hata et al.,[161] using the Por,SMe model (Scheme 1), basically confirmed the TSR picture but reported notable differences compared with Figure 21. Figure 23 shows side by side the energy profiles for camphor hydroxylation using the Por,SH model (Figure 23a)[36,98,179] and the Por,SMe model (Figure 23b).[104] It is seen that the two studies describe TSR with a stepwise HS mechanism and an effectively concerted LS mechanism. However, while the Por,SH model leads to a LS below HS scenario, the opposite is the case for the Por,SMe model. The relative energies of the HS and LS states for the Por,SMe model (Figure 23b) seem a bit large. However, most importantly, the state ordering for the Por,SH model (Figure 23a) is in good accord with the DFT(B3LYP)/MM results of Schöneboom et al.[84] for camphor hydroxylation by P450$_{cam}$ irrespective of the modeling of the cysteinate ligand; the HS below LS situation obtained for the Por,SMe model in Figure 23b is in discord with these calculations. As already mentioned in the discussion of Cpd I, the situation in the enzyme environment is better represented in gas-phase calculations when using the SH$^-$ rather than the SMe$^-$ ligand.

4.5. DFT(B3LYP)/MM Studies of Camphor Hydroxylation by P450$_{cam}$

At the time of the writing of this review only two published DFT/MM studies of camphor hydroxylation exist. The DFT(B3LYP)/MM study of Schöneboom et al.[84] investigated the mechanism for four different snapshots after MD equilibration using two different models of the QM subsystem and two different basis sets. The results of this study are summarized in Figure 24 for one of these snapshots; other snapshots gave essentially the same picture and are therefore skipped.[86,179]

(a) Por, SH

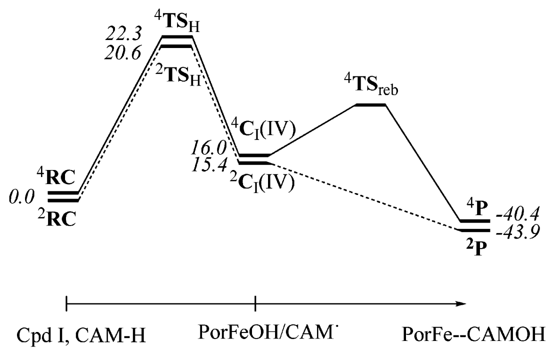

(b) Por, SMe

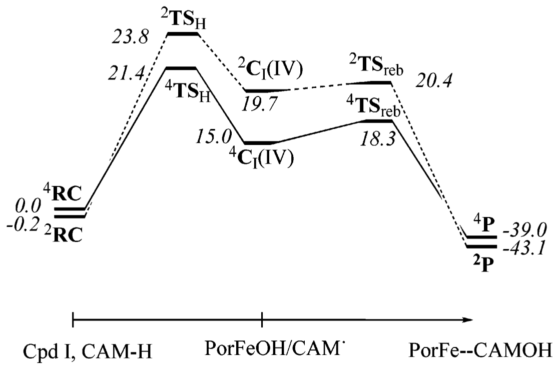

Figure 23. Reaction profile for camphor (CAM-H) hydroxylation by Cpd I models in the gas phase: (a) data from Cohen[179] for the Por,SH model, (b) data from Kamachi and Yoshizawa[104] for the Por,SMe model. The Cpd I models include camphor compared to Scheme 1. The label RC refers to the reaction cluster between Cpd I and camphor. The rest of the labels follow Figure 21.

The reaction (Figure 24a) starts from a reactant cluster of the two spin-state varieties ($^{4,2}\mathbf{RC}$) and follows essentially the same TSR profile as shown before (Figure 21) with an initial hydrogen abstraction from camphor (CAM-H) to form a radical intermediate ($^{4,2}\mathbf{C}_I$) followed by rebound to the alcohol product complexes ($^{4,2}\mathbf{P}$). The initial hydrogen-abstraction step is rate determining and requires an activation of ca. 20 kcal mol^{-1} (slightly less in the LS state than in the HS state). The rebound on the HS manifold encounters a significant barrier, while from the LS manifold the barrier is negligible, ca. 0.3 kcal mol^{-1}. The scenario is extremely similar to the gas-phase study described in Figure 23a using the small model, Por,SH. Furthermore, the geometries of the bond-activation transition states shown in Figure 24b exhibit similarities despite the different models and conditions (protein and gas phase). Thus, this study confirms the two-state picture that emerges from gas-phase model calculations using the small model representation, Por,SH.

The DFT(ROB3LYP)/MM study of Guallar et al.[89,90] considered only the initial hydrogen-abstraction step in the quartet state. It differs from the QM/MM work of Schöneboom et al.[84] in a number of aspects including the chosen DFT approach (ROB3LYP vs UB3LYP), the MM force field (OPLS vs CHARMM), the size of the overall system (7467 vs 24 394 atoms, without/with outer water layer), the treatment of surface

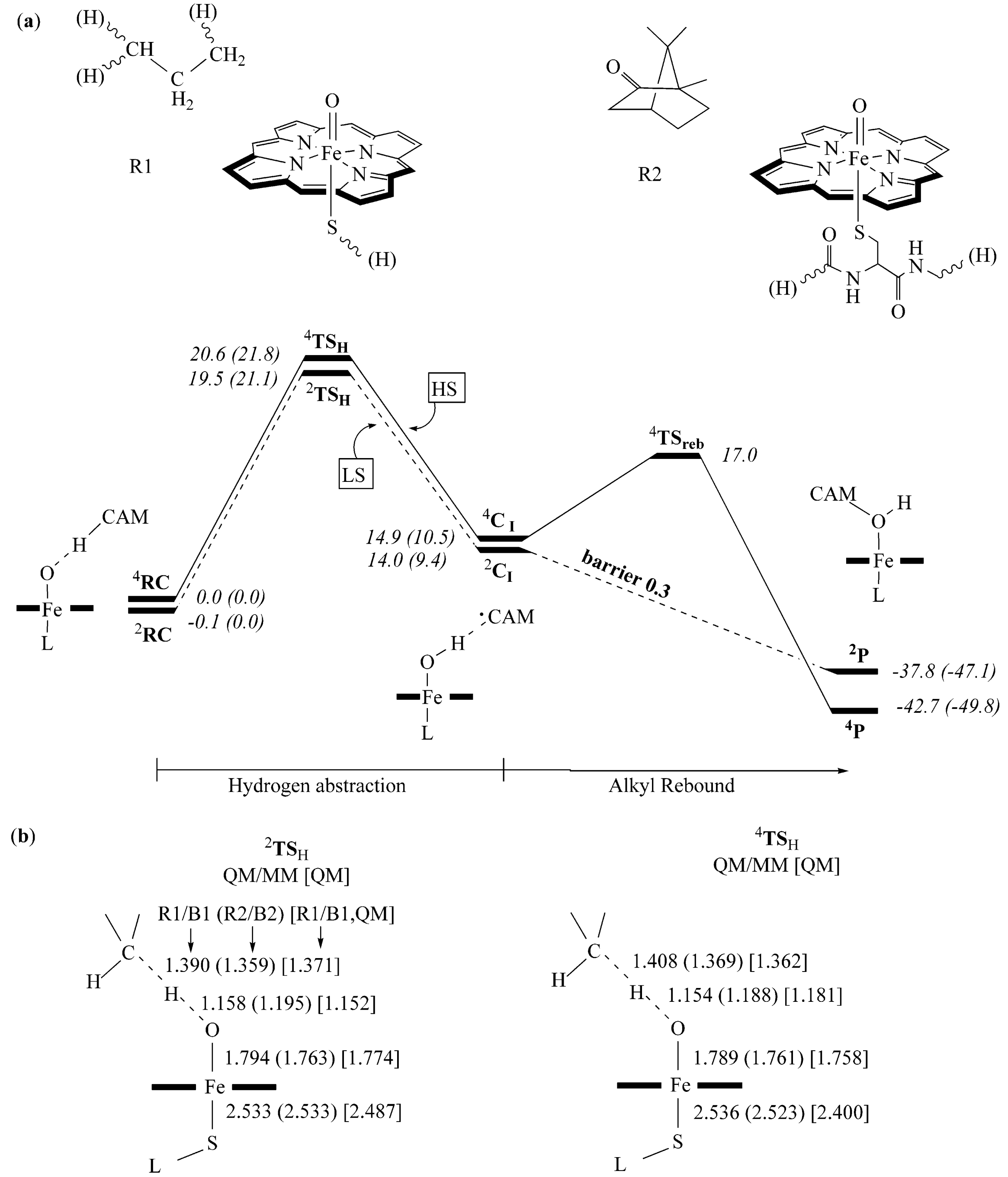

Figure 24. (a) Representative energy profiles describing camphor (CAM-H) hydroxylation by Cpd I of $P450_{cam}$ obtained by DFT(B3LYP)/MM calculations for the equilibrated snapshot 40 ps from Schöneboom et al.[84] The QM subsystems labeled as R1 (Por,SH) and R2 (Por,ext-SCys) are depicted near the profile. The energies out of parentheses correspond to R1 and the basis set LACVP-DZ. Data in parentheses correspond to the extended model, R2, using basis set B2. B2 involves LACVP-DZ augmented with a set of polarization and diffuse functions (6-31+G*) on the six atoms coordinated to iron and on the C^5 atom of camphor as well as on the hydrogen in transit (6-31++G**). (b) Key geometric parameters for the HS and LS transition structures for C−H activation. Data out of parentheses correspond to R1/B1 and in parentheses to R2/B2. The data in square brackets corresponds to R1/B1 in the gas phase.

residues (neutralized vs charged and screened by water), the size of the QM region (with/without heme side chains), the handling of the QM/MM boundary (frozen orbital vs link atom approach), and the starting points for QM/MM geometry optimization (X-ray structure vs several snapshots from MD trajectory). Figure 25 shows the energy profile obtained for the hydrogen-abstraction reaction from camphor in the HS state with a low barrier of 11.7 kcal mol^{-1}, leading to a rather stable intermediate lying only 4.5 kcal mol^{-1} above the reactant complex.[89,90] According to Guallar et al., the propionate side chain carries some spin density which decreases during the reaction (see Figure 25) with a concomitant increase of negative charge at the propionate. It is proposed that this buildup of negative charge will stabilize the transition state as well as the intermediate through electrostatic interactions with the positively charged

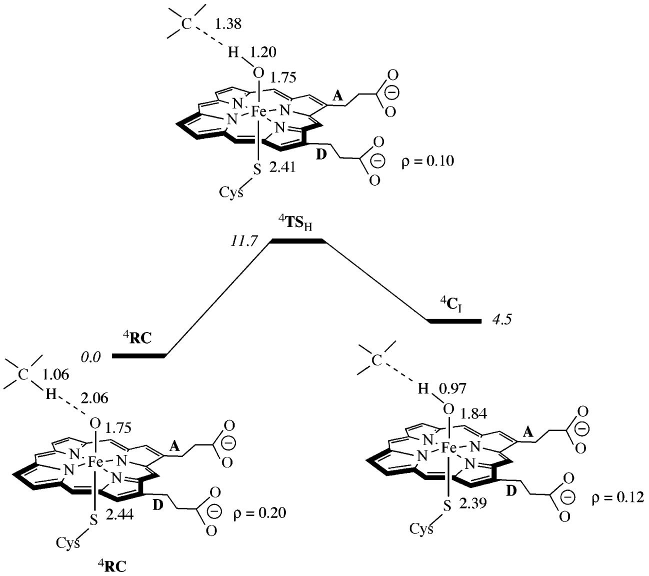

Figure 25. HS state DFT(ROB3LYP)/MM energy profile (QM region PPIX,SCys). The relevant structures are shown underneath the figure along with spin densities (ρ) on the propionate side chain. Data taken from Guallar et al.[89,90]

Arg_{299} group, thereby causing a lowering of the barrier and of the reaction energy.

To check this hypothesis, Schöneboom et al.[84] and Cohen[179] performed single-point test calculations with large QM regions at their optimized structures. These tests show that as long as the propionate side chains are properly screened by Arg_{299}, the side chains have zero spin density. Figure 17 gives the situation in Cpd I, while Figure 26 addresses the effect of the salt bridges in the reactant cluster, ^{4}RC, and the transition states, ^4TS_H. It is seen that inclusion of the side chains into the QM subsystem results in spin density accumulation on propionate A in the gas phase (results in parentheses), but all the spin density vanishes in the presence of the protein (results out of parentheses). Adding the salt bridges to the QM subsystem (Figure 26c) screens the propionates and eliminates any spin density for the gas-phase structures and for the structures in the protein environment. Furthermore, the presence or absence of propionate spin density does not lower the barriers in these calculations (compare barriers to Figure 23). QM/MM geometry optimization did not change these conclusions.[179]

In view of the technical differences between the two published QM/MM studies (see above), some deviations in the results are inevitable, but it is still disconcerting to see such large discrepancies in the computed barriers (12 vs 20 kcal mol^{-1}) and qualitative differences in the computed spin densities. Clearly these issues need to be resolved, and corresponding work has started.[208] At the time of writing, there are only a few preliminary results: Reoptimizations with tighter convergence criteria increase the reported DFT(ROB3LYP)/OPLS barrier[89,90] of 11.7 kcal mol^{-1} by about 2 kcal mol^{-1}.[208] Starting from an independent new system setup with an outer water layer and without neutralizing charged surface residues, DFT(ROB3LYP)/OPLS calculations still find spin density on the propionate group but a rather large barrier of 17.8 kcal mol^{-1}.[208] Using this setup and exactly the same geometry, DFT(UB3LYP)/CHARMM computations also give a small amount of spin density at the propionate group but the barriers are again quite high, more than 18 kcal mol^{-1}. A direct comparison of the geometries used in the two independent QM/MM studies shows that different protonation states have been assigned to several residues (e.g., His_{355}), but these were found to have no significant effect on the barriers. However, starting from the X-ray geometry[28] led to somewhat lower barriers, on the order of 16 kcal mol^{-1}. Further work is in progress to clarify these and related issues.[208]

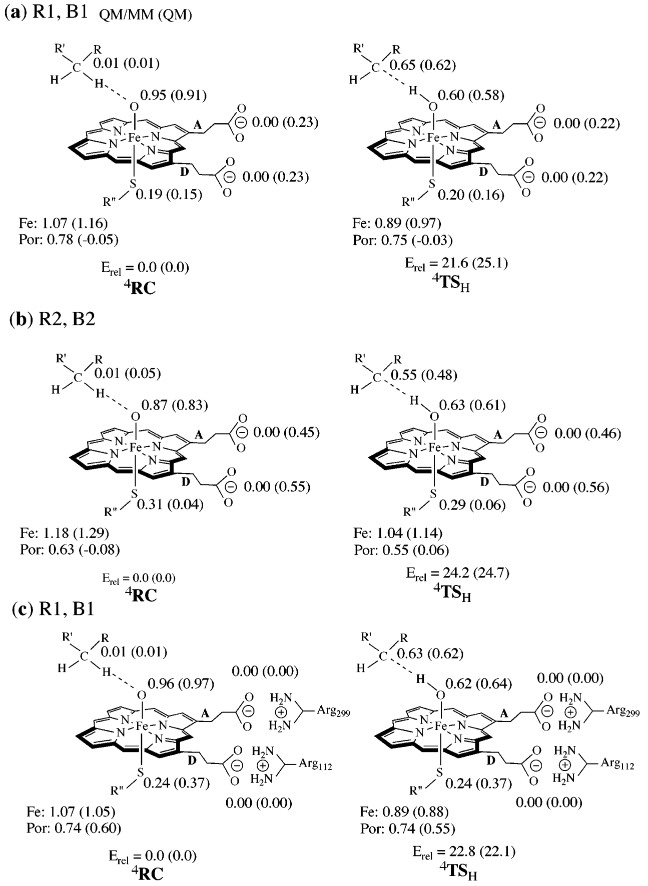

Figure 26. Effect of salt bridges to the heme propionate side chains on the spin density distribution and relative energies (kcal mol^{-1}) in the HS state during camphor hydroxylation by $P450_{cam}$. Values in parentheses correspond to the gas phase and those out of parentheses to the protein. Data taken from Schöneboom et al.[84] The labels R1/B1, R2/B2 are explained in Figure 24: (a) single-point calculations on the R1/B1 system (snapshot 40 ps) with addition of propionates to the QM subsystem, (b) single-point calculations on the R2/B2 system (snapshot 40 ps) with addition of propionates to the QM subsystem, (c) single-point calculations on the R1/B1 system (snapshot 29 ps) with addition of propionates and arginine salt bridges to the QM subsystem. Similar results were obtained after geometry optimization.[179]

As mentioned before, Cpd I of $P450_{cam}$ continues to be an elusive species which has not yet been detected experimentally. The most straightforward explanation for this experimental fact would be a short lifetime due to a very low barrier to camphor hydroxylation, possibly on the order of 10−12 kcal mol^{-1} according to estimates in the experimental

Table 2. Calculated[a] DFT(B3LYP) C−H Hydroxylation Barriers ($\Delta E^{\ddagger}$), Their Zero-Point-Corrected Values, $\Delta E(ZPE)^{\ddagger}$, and the Corresponding Activation Enthalpies at 298 K ($\Delta H^{\ddagger}$) and Free Energies at 298 K ($\Delta G^{\ddagger}$) of Hydrogen-Abstraction Transition States

substrate	spin state	$\Delta E^{\ddagger}$	$\Delta E(ZPE)^{\ddagger}$	$\Delta H^{\ddagger}$	$\Delta G^{\ddagger}$	$\Delta E^{\ddagger}{}_{\mathrm{LACV3P+*}}$
methane[b]	HS	26.7	22.8	22.6	31.7	*l*
	LS	26.5	22.3	21.7	32.4	*l*
ethane	HS	21.6 (19.4[c])	17.9	17.7	28.8	20.5
	LS	20.4 (16.2[c])	16.7	16.2	28.8	19.1
propane[d]	HS	19.0	15.0	14.7	27.5	18.0
	LS	18.0	14.0	14.3	25.1	16.9
propane[e]	HS	21.8	18.1	18.1	28.5	20.8
	LS	20.6	16.7	16.1	29.1	19.1
propene[f]	HS	13.5	10.6	10.9	21.2	*l*
	LS	13.5	10.8	11.3	21.4	*l*
Me-probe[g]	HS	18.7	14.8	15.1	25.8	17.3
	LS	17.9	14.0	13.9	25.9	16.6
^{i}Pr-probe[h]	HS	15.9	12.2	12.6	23.8	15.4
	LS	15.2	12.1	12.6	23.2	15.5
camphor	HS	18.8 (18.0[i])	14.5	15.0	25.3	19.7
	LS	17.4 (20.2[i])	13.4[j]	13.2	27.4	16.0
benzene[k]	HS	29.1	25.5	26.0	34.6	28.7
	LS	28.5	25.7	26.1	35.4	27.0
toluene	HS	16.2	13.1	13.0	25.4	11.9
	LS	16.0	12.6	12.6	25.0	15.7
phenylethane	HS	21.8	17.8	17.6	30.0	21.0
	LS	19.7	15.8	16.0	27.3	17.1

[a] All data are in kcal mol^{-1} (see ref 98). Unless noted otherwise, these barriers correspond to the LACVP-DZ basis set and refer to separated reactants. [b] Reference 91. [c] Reference 99. [d] Hydrogen abstraction from propane leading to isopropyl radical. [e] Hydrogen abstraction from propane leading to *n*-propyl radical. [f] Reference 94. [g] *trans*-Methylphenylcyclopropane from ref 96. [h] *trans*-Isopropylphenylcyclopropane from ref 96. [i] Reference 104. [j] The $\Delta E^{\ddagger}$ barriers relative to the gas-phase reactant complexes are given for camphor in Figure 23. The corresponding $\Delta E(ZPE)^{\ddagger}$ values in the LS state are 16.5 (LACVP) and 15.1 kcal mol^{-1} (LACV3P+*).[179] [k] Barrier for hydrogen abstraction from ref 109. [l] These data are are not given due to convergence difficulties.

community. The DFT(UB3LYP)/CHARMM value of ca. 20 kcal mol^{-1} seems rather high in this context. One should not forget, however, that zero-point vibrational corrections reduce this value by about 4 kcal mol^{-1} because the contributions from one C−H stretching mode are lost at the transition state. Moreover, if tunneling is important this could further lower the effective barrier, maybe by as much as 3 kcal mol^{-1},[209] which would then lead to a value of ca. 13 kcal mol^{-1}. One should note, however, that the measured kinetic isotope effects (KIE) do not provide conclusive evidence for tunneling in P450$_{\mathrm{cam}}$: the KIE values for camphor hydroxylation (ca. 4−5)[210] are lower than those for norbornane hydroxylation (ca. 11)[211] and thus less indicative of tunneling. As a final caveat, one should also remember that DFT barriers are of limited accuracy: test calculations for the model system $\mathrm{FeO(NH_3)_4(SH)} + \mathrm{CH_4}$ have shown[84] that the B3LYP barrier for hydrogen abstraction remains in the range of 19−20 kcal mol^{-1} upon basis set extension; however, use of the alternative PBE0 hybrid functional lowers this barrier to 15 kcal mol^{-1}. Taking all these points into account, the DFT(UB3LYP)/CHARMM barrier would seem to be on the high side but not prohibitively so.

Having focused on differences in the computed QM/MM barriers in the preceding discussion, one should emphasize that the published QM/MM work on camphor hydroxylation[84,89,90] also agrees on a number of points. In both studies the protein environment stabilizes the Fe(III)Por$\bullet^{+}$ electromers such that they lie below the Fe(IV)Por electromers (see also Figure 22). Similarly, both studies find a hydrogen bond between camphor and Tyr$_{96}$. Schöneboom et al.[84] emphasized the role of this hydrogen bond in the rebound step, where it guides a rebound from the *exo* face of the camphor by restricting the movements of the camphoryl radical.

Finally, all gas-phase model calculations show a significant entropic contribution to the free-energy barrier (see Table 2) of hydrogen abstraction, which causes an increase of ca. 10 kcal mol^{-1} at 298 K due to the loss of translational and rotational degrees of freedom upon association of Cpd I and the substrate.[37,94] In enzyme catalysis this entropic penalty is absorbed into the substrate binding step, which is driven mainly by the expulsion of water molecules from the binding pocket.[37,84]

4.5.1. Product Release in C–H Hydroxylation of Camphor by P450$_{\mathrm{cam}}$

According to detailed low-temperature electron nuclear double-resonance (ENDOR) studies at 200 K, product formation occurs through three distinct hydroxycamphor-bound conformations.[113] The spectroscopic results suggest that the immediate product after hydroxylation corresponds to a nonequilibrium state, involving a more or less normal Fe−O distance (≈2 Å), and that the heme pocket then relaxes in two detectable steps to accommodate the anomalously long Fe−O bond of 2.67 Å, found in the crystal structure.[212] The long Fe−O bond in the equilibrium state is thought to be a compromise between favorable Fe−O interactions, on one hand, and unfavorable desolvation of the polar hydroxy group in the nonpolar protein pocket, on the other hand. In addition, the initial product seems to be the low-spin doublet state complex.[212]

To address these issues, Lin et al.[87] performed DFT(B3LYP/LACVP-DZ)/MM calculations on the

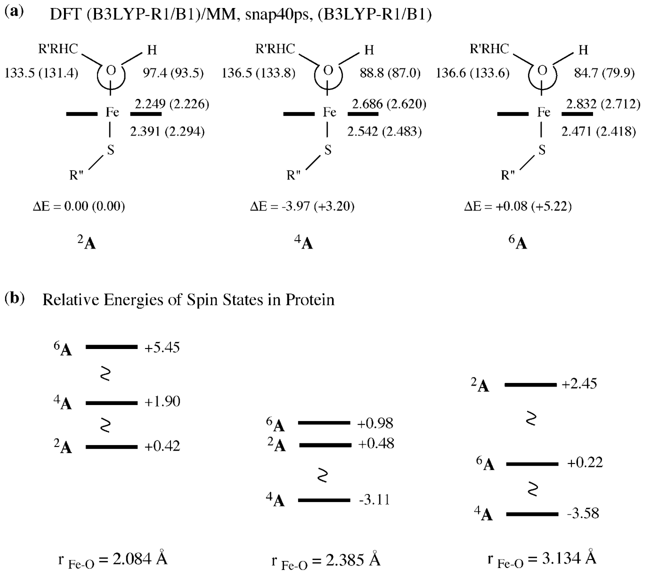

Figure 27. DFT(B3LYP/LACVP-DZ)/MM calculations for the R1 model of the 5-hydroxocamphor product complex in three low-lying spin states. (a) Selected geometric parameters and relative energies (kcal mol^{-1}) of optimized structures. Values in parentheses refer to the gas phase and those out of parentheses to the situation in the protein. (b) Relative energies (kcal mol^{-1}) of the three spin-state species at different Fe−O bond lengths. Data are taken from ref 87. Energies are given relative to the doublet minimum.

product complex in its different spin states and on the mechanism of Fe−O bond breaking (product release). The study used only a small QM subsystem (Por,SH) and one snapshot (40 ps).[84] The resulting geometry of the ferric complex of 5-hydroxocamphor corresponds closely to the crystal structure where 5-hydroxocamphor is bound through its carbonyl group by a hydrogen bond to Tyr$_{96}$ and otherwise by hydrophobic interactions with Phe$_{87}$, Val$_{295}$, Ile$_{295}$, and Val$_{396}$. The optimized geometries and relative energies of the three lowest spin states are shown in Figure 27a. In the gas phase the ground state is the doublet state, ^{2}A, while in the protein (out of parentheses) the global minimum is computed to be the quartet state ^{4}A; the sextet state ^{6}A is now very close to the doublet state. The stabilization of the higher spin states relative to the doublet, ^{2}A, is caused by the effect explained above for the resting state, namely, the hydrogen bonding to the thiolate ligand in the enzyme stabilizes the $d_{z^2}(\sigma^*)$ orbital which is occupied in the higher spin states.

Figure 27b shows the relative energies of these spin states at different Fe−O distances, in the protein environment. It is seen that at short Fe−O distances (2.048 Å) the lowest state is the doublet, but as the Fe−O bond is stretched, the quartet state crosses the doublet, and eventually at longer distance the sextet state also crosses the doublet. The stabilization of the hydroxocamphor by hydrogen bonding to the protein increases as the Fe−O bond gets longer (the hydrogen bond to Tyr$_{96}$ gets shorter in the process), and this balances the loss of bonding and makes the surface very flat. The results indicate that the initial product along the C−H hydroxylation pathway is the doublet species, ^{2}A, which is the lowest one at short Fe−O distances, ca. 2.2 Å. However, dissociation on the doublet surface requires very little activation (ca. 2 kcal mol^{-1}), and the system can undergo efficient intersystem crossing to the quartet during this process. The sextet state remains above the quartet state for the Fe−O distances considered in the enzyme (up to 3.13 Å).

The DFT(B3LYP)/MM results support the interpretation of the low-temperature ENDOR data[113] that the initially observed nonequilibrium species with a short Fe−O distance is a hexacoordinated product complex in the doublet state. The other two observed species with longer Fe−O distances could well correspond to pentacoordinated quartet and doublet minima with a relaxed protein environment, but a conclusive assignment is not possible in view of the flatness of the computed potential curves.[87]

4.6. Resolution of the Radical Lifetime Controversy by TSR

The TSR scenario provides a simple resolution of the controversy generated by radical clock data of Newcomb et al.[196] In a nutshell, TSR (Figure 21) involves interplay of two mechanisms; *the HS mechanism is stepwise with a normal radical lifetime, while the LS mechanism is effectively concerted with ultrashort ("zero" for the sake of simplicity) radical liftetime*. As such, the rearranged alcohol products will be produced only from the HS mechanism, while the unrearranged alcohol product will arise primarily from the LS mechanism. Thus, the [***R*/*U***] product ratio that is used to determine the apparent radical lifetime (τ_{app}, in Figure 18b) reflects the relative yield of the HS and LS surfaces rather than the lifetime of a single radical species that partitions between rearranged and unrearranged products.[35−37,91]

To test this hypothesis directly, Kumar et al.[95−97] carried out B3LYP studies of the hydroxylation mechanism of two clock substrates, *trans*-2-phenyl methyl cyclopropane and *trans*-2-phenyl isopropyl cyclopropane. The reaction profile for the first substrate is shown in Figure 28a, while the competition between radical rebound without prior rearrangement and the rearrangement process is shown in Figure 28b. Figure 28a exhibits the usual TSR scenario with LS below HS; the HS is truly stepwise with a barrier for rebound, while the LS is effectively concerted. In Figure 28b we see the competition between radical rearrangement and rebound, starting from the HS and LS radical complex intermediates (^{2,4}I$_U$). It is obvious that the HS radical complex has a smaller barrier for rearrangement compared with rebound. Therefore, the HS radical complex will give mostly rearranged alcohol product (***R***). By contrast, the LS radical complex has no barrier for rebound and a finite one for rearrangement, and hence the LS reaction will lead mostly, if not exclusively, to unrearranged alcohol product (***U***). It follows therefore that the quantity [***U*/*R***] reflects the relative yields of the HS and LS pathways and does not as such concern the partition of a single radical intermediate into ***R*** and ***U*** products, as assumed in the kinetic scheme in Figure 18b. In fact, a simple

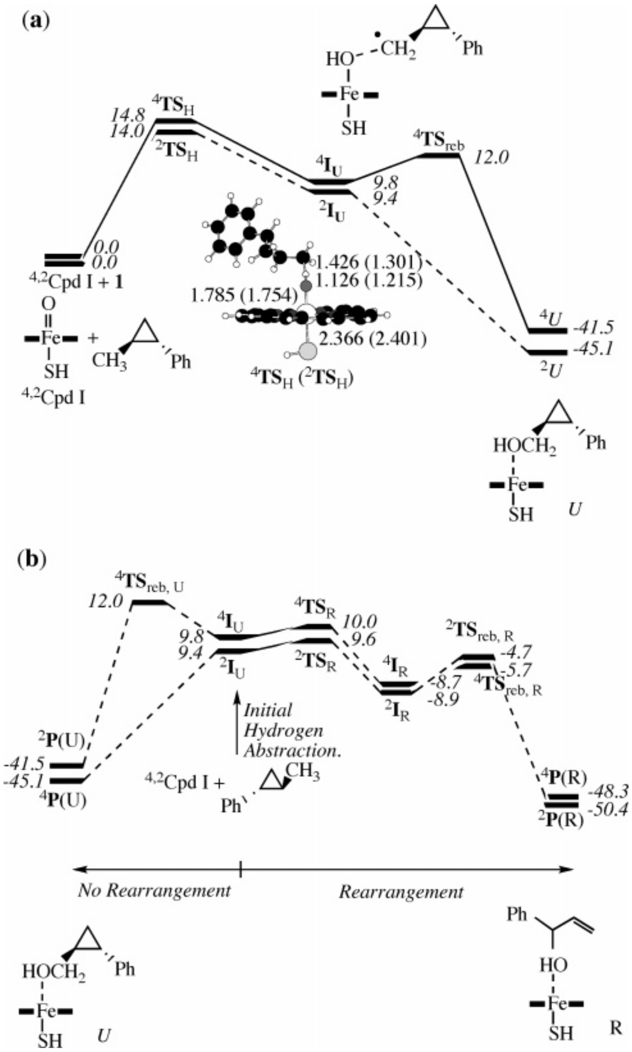

Figure 28. B3LYP/LACVP-DZ calculations of C−H hydroxylation of the *trans*-2-phenylmethylcyclopropane probe. The letters U and R represent, respectively, unrearranged and rearranged radicals and products. (a) TSR scenario for the bond-activation and rebound phases. (b) Competition of rearrangement and rebound without rearrangement for the HS and LS radical complexes, $^{4,2}I_U$. All energies (kcal mol^{-1}) are corrected for ZPE. The same conclusions were obtained with the LACV3P+*-6-311+G* basis set. (Reprinted with permission from ref 96. Copyright 2004 American Chemical Society.)

derivation shows that, in the general case, the ratio of the real radical lifetime (τ_{REAL}) on the HS manifold to the apparent lifetime (τ_{app}) in Figure 18b depends critically on the relative LS to HS yields, the quantity F in eq 1[35−37,91]

$$\tau_{REAL}(TSR)/\tau_{app} = \{[\boldsymbol{U/R}]\ (1 + F)\}/\{[\boldsymbol{U/R}] - F\} > 1;\ F = [\mathbf{LS/HS}] > 1 \quad (1)$$

Since the hydrogen-abstraction transition states ($^{2,4}\mathbf{TS}_H$) have generally a LS below HS ordering in both the DFT calculations[98] and the DFT(B3LYP)/MM study of camphor hydroxylation,[84,179] the value of F would be larger than 1,[91] and in some cases it can reach values of 10 or so.[93,94] Therefore, the apparent lifetimes will be short compared to the real lifetimes and become unrealistically short when the LS yield is much larger than the HS yield.

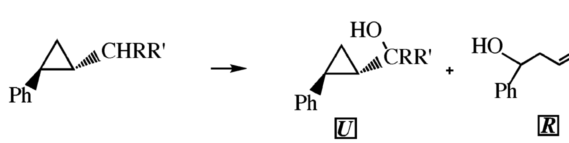

	Ar	R, R'	[*U*/*R*]
Donor Ability ↓	*p*-CF_3	H, H	4
	p-H	H, H	4.3
	p-CF_3	H, CH_3	12
	p-H	H, CH_3	25
	p-H	CH_3, CH_3	> 100

Figure 29. Experimentally determined ratios of unrearranged to rearranged alcohol products for a series of probe substrates. Note that the trend follows the relative donor ability of the radical center, as predicted by theory. (Reprinted with permission from ref 36. Copyright 2004 Wiley-VCH Verlag GmbH & Co. KgaA Weinheim.)

4.6.1. Rearrangement Patterns in P450 Hydroxylation

Using a simple rationale based on the electron count during the rebound on the HS manifold, it is possible to predict the trends in the extent of rearrangement in a series of related substrates.[35−37,91] From Figure 19 it is seen that the rebound process involves an electron shift from the radical center to the heme that gains one electron (either in the a_{2u} or the π^* orbitals of the heme) in both the HS and LS manifolds. However, spin conservation in the HS manifold requires shifting the electron to the high-lying $d_{z^2}(\sigma^*)$ orbital, which has Fe−O and Fe−S antibonding character (consult Figure 4). This is the reason the HS rebound step has a barrier while the LS rebound is barrier free.

A recent valence-bond model[36] provides a systematic way of predicting trends in the barrier height. Thus, the HS rebound barrier, in a series of related radicals, depends on a combination of two factors: the ionization potential of the radical that has to lose an electron to the heme and the excitation energy of the heme ($\pi^* \Rightarrow d_{z^2}(\sigma^*)$). Both factors were analyzed and shown to be important.[36] The first factor predicts that as the radical center will become a better electron donor (lower ionization potential), the rebound barrier should decrease. Figure 29 shows the series of Newcomb probes organized according to increasing donor ability of the radical center. It is seen that for the poorest donors (top) the amount of rearrangement reaches 20−25%, and as the donor strength improves, the amount of rearrangement decreases. For the best donor radical (at the bottom), nascent from the *trans*-2-phenyl isopropyl cyclopropane probe, the amount of rearranged product was barely detectable.

The mechanism of C−H hydroxylation in the substrate *trans*-2-phenyl isopropyl cyclopropane was studied by Kumar et al.[96] using DFT(B3LYP); the results are summarized in Figure 30. The TSR scenario is apparent here too. However, now both LS and HS rebound processes proceed without a barrier. Thus, the prediction of the VB model[36] and theoretical calculations reproduce the experimental result that this substrate exhibits no detectable rearrangement.[196]

Theory predicts another result based on the TSR scenario. Thus, since the LS and HS bond-activation transition states have different geometries, the reac-

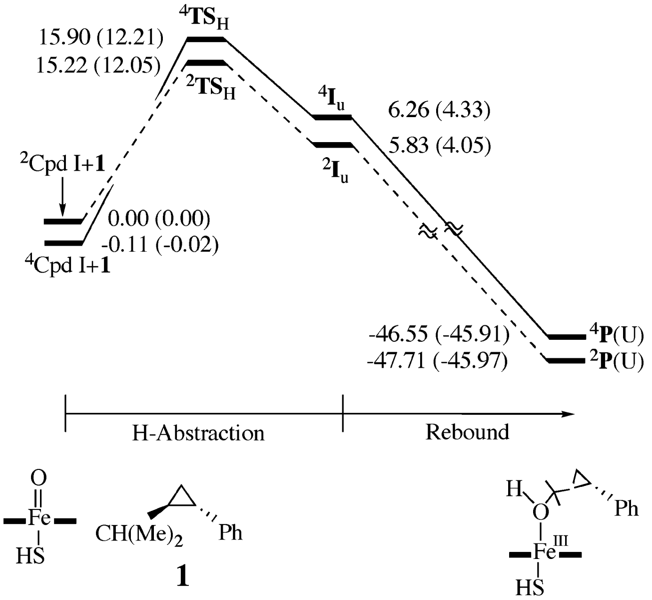

Figure 30. DFT(B3LYP/LACVP-DZ) results for C−H hydroxylation of *trans*-2-phenylisopropylcyclopropane; data in parentheses are LACV3P+*-6-311+G* values. Energy data (kcal mol^{-1}) include ZPE corrections. (Reprinted with permission from ref 96. Copyright 2004 American Chemical Society.)

tion should exhibit an intrinsic product isotope effect different from unity (PIE = KIE(***U***)/KIE(***R***) ≠ 1), namely, different isotopic sensitivity of the rearranged and unrearranged products.[92] Kumar et al.[96] calculated the PIEs for the *trans*-2-phenyl methyl cyclopropane probe and found, generally, PIE values >1, in the direction of the experimentally measured ones.[213] It was shown[96] that the magnitude of PIE is determined by the location of the HS and LS transition states along the hydrogen-transfer coordinate; a central TS gives a large KIE, while an 'early' or 'late' one leads to smaller KIEs.[214] As argued, these considerations should apply to intrinsic PIEs determined from intramolecular isotope effect measurements. Other factors which affect observed PIEs, e.g., the effect of competing phenyl hydroxylation, were analyzed[96,202] based on the kinetic scheme of Jones and co-workers for a mechanism that branches into two products via two enzyme (Cpd I)−substrate (ES) complexes.[215] The reader is advised to consult these and other sources for further details.

4.6.2. Reactivity of Ferric Hydroperoxide (Cpd 0) in P450 Oxidations

As already noted above, Newcomb et al.[196] invoke another oxidant species to explain the observed rearrangement during P450 hydroxylation. The primary candidate for this second oxidant species is usually Cpd 0.[195,196,213] Our many attempts to find low-energy pathways for C−H hydroxylation with Cpd 0 failed.[80] Two groups[80,105] used B3LYP to study double-bond epoxidation since this process is considered to be a marker reaction of this oxidant.[197,201] Another B3LYP study was devoted to sulfoxidation by Cpd 0.[111] The results of these studies are briefly summarized in Figure 31, which compares the barriers for oxidation by Cpd 0 with those by Cpd I. The former is seen to be very large. Clearly, Cpd 0 is a sluggish oxidant, even in the presence of a potent acid catalyst. Considering the relative barriers for Cpd 0 and Cpd I, it is apparent that Cpd 0 cannot compete in the presence of Cpd I. Therefore, any scenario that invokes a competition between the two oxidants merits some careful rethinking. A recent experimental study of C−H hydroxylation[159] shows that even in cases of activated C−H bonds the oxidizing reagent responsible for the KIEs in two different P450 enzymes is Cpd I and not Cpd 0. The latter study supports the conclusions based on TSR. Indeed, the TSR scenario seems to account for many of the tantalizing features of C−H hydroxylation.

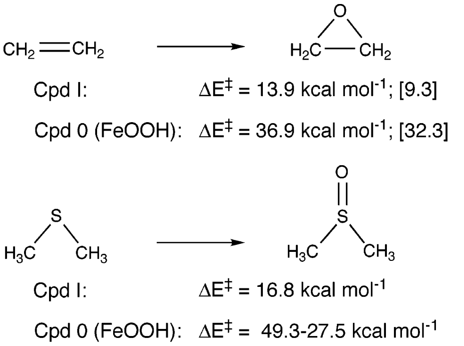

Figure 31. Summary of relative barriers (kcal mol^{-1}) for the epoxidation of ethene and sulfoxidation of dimethyl sulfide by Cpd I and Cpd 0. Data in brackets are from ref 105. The data out of brackets are from ref 80 for epoxidation and ref 111 for sulfoxidation. The lowest barriers are shown in each case.

4.7. Predictive Pattern of C−H Hydroxylation Barriers Emerges from Theory

Mayer[216,217] demonstrated that the barriers for hydrogen abstraction by metal oxo complexes correlate linearly with the bond dissociation energies of the C−H bond, which is broken, and the MO−H bond, which is formed. He showed that these Bell−Evans−Polanyi-type correlations are universal and predictive. Furthermore, such correlations can be derived from fundamental models of barrier formation,[218] which make them also physically meaningful. The first attempt to achieve such order in the area of P450 reactivity was made by Korzekwa et al.,[219] who used semiempirical AM1 calculations to correlate the barriers for P450 hydroxylation with a variety of factors, including the energy of the bond-activation step. Subsequently, Park and Harris[220] demonstrated that the patterns of metabolism of substrates, with multiple regiochemical sites, by the human enzyme P450$_{2E1}$ can often be predicted by considering the energies of the hydrogen-abstraction process. Obviously, the ability to predict P450 barriers is very important, but one must establish first that such a correlation is indeed obeyed in P450 hydroxylation across the board.

To this end, de Visser et al.[98] used B3LYP calculations with two different basis sets (LACVP-DZ and LACV3P+*/6-311++G**) and studied the barriers for C−H hydroxylation of 10 different substrates, ranging from methane through camphor to toluene and phenylethane. Table 2 (see section 4.5) shows the computed barriers. An important factor is the reduc-

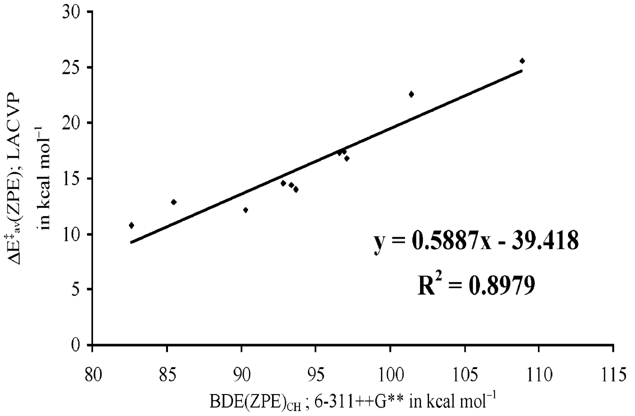

Figure 32. Correlation between hydrogen-abstraction barrier heights of the substrates given in Table 2 and C−H bond dissociation energies (BDE_{CH}) computed at the B3LYP/6-311++G** level (consistent with experimental values). The average values of the HS and LS barriers were used in the correlation. (Reprinted with permission from ref 98. Copyright 2004 American Chemical Society.)

tion of the barrier height by the zero-point energy (ZPE) correction due to the loss of a C−H vibration in the transition state. In the gas phase the free-energy barriers are considerably higher than the ZPE-corrected energy or enthalpy barriers due to the entropic costs associated with the loss of translational and rotational degrees of freedom upon association and some structural stiffening of the heme. These factors are not important in the enzyme that binds the substrate by virtue of the entropy gain caused by the expulsion of water molecules from the pocket, as the substrate enters the pocket. Thus, for all practical purposes the important factors for reasoning about enzymatic reactivity are the $\Delta E(\mathrm{ZPE})^{\ddagger}$ and/or $\Delta H^{\ddagger}$ values in Table 2.

A systematic error in the reported B3LYP/LACVP-DZ barriers exists since they are larger than the B3LYP/LACV3P+* values, on average by 1.2 kcal mol^{-1}. While this may change further with geometry optimization and a still better basis set, it is not likely to change much more; the set of barriers in Table 2 may be considered internally consistent and reasonably reliable. Since the radical products of the hydrogen abstraction have widely different delocalization properties (e.g., allyl and benzyl radical vis-à-vis simple alkyl radicals), an appropriate criterion would be the in-situ C−H bond strengths, which are bond dissociation energies (BDE_{CH}) corrected for the radical reorganization energies. Using these C−H bond strengths led to very good correlations with the $\Delta E(\mathrm{ZPE})^{\ddagger}$ barriers, with correlation coefficients of $R^2 = 0.98-0.99$.[98] Furthermore, the correlation between the LACVP-DZ and LACV3P+*/6-311++G** barriers is also good ($R^2 = 0.975$). Thus, the correlation is genuinely good and can serve as a tool for making predictions.

For practical purposes, however, one needs a correlation that can be used across the board by relying only on experimental BDE_{CH} data. Figure 32 is such a plot of the computed averaged high-spin and low-spin $\Delta E(\mathrm{ZPE})^{\ddagger}$ barriers against the experimentally matched $BDE(ZPE)_{CH}$ values. The trend shows clearly an increase of barrier height with increased C−H bond energy. The regression in Figure 32 can be used to estimate barriers within 1−2 kcal mol^{-1}.

An illustration of the utility of the correlation in Figure 32 is the application to camphor hydroxylation by $P450_{cam}$. The low-spin $\Delta E(\mathrm{ZPE})^{\ddagger}$ barriers, from the gas-phase reactant complex, are 16.5 (LACVP) and 15.1 (LACV3P+*) kcal mol^{-1}, and the $\Delta H^{\ddagger}$ values are within 0.4−0.6 kcal mol^{-1}.[179] These values are quite close to the $\Delta E(\mathrm{ZPE})^{\ddagger}$ barriers computed by DFT-(B3LYP)/MM calculations.[84] The $BDE(ZPE)_{CH}$ value (6-311++G**) for camphor is 93.7 kcal mol^{-1}, close to an experimental estimate of 98 ± 4 kcal mol^{-1}.[185] Using the Mayer series,[216] with CrO_2Cl_2 as the oxidant, we find that cyclooctane with $BDE_{CH} = 95.7$ kcal mol^{-1} gives a $\Delta H^{\ddagger}$ value of 19.4 kcal mol^{-1}. Taking into account the BDE_{CH} differences and the fact that the calculated FeO−H bond energy is higher than the estimate[216] for CrO−H, by 5 kcal mol^{-1}, a lower barrier would be expected for camphor hydroxylation by Cpd I. From the slope of the correlation in Figure 31, the barrier lowering should be 4.1 kcal mol^{-1} (6.5 kcal mol^{-1} if we use the $D_{\mathrm{FeO-H}}$ datum of Green et al.[185]), thereby resulting in "an experimentally scaled barrier" for camphor hydroxylation of 15.4 (14.0) kcal mol^{-1}. Using the porphyrin−Mn(V)−oxo data[221] in conjunction with the correlation in Figure 32 leads to another "experimentally scaled barrier" of 17.7 kcal mol^{-1} for camphor hydroxylation. Single-turnover kinetics data for camphor hydroxylation by $P450_{cam}$[222] yields an upper limit of the free-energy barrier as $\Delta G^{\ddagger} < 15$ kcal mol^{-1} ($k > 200\ \mathrm{s}^{-1}$). The computed DFT-based barriers (see above) are not too far from these values and thus support the validity of the correlation given in Figure 32.

4.8. Carbocation Intermediates during C−H Hydroxylation

During the study of the hydroxylation of 2-phenylisopropyl cyclopropane by Cpd I it was noticed[96] that in addition to the usual radical "intermediates" (the $\mathbf{I}_{\mathrm{U}}$ species in Figure 30) there exists a LS cationic species. Figure 33 shows the radical and cationic species. The spin and charge densities on the alkyl moiety (Alk) make it apparent that ${}^2\mathbf{I}_{\mathrm{u}}{}^{+}$ involves a largely cationic substrate coordinated to the iron−hydroxo anion, whereas both ${}^{4,2}\mathbf{I}_{\mathrm{u}}$ species involve a coordinated alkyl radical. As discussed by reference to Figure 30, the rebound process for the two radical species is barrierless. The cationic species behaves much the same and collapses to the corresponding ferric alcohol product in a barrier-free manner. No such species could be located for C−H hydroxylation of *trans*-methylphenyl cyclopropane.[95,96]

An outstanding feature of the cationic species in Figure 33 is the very long C---O distance in ${}^2\mathbf{I}_{\mathrm{U}}{}^{+}$, ca. 3.2 Å. One may therefore wonder whether a free cationic species is available during the reaction and if so whether it has sufficient lifetime to rearrange and lead to products typical of carbocations. The B3LYP calculations,[96] displayed in Figure 34, show that, among other possibilities, such a free cationic species could rearrange to the open form ($\mathbf{2}^{+}$) as well as to a new form ($\mathbf{3}^{+}$). To the best of our knowledge,

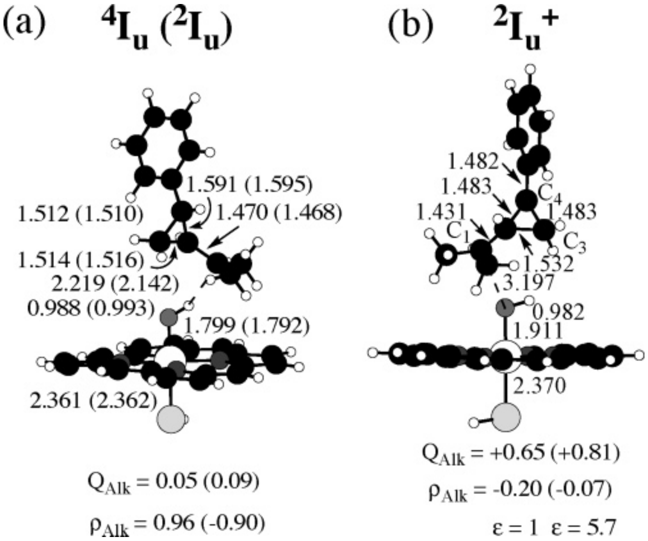

Figure 33. B3LYP/LACVP-DZ calculated structures (Por,-SH model) of (a) radical and (b) cationic species during C−H hydroxylation of isopropylphenylcyclopropane. The spin density (ρ) and charge (Q) on the alkyl moiety (Alk) are shown underneath the structures. The data in parentheses for the cation correspond to the values in a dielectric medium (with a dielectric constant $\epsilon = 5.7$). (Reprinted with permission from ref 96. Copyright 2004 American Chemical Society.)

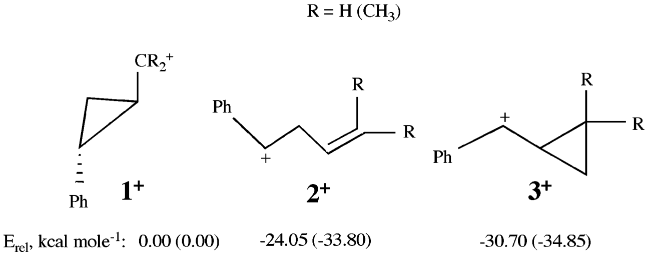

Figure 34. B3LYP/6-311+G* calculated isomers of cationic species and their relative energies (kcal mol^{-1}). (Reprinted with permission from ref 96. Copyright 2004 American Chemical Society.)

products derived from **3**$^+$ have not been reported for either *trans*-isopropyl phenylcyclopropane or *trans*-methyl phenylcyclopropane probes.[196] This puts a question mark on the possibility that the observed rearranged products for this family of probe substrates (Figure 29) originate from rearrangement of free carbocations. In addition, the example of $^2\mathbf{I}_U{}^+$ shows that coordinated carbocations undergo a barrier-free rebound, so that carbocationic rearrangement within the complex may not be competitive with the rebound. Nevertheless, the results do not rule out an in-protein scenario where the carbocationic moiety, which is weakly coordinated, will detach from the complex by coordination to protein residues or to a water molecule and therefore reveal carbocationic behavior.

4.8.1. Possible Origins of Dehydrogenase/Oxidase Activity during C−H Hydroxylation

The economy of dioxygen consumption by P450 constitutes a fundamental problem.[114] In its normal activity the enzyme catalyzes the "insertion" of an oxygen atom into substrates by utilizing two reduction equivalents (2e$^-$), 1 mol of O_2, and two proton equivalents; the other [O] equivalent is converted to water, eq 2. Occasionally, the O_2 consumption follows eq 3, where the enzyme converts all the dioxygen into water, thereby acting as an oxidase, but at the same time dehydrogenates the substrate[223,224] and functions as non-heme enzymes that catalyze fatty acids metabolism

$$O_2 + 2e^- + 2H^+ + HR_2C{-}CR'_2H \rightarrow HR_2C{-}CR'_2OH + H_2O \quad (2)$$

$$O_2 + 2e^- + 2H^+ + HR_2C{-}CR'_2H \rightarrow R_2C{=}CR'_2 + 2H_2O \quad (3)$$

A seminal study[225] of C−H hydroxylation of the anti-epileptic drug valproic acid showed that the dehydrogenase−oxidase activity and the normal monooxygenation function branch from the same oxidation mechanism that involves Cpd I. This and other studies[7,223,226−228] led to the conclusion that the mechanism involves an initial hydrogen abstraction from the substrate by Cpd I. Subsequently, the so formed radical may be partitioned between a few possible pathways, e.g., to form alcohol by rebound (see Figure 21 above). In the mixed oxidase−dehydrogenase route the radical loses one more hydrogen atom (possibly by sequential loss of electron and proton), thus producing olefin and water.

Since the mechanistic details are not clear-cut and the desaturation reaction is not very predictable,[224] theoretical calculations by Kumar et al.[97] were used to gain additional insight. The model alkane (Alk-H) chosen for the calculations is *trans*-2-phenyl-1-isopropylcyclopropane. Despite the fact that there are no clear experimental data that show oxidase/dehydrogenase reactivity for this substrate, it was selected because it leads to both radical and cationic species en route to rebound and because it is sterically encumbered to reveal possible insight about the mixed oxidase/dehydrogenase function. These features allowed the testing of the putative mechanistic scenarios of the dehydrogenase/oxidase reaction. Figure 35a shows the radical, $^2\mathbf{I}_U$(rad), and cation, $^2\mathbf{I}_U$(cat). The conformation of $^2\mathbf{I}_U$(cat) is different from the one shown in Figure 33b, the latter being prepared for rebound, while here in $^2\mathbf{I}_U$(cat) the methyl groups of the isopropyl moiety are close to the iron−hydroxo anion. As shown by the arrows in Figure 35a, $^2\mathbf{I}_U$(rad) undergoes a barrier-free rebound (as in Figure 30) while $^2\mathbf{I}_U$(cat) spontaneously loses a proton from the $(CH_3)_2C{-}H^+$ moiety to the ferric−hydroxo anion to form the corresponding alkene and the ferric−water complex. In fact, the ^2I_U(cat) species is on the downhill slope en route to alkene product complex. Frequency analysis of $^2\mathbf{I}_U$(cat) exhibits a single negative eigenmode that corresponds to the second hydrogen transfer to the heme. It is part of the same cation manifold that branches out to give alcohol by rebound (Figure 33b) and to the alkene by additional proton transfer (Figure 35a). *Thus, theory reveals that the dehydrogenase−oxidase activity is not associated with radicals of the substrates but rather with the corresponding carbocations*. This is indeed one of the possibilities postulated in the

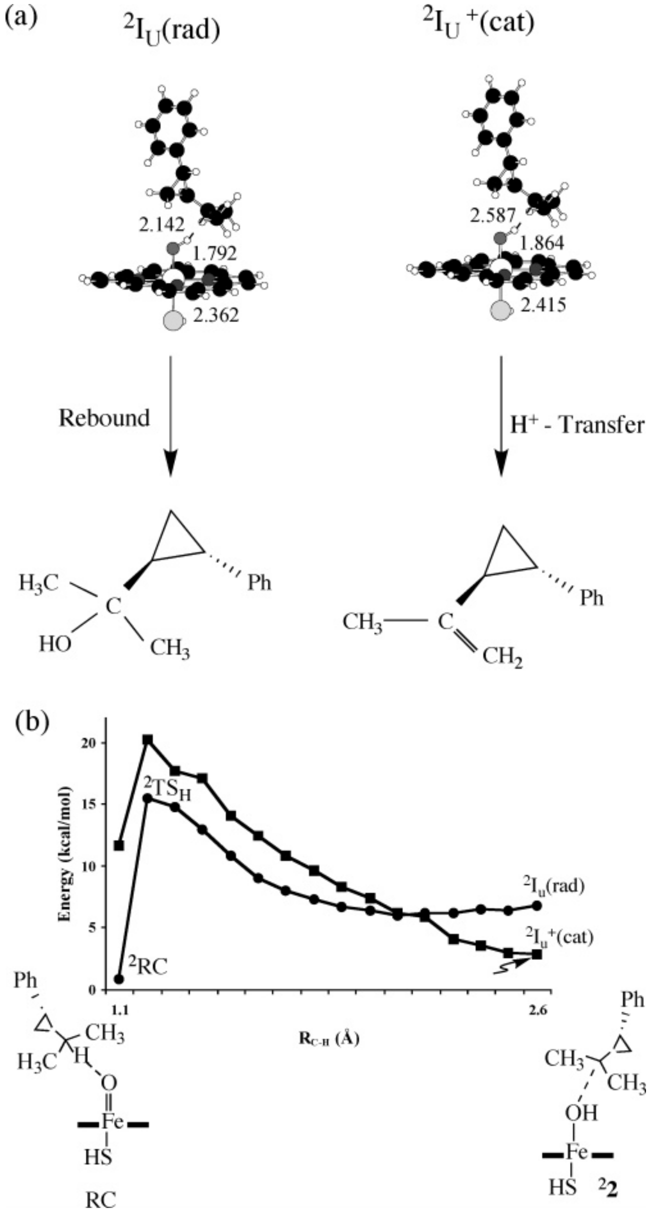

Figure 35. B3LYP/LACVP-DZ calculated isopropylphenylcyclopropyl radical (^2I_U(rad)) and cation (^2I_U(cat)) species after hydrogen abstraction. (a) The spontaneous processes of the two species are indicated by the arrows leading to the respective products. (b) The surface crossing of the radical and cationic manifolds along the C−H abstraction coordinate. Data taken from ref 97.

experimental literature.[7,224,228] Furthermore, as shown in Figure 35b, according to the calculations,[97] electron transfer from the alkyl radical to the iron−hydroxo complex occurs by surface crossing between the radical and cationic manifolds during the initial C−H abstraction phase, wherefrom the reaction proceeds further to the alkene.

What is the reason for the oxidase−dehydrogenase mode of $^2\mathbf{I}_U$(cat)? Inspection of the geometry of the species in Figure 35 shows that the C---O distance is 2.6 Å compared with 2.1 Å for the corresponding radical. The conformer of $^2\mathbf{I}_U$(cat), $^2\mathbf{I}_U{}^+$ in Figure 35b, exhibits an even much longer distance in the rebound-prepared orientation (3.2 Å). The reason for this long C---O distance is rooted in the steric bulk and the charges of two moieties of ^2I_U(cat). Thus, on one hand, the steric bulk of the isopropyl prevents the close approach necessary for instantaneous C---O bond making. This is further augmented by the charge effect: In the cationic species, $^2\mathbf{I}_U$(cat), the iron−hydroxo is negatively charged and maintains O^----H^+ interaction with the close-by positively charged hydrogen ends of the CH_3 groups of the Alk cation moiety; this facilitates proton abstraction. Thus, the electrosteric factor causes a spontaneous proton transfer from the radical to the iron−hydroxo complex and results in the oxidase−dehydrogenase activity.

The electrosteric factor links the theoretically studied process to the "pure" oxidase activity of P450, which converts all the O_2 to water, by using an extra mole of the reductase that provides $4e^-$ in the course of the reaction (i.e., $O_2 + 4e^- + 4H^+ \rightarrow 2H_2O$). As has been shown by experiments,[114,229] the "decoupling" of oxygen consumption from substrate oxidation occurs when Cpd I accepts two electrons from the reductase. Mueller et al.[114] further demonstrated that whenever the protein pocket is encumbered, such as to prevent approach of the substrate C−H bond to the FeO moiety of Cpd I, there are increased "decoupling" and heightened "pure" oxidase activities. The theoretical study[97] shows similarly that whenever the substrate is sterically encumbered, so that the C---O approach is hindered, the cationic intermediate will lead to a mixed oxidase−dehydrogenase reaction. Thus, the oxidase−dehydrogenase function requires substrates that combine steric inhibition of rebound and stable carbocationic complexes. It is further reasonable to speculate that in the protein environment release of the carbocation, away from the iron hydroxo anion, may compete with dehydrogenation. In such an event the carbocation will either get hydroxylated (e.g., by rebound from a long C---O distance [Figure 33b] or simply by water) or mediate "pure" oxidase activity by accepting electrons from the reductase while restoring the substrate by hydrogen abstraction.

4.9. DFT Studies of Alkene Epoxidation: TSR and MSR Scenarios

Alkene epoxidation by P450 and other Cpd I reagents has many of the puzzling mechanistic features that have been discussed above for C−H hydroxylation.[5,230] Scheme 2 summarizes the type of products produced by the reaction of Cpd I with an alkene. Several experimental observations, such as occasional cis/trans isomerization,[231] sensitivity of the reaction to the donor capability of the olefin,[232] production of aldehydes,[231,233] and formation of heme-alkylated products ("suicidal complexes"),[7,9] indicate that the mechanism involves intermediates which are very likely of different nature. Indeed, the proposed mechanistic schemes[5,230] suggest the incursion of radicals, cations, and radical cationic intermediates. Theory was used to shed light on these mechanistic puzzles.

Figure 36 shows the calculated B3LYP/LACVP results[106−108,205,234] for ethene epoxidation. The reaction profile, much like C−H hydroxylation, follows a nonsynchronous TSR with competing HS and LS

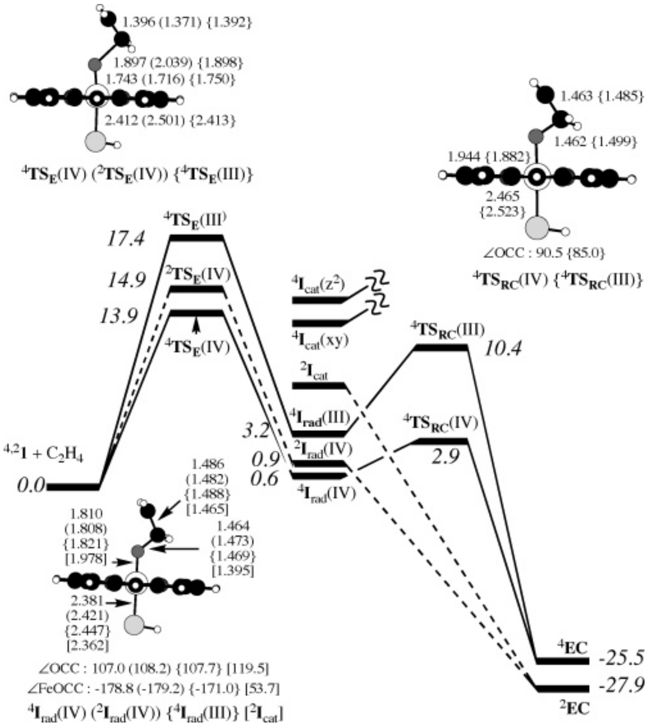

Figure 36. B3LYP/LACVP calculated energy profiles for the reaction of Cpd I (Por,SH model) with ethene. **TS**$_{RC}$ **TS**$_{E}$, **TS**$_{RC}$, and **EC** denote the epoxidation transition state, the ring-closure transition state, and the epoxide complex, respectively. All intermediate species are labeled with the letter **I**. Relative energies are in kcal mol^{-1}. (Reprinted with permission from ref 205. Copyright 2004 Elsevier Inc.)

pathways. An initial C═C bond-activation step proceeds via three nonsynchronous transition states, ^{4,2}**TS**$_E$, to the iron alkoxy radical species (^{4,2}**I**$_{rad}$). The oxidation state of the iron is indicated in these species by the Roman numeral, i.e., **I**$_{rad}$(III) stands for the Por$\bullet^{+}$Fe^{III}OCH$_2$CH$_2\bullet$ situation, and **I**$_{rad}$ (IV) for PorFe^{IV}-OCH$_2$CH$_2\bullet$ (consult the electronic structures in Figure 38). In addition, there are cationic situations, I$_{cat}$, that are generated by electron transfer from the carbon radical moiety into the heme and will be specified later (consult Figure 38). As indicated by the profile lines, some of these intermediates undergo ring closure and generate the ferric−epoxide product complex (^{4,2}**EC**). In this process the HS species are real intermediates with genuine transition states for ring closure (^{4}**TS**$_{RC}$), while the LS species collapse in a barrier-free manner to the corresponding epoxide complex, ^{2}**EC**. *Thus, much as in C−H hydroxylation, here too the HS mechanism is stepwise while the LS one is effectively concerted.* A synchronous concerted oxygen-transfer mechanism was ruled out since it was shown to proceed via a higher lying second-order saddle point (see Figure 20) that collapses to the nonsynchronous structures, ^{4,2}**TS**$_E$.[108] The epoxida-

Scheme 2. Epoxide and Side Products in the Reaction of Cpd I with Alkenes (Reprinted with permission from ref 205. Copyright 2004 Elsevier Inc.)

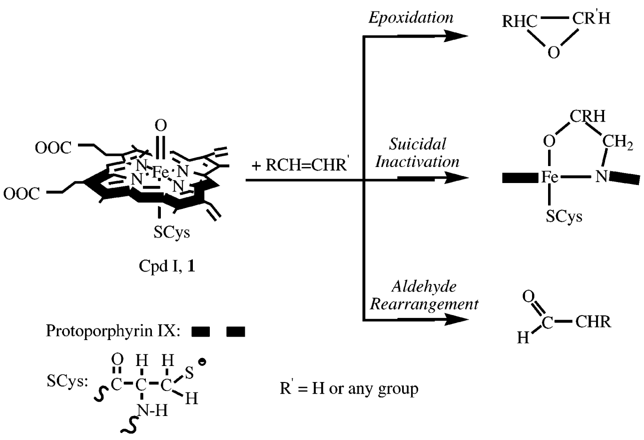

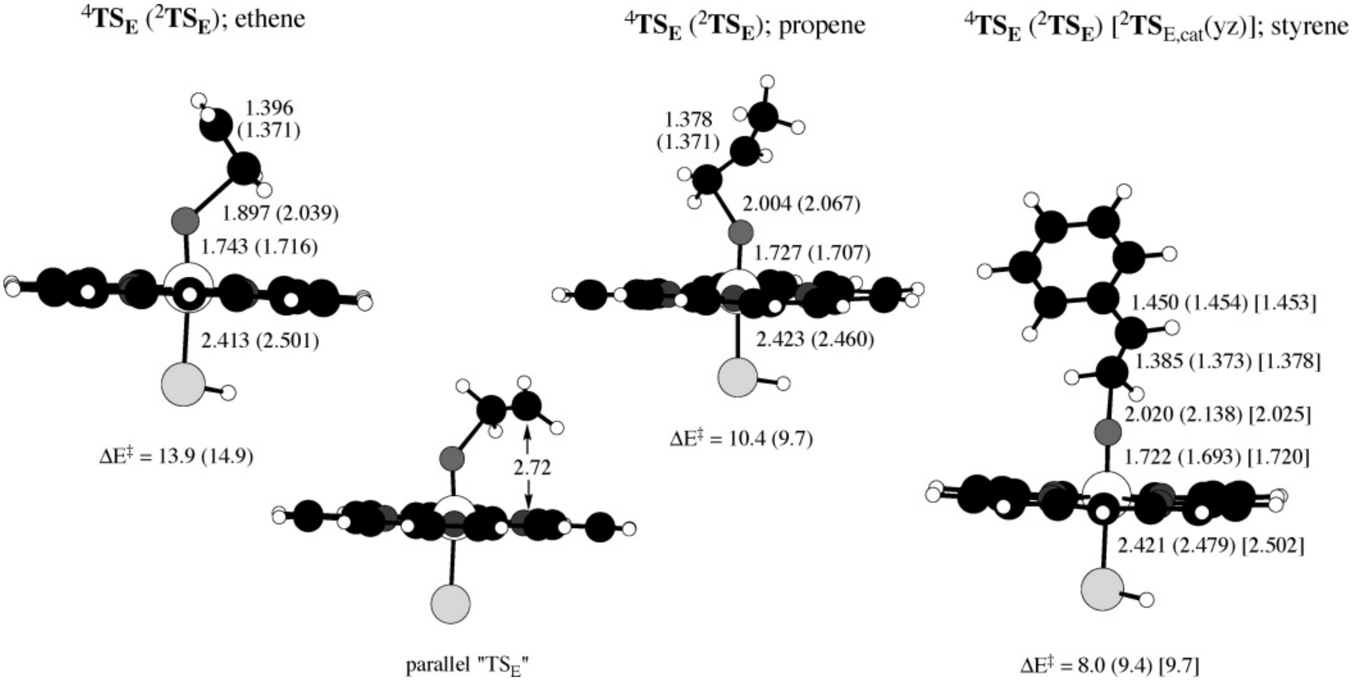

Figure 37. B3LYP/LACVP-DZ calculated structures and barriers for the epoxidation of three alkenes by Cpd I (Por,SH model). The last structure, parallel "**TS**$_E$", was generated, from the ^{2}**TS**$_E$ species for ethene epoxidation, by 90° rotation about the C−O bond.

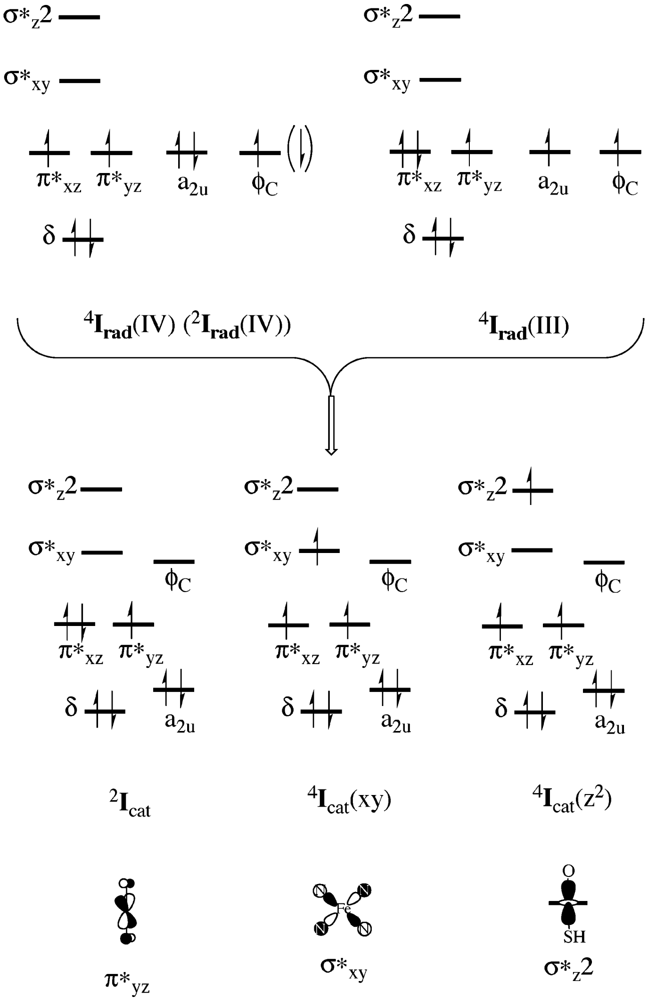

Figure 38. Orbital diagrams showing the formation of the intermediate cationic species ($^{2,4}\mathbf{I}_{\mathrm{cat}}$) from the radicals, $^{2,4}\mathbf{I}_{\mathrm{rad}}$(IV) and $^4\mathbf{I}_{\mathrm{rad}}$(III). The symbols in parentheses for the HS cationic states specify the orbital that accepts the electron from the ϕ_C orbital of the radical center. These orbitals are depicted underneath the orbital diagrams. (Reprinted with permission from ref 205. Copyright 2004 Elsevier Inc.)

tion mechanisms for propene,[93,94] styrene,[205,234] and cyclohexene[179] were found to be virtually identical to the one displayed in Figure 36 for ethene, except for the bond-activation barriers that are some 4−6 kcal mol^{-1} lower (other features are discussed below). Table 3 lists these barriers, and it is apparent that they decrease as the alkene becomes a better electron donor, in accord with experimental trends.[3,5,9,224,232]

Figure 37 compares the optimized geometries of the lowest lying bond-activation transition states in the epoxidation studies of ethene,[106−108,205] propene,[93,94] and styrene.[234] Consistent with the decreasing bond-activation barriers (Table 3), the transition states for styrene are somewhat earlier than those for ethene (compare, e.g., the C−O and C=C distances). Interestingly, in all the structures the alkene moiety assumes an "upright" orientation with respect to the plane of the porphyrin ring, presumably to avoid repulsion with the porphyrin ring. Groves et al.[232,235] suggested a transition state with a synchronous parallel orientation to account for the preferred reactivity of cis over trans isomers (cis is preferred in the synchronous parallel conformation since the two substituents of the cis isomer can be oriented away from the porphyrin). An alternative structure, the parallel "$\mathbf{TS}_{\mathrm{E}}$" species in Figure 37, was generated[37] by rotation of the FeOCC dihedral angle of the nonsynchronous $\mathbf{TS}_{\mathrm{E}}$ structure for ethene epoxidation. This nonsynchronous−parallel transition structure can also account for the relative reactivity of cis and trans isomers. The structures of the actual $\mathbf{TS}_{\mathrm{E}}$ species in the enzyme appear in these two generic conformations according to preliminary DFT(B3LYP)/MM calculations.[179]

4.9.1. Intermediate States and Multistate Reactivity (MSR) in Alkene Epoxidation

After the formation of the radical intermediates ring closure will lead to the formation of epoxide products. As already stated (see Figure 36), ring closure on the LS manifold is barrierless while the HS manifold exhibits significant barriers. As such, the HS intermediates will scramble the initial stereochemistry of the alkene to yield a mixture of cis and trans epoxides, whereas the intermediates with larger ring-closure barriers will participate in other processes as well.

To facilitate the discussion of these processes, Figure 38 shows orbital diagrams of the intermediate situations and the generation of the cationic species from the radical intermediates by electron transfers to the heme. The high-spin cationic situations are indicated with a parenthetical label, which specifies the orbital that accepts an electron from the radical center, e.g., $^4\mathbf{I}_{\mathrm{cat}}(xy)$ corresponds to the quartet state of the cation in which the accepting orbital is the σ_{xy}^* orbital, etc. Similarly, the LS cationic species is indicated as $^2\mathbf{I}_{\mathrm{cat}}(yz)$ to specify the singly occupied iron d orbital. This group of states is responsible for multistate reactivity (MSR) during alkene epoxidation.

Figure 39 summarizes the MSR scheme obtained during the study of ethene[205] and may serve as a model for similar simple alkenes. The figure reveals

Table 3. Barriers $\Delta E^{\ddagger}$ and Barriers with Zero-Point Energy Correction $\Delta E(ZPE)^{\ddagger}$ for Epoxidation of Alkenes by Cpd I[a]

substrate	spin state[b]	$\Delta E^{\ddagger}$	$\Delta E(ZPE)^{\ddagger}$	ref
ethene	LS(HS)	14.8 (13.9)		106
propene	LS(HS)	10.4 (9.7)	10.6 (10.3)	94
cyclohexene	LS(HS)	(11.9)	(12.1)	179
styrene	LS(HS)[cat][c]	9.4 (8.0)[9.7][c]	9.17 (8.5)[9.6]	234

[a] In kcal mol^{-1}. [b] Out of parentheses for the low-spin (LS) process; in parentheses for the high-spin (HS) process. [c] In square brackets: barrier for the LS cationic transition state, $^2\mathrm{TS}_{\mathrm{E}}(\mathrm{cat}, yz)$, leading to the ferric cationic intermediate (with one electron in the d_{yz} orbital, see Figure 38).

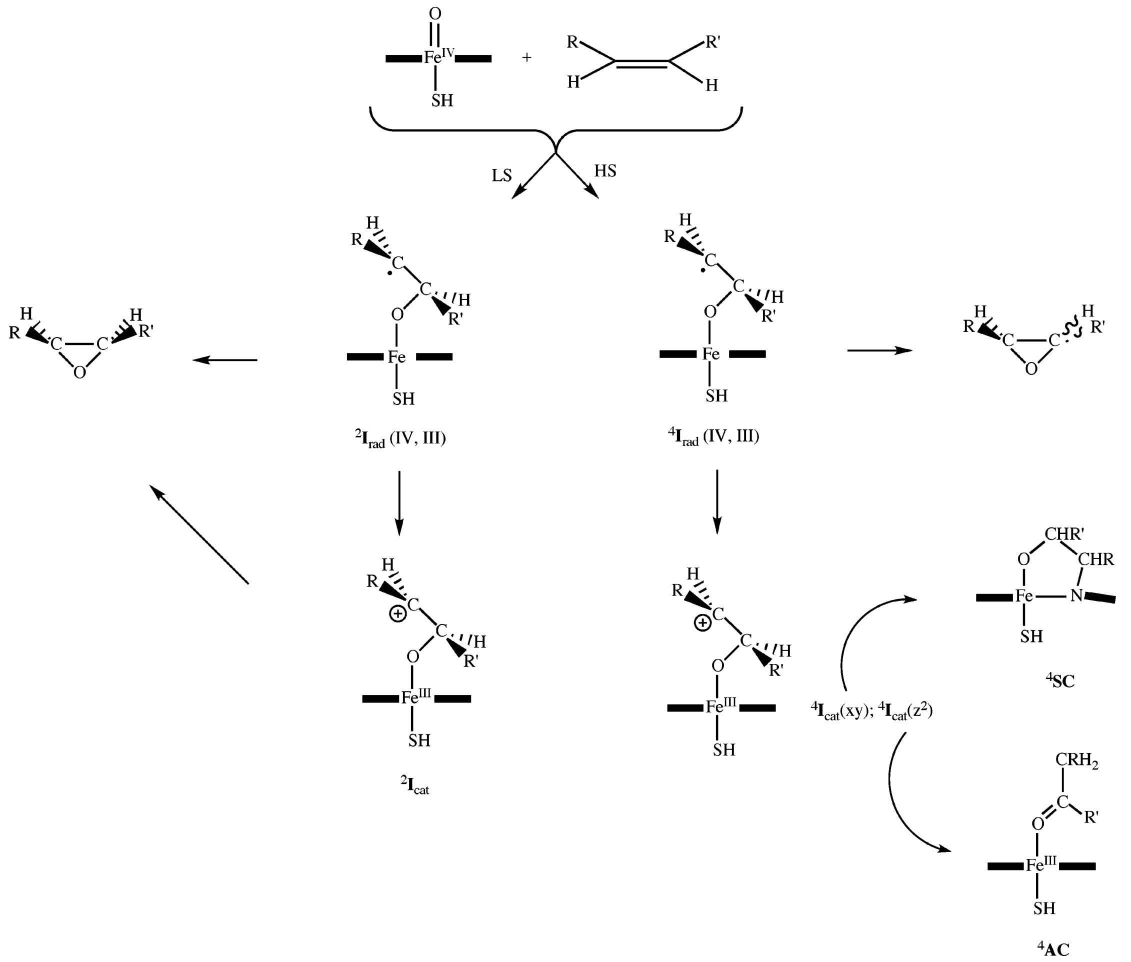

Figure 39. Multistate reactivity (MSR) scheme for epoxidation of simple alkenes by Cpd I. The states that generate the various products are specified. (Reprinted with permission from ref 205. Copyright 2004 Elsevier Inc.)

a multistate scenario in which the different products are generated *in state- and spin-specific manners*. All the low-spin doublet-state processes are effectively concerted epoxide-producing pathways. By contrast, all the high-spin quartet processes are stepwise and generate either an epoxide mixture that does not conserve the isomeric identity of the alkene (cis or trans) or/and byproducts such as suicidal complexes and aldehydes. The product/state inventory is as follows:

The $^4\mathbf{I}_{rad}$(IV) intermediate has a barrier for ring closure, ca. 2.3 kcal mol^{-1}, which is much lower than that for the $^4\mathbf{I}_{rad}$(III) intermediate, 7.2 kcal mol^{-1}.[106,107,205] At the same time, the C−C and C−O rotational barriers in the HS intermediates ($^4\mathbf{I}_{rad}$(IV), $^4\mathbf{I}_{rad}$(III)) are 1.5 kcal mol^{-1} or less.[106,107] Therefore, both HS intermediates lead to mixtures of cis and trans epoxides (e.g., starting from cis or trans 1,2-dideuterio ethylene or 2-butenes).

Because of its high ring-closure barrier, if the $^4\mathbf{I}_{rad}$(III) intermediate can be populated, before collapse to the lowest intermediate, it will participate also in formation of the "suicidal complex" (**SC**) and aldehyde complex (**AC**). As shown in Figure 39, this arises by the crossover of the $^4\mathbf{I}_{cat}(xy)$ and $^4\mathbf{I}_{cat}(z^2)$ states.[107,205]

Population of the σ^*_{xy} orbital in $^4\mathbf{I}_{cat}(xy)$ causes two effects: since this orbital has antibonding Fe−N interactions (Figure 38), the iron−nitrogen bonding in the porphyrin is weakened and at the same time the nitrogens become more negative and susceptible to attack by the cationic terminal carbon atom. Figure 40a exemplifies the formation of the "suicidal" complex by crossing of the radical and $^4\mathbf{I}_{cat}(xy)$ states; the latter state descends smoothly to the "suicidal complex".

In the $^4\mathbf{I}_{cat}(z^2)$ state population of the $\sigma^*_{z^2}$ orbital (Figure 38) lengthens the Fe−O bond and the organic moiety becomes polarized in the sense "$^-OCH_2CH_2^+$"; the negatively charged oxygen then anchimerically assists the 1,2-hydride shift to the carbocationic center and creates the aldehyde complex. Due to this electronic structure the $^4\mathbf{I}_{cat}(z^2)$ state descends smoothly to the aldehyde complex,[205] as shown in Figure 40b.

Many of the features summarized in Figure 39 also occur in the reaction of Cpd I with styrene, but there are also obvious differences since styrene can stabilize carbocations much better than ethene or simple alkenes. Thus, the LS pathways proceed to epoxide in an effectively concerted manner, while the HS path proceeds in a stepwise manner via the radical intermediate, $^4\mathbf{I}_{rad}$(IV). Other HS species behave as above; the $^4\mathbf{I}_{cat}(xy)$ state descends smoothly to yield the suicidal complex, while the $^4\mathbf{I}_{cat}(z^2)$ state proceeds to the aldehyde complex. However, much of the epoxidation chemistry of styrene was found[234] to be associated with the cationic states. Figure 41 shows the

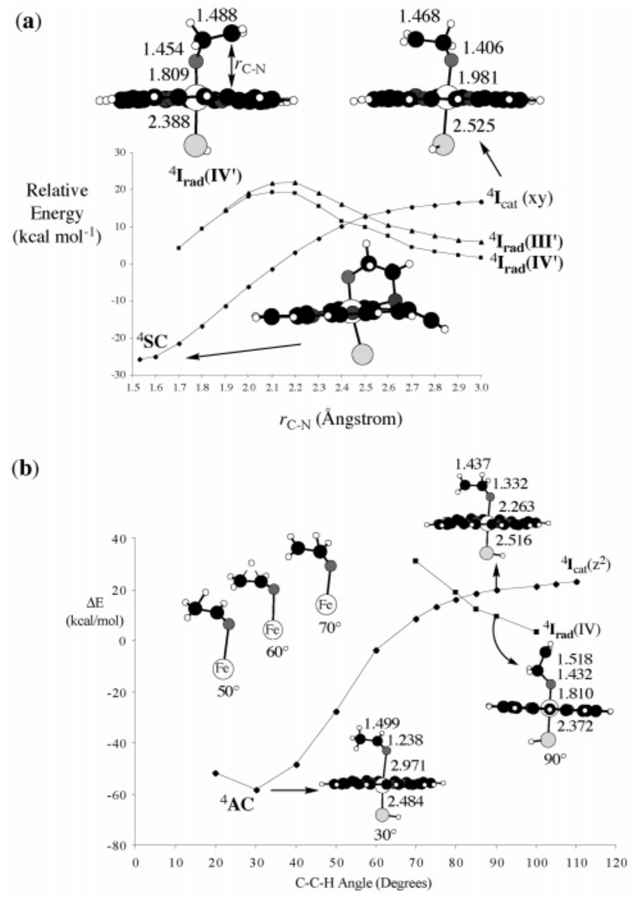

Figure 40. B3LYP/LACVP-DZ energy profiles for the formation of (a) the suicidal complex ^{2}**SC** and (b) the aldehyde complex, ^{4}**AC**, during epoxidation of ethene by Cpd I (Por,SH model). (Reprinted with permission from ref 205. Copyright 2004 Elsevier Inc.)

relative energies of the three bond-activation transition states in different environments. It is seen that in addition to the two radical species, ^{2,4}**TS**$_{E,rad}$, there is a third species, labeled as ^{2}**TS**$_{E,cat}$(yz), which leads to the intermediate cationic species, ^{2}**I**$_{cat}$(yz). In the case of ethene epoxidation this state is high lying, but for styrene it is very close to the radical states. Furthermore, external perturbations, such as a dielectric medium and NH---S hydrogen bonds to the thiolate, stabilize the cationic species, ^{2}**TS**$_{E,cat}$(yz), which then becomes the lowest state. This means that the effectively concerted LS pathways of cationic and radical nature will dominate the epoxidation of styrene.

Nevertheless, since the HS radical intermediates, ^{4}**I**$_{rad}$(IV) and ^{4}**I**$_{rad}$(III), lie considerably below the bond-activation transition states (by ca. 17−14 kcal mol^{-1}), they might be populated too and will lead to some scrambling and side products, due to crossing with the ^{4}**I**$_{cat}$(xy) and ^{4}**I**$_{cat}$(z^2) states. The changes with respect to ethene epoxidation are as follows: (a) ring-closure barriers are now smaller than the C−C rotational barrier, (b) the mechanism of aldehyde formation from the ^{4}**I**$_{cat}$(z^2) state involves initial protonation of a nitrogen atom in the porphyrin, by the CH_2 group, in the $FeOCH_2CHPh$ moiety, followed by back proton transfer from the porphyrin to generate the phenylacetaldehyde. The latter process is shown in Figure 42. It is seen that the proton abstraction by the porphyrin occurs in a barrier-free manner in the ^{4}**I**$_{cat}$(z^2) state and leads to the protonated porphyrin intermediate, ^{4}**I**$_{PorH}$, that rearranges with almost no barrier to the 1-hydroxo styrene enol complex (^{4}**E$_n$C**) or via a considerable barrier to the aldehyde complex (^{4}**AC**). Thus, the aldehyde will most probably form through a subsequent rearrangement of the enol. This proton-shuttle mechanism occurs also in benzene hydroxylation, as discussed in the next subsection.

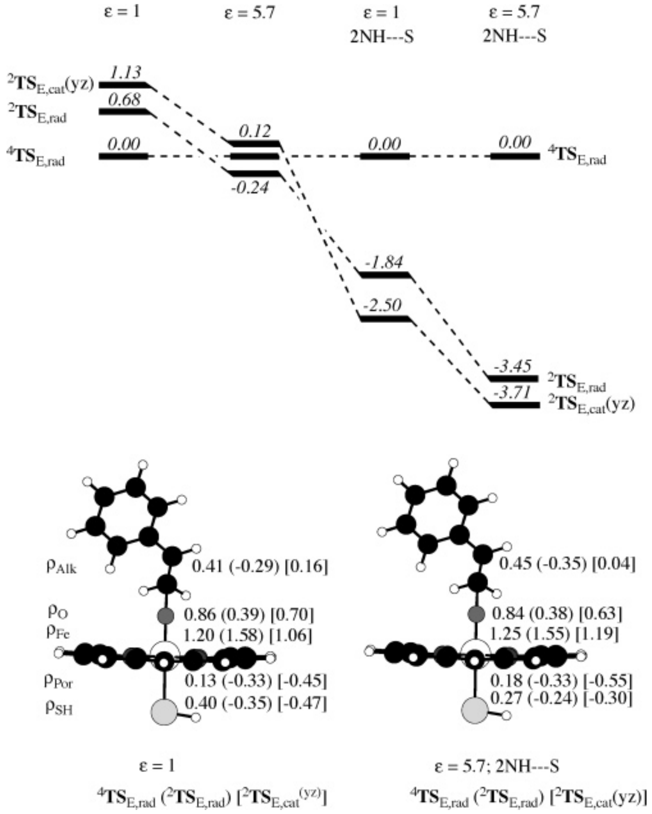

Figure 41. Relative B3LYP/LACVP-DZ energies (kcal mol^{-1}) and structures of three low-lying transition states for styrene epoxidation by CpdI (Por,SH model) under different conditions; ϵ is a dielectric constant, and 2NH---S refers to two hydrogen bonds to the thiolate ligand (H bonding is simulated as in Figure 14a). The numbers near the structures are spin densities (ρ).

In summary, the mechanism of alkene epoxidation is rich in MSR with state- and spin-specific reactions. Compared with similar experimentally based schemes,[3,5,7,9,16,230] theory has revealed additional spin-state specificities. What is missing at the time of writing of this review is a QM/MM study of epoxidation, which might define the role of the protein more precisely. Such a study is in progress.[179]

4.10. DFT Studies of Arene Hydroxylation by Cpd I

A long-standing dispute in P450 activation regards the mechanism of hydroxylation of arenes. This process is known to lead to phenol but generally also produces ketones and arene oxides as side products. The reaction features an NIH shift, i.e., an intramolecular hydrogen shift, which amounts to retention of the original hydrogen atom in the activated C−H

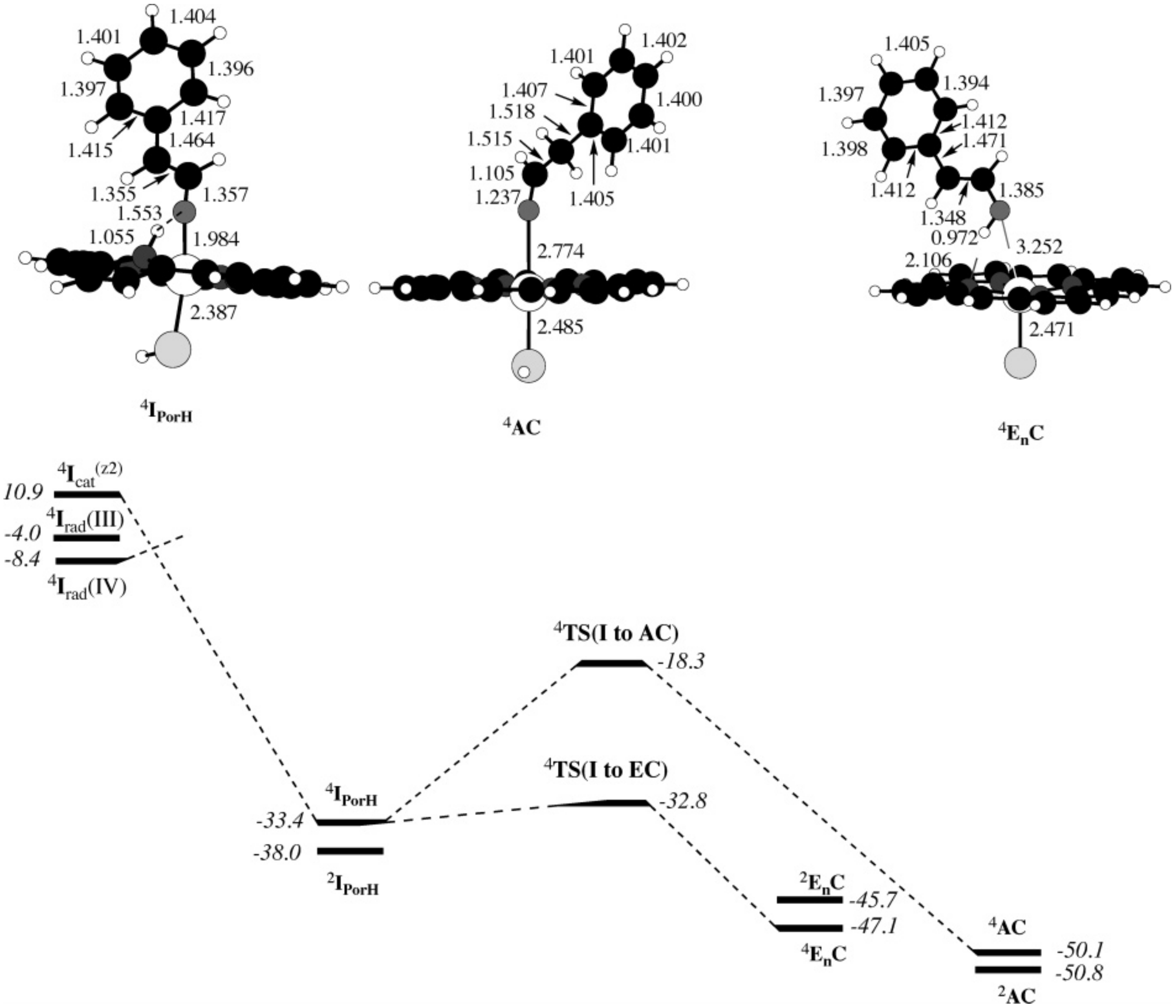

Figure 42. Relative B3LYP/LACVP-DZ energies (kcal mol^{-1}) with ZPE corrections, structures, and rearrangement pathways from the cationic state $^4\mathbf{I}_{cat}(z^2)$ toward the aldehyde complex (**AC**) and enol complex (**E$_n$C**) during styrene epoxidation by Cpd I (Por,SH model). The dashed line near $^4\mathbf{I}_{rad}$(IV) indicates that this state crosses the descending state.

bond in the products.[3,7] The reaction mechanism was addressed using DFT(B3LYP) calculations by de Visser and Shaik[109] and subsequently by Bathelt et al.[110]

Both studies conclude that the process involves initial electrophilic attack on the π-system of benzene and occurs preferentially from a LS state with a cationic character. Thus, de Visser and Shaik[109] ruled out a rebound mechanism like in C−H hydroxylation and benzene activation by an initial electron-transfer process. The most facile mechanism involves generation of Meisenheimer complexes by π-attack on the benzene. The computed reaction profile is shown in Figure 43 for the LS doublet pathways; the HS quartet pathways are much higher in energy and therefore not discussed. In agreement with experiment,[236,237] the LS reaction proceeds via π-attack of Cpd I on the benzene, leading to a radical-type intermediate ($^2\sigma$-C•) and a cationic-type intermediate ($^2\sigma$-C$^+$). The ordering and energy separation of the two LS reaction barriers depend on environmental factors, such as hydrogen bonding and a dielectric medium. In the presence of these external perturbations the cationic mechanism attains the lowest energy throughout.[109,110] Furthermore, Bathelt et al.,[110b] found the same LS mechanisms for an extended series of arenes and derived useful structure−reactivity correlations.

Starting from the intermediates ($^2\sigma$-C•; $^2\sigma$-C$^+$) there are barriers leading either to the ferric benzene oxide (^{2}**BO**) or to the protonated porphyrin intermediate $^2\mathbf{I}_{PorH}$. The latter is formed via a proton transfer from the ipso carbon to one of the nitrogen atoms of the porphyrin ring. This intermediate is formed since the nitrogens in the porphyrin are quite basic, and it is analogous to one discussed above for the conversion of styrene to phenylacetaldehyde (Figure 42). This $^2\mathbf{I}_{PorH}$ intermediate, in turn, reprotonates the oxo group to form phenol (^{2}**P**) and the ortho carbon to produce the ketone (^{2}**K**). Since the barriers (for reaching $^2\mathbf{TS}_{H-shuttle}$) separating $^2\mathbf{I}_{PorH}$ and the ketone and phenol products are well below the $^2\mathbf{TS}_{H\to N}$ transition states, it is expected that if the intermediate is not thermally equilibrated, it will generate both ketone and phenol.

The proton-shuttle mechanism in Figure 43 accounts for the NIH shift since the original hydrogen atom is retained in the process. Thus, the calculations show that an enzymatic pathway exists leading to direct formation of phenol and ketone without a

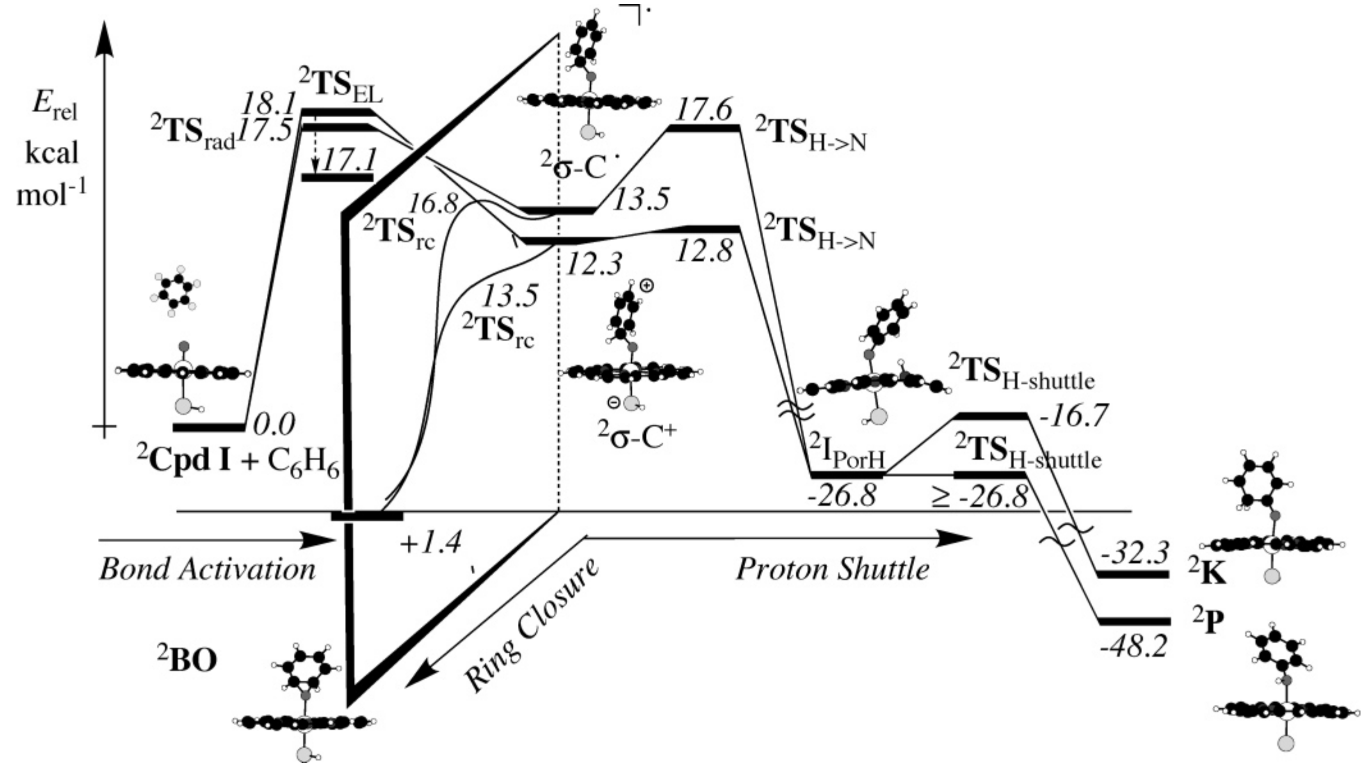

Figure 43. Relative DFT(B3LYP)/LACVP-DZ energies (kcal mol^{-1}) and LS mechanistic pathways for hydroxylation of benzene by Cpd I (Por,SH model). The bond-activation transition states are indicated as ^{2}**TS**$_{rad}$ and ^{2}**TS**$_{EL}$; the first leads to the radical complex, $^2\sigma$-C•, and the latter to the cationic complex, $^2\sigma$-C$^+$. These intermediates then either undergo ring closure to give benzene oxide (^{2}**BO**) or transfer a hydrogen species to the porphyrin to yield the intermediate ^{2}**I**$_{PorH}$, which then transfers the proton back either to the oxygen to give phenol (^{2}**P**) or to the ortho carbon to give ketone (^{2}**K**). The arrow leading from ^{2}**TS**$_{EL}$ down indicates its relative stabilization (relative to ^{2}**TS**$_{rad}$) by a dielectric medium ($\epsilon = 5.7$). The HS pathways are much higher in energy and not shown. (Reprinted with permission from ref 109. Copyright 2003 American Chemical Society.)

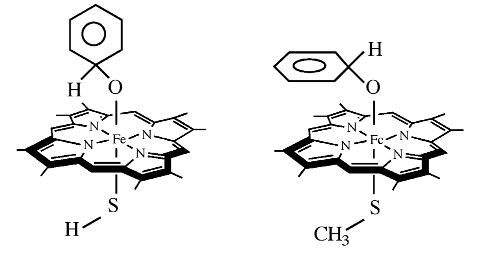

de Visser and Shaik

Bathelt et al

Figure 44. $^2\sigma$-C$^+$ complexes located during benzene hydroxylation by de Visser and Shaik[109] and Bathelt et al.[110]

benzene oxide intermediate. Bathelt et al. intially[110a] proposed an alternative mechanism in which the ketone (^{2}**K**) and phenol (^{2}**P**) are formed directly from the $^2\sigma$-C$^+$ intermediate by hydride shifts. The reason for the two different mechanisms is obvious from Figure 44, which depicts the $^2\sigma$-C$^+$ intermediates of the two studies. It is apparent that in the study of de Visser and Shaik[109] the phenyl plane is perpendicular to the porphyrin and the ipso C−H bond is in direct contact with one of the nitrogen atoms of the porphyrin, leading to instantaneous proton transfer and a reshuttle mechanism as described in Figure 43. By contrast, in the initial study of Bathelt et al.[110a] the phenyl ring is parallel to the porphyrin plane and the ipso C−H bond points away, thus prone to skeletal rearrangement by 1,2-hydride shifts. In the gas phase the barriers found by de Visser and Shaik[109] are smaller than those found initially by Bathelt et al.[110] In a subsequent study Bathelt et al.[110b] confirmed the proton-shuttle mechanism for the NIH shift and the results of the two groups completely converged. Indeed, in the protein pocket both conformations may exist and contribute to the NIH shift. Once again, this will have to wait for a QM/MM study.

4.11. Sulfoxidation of Dialkyl Sulfides by Cpd I

P450 enzymes are able to catalyze sulfoxidation reactions of dialkyl sulfides.[3,7,9] The results of a B3LYP study of sulfoxidation of dimethyl sulfide (DMS) by Sharma et al.[111] are displayed in Figure 45. Once again we see two energy profiles, which originate from the LS and HS spin states of Cpd I. However, here the HS mechanism has a considerably lower barrier and the reaction is synchronous.

Sharma et al. tentatively rationalized the dominance of the HS over LS sulfoxidation[111] in terms of the orbital interactions shown in Figure 46, which are characteristic of the different electronic structures of the two spin situations in the transition states. Thus, since the reaction is concerted and the respective ferric complexes of the products involve two oxidation equivalents less than the reactant complexes, the two electrons that fill the heme orbitals (Figure 19) must shift in a single step. The orbitals being filled are the π^*_{xz} and a_{2u} orbitals in the LS case and the $\sigma^*_{z^2}$ and a_{2u} orbitals in the HS case. Since the $\sigma^*_{z^2}$ orbital is located along the

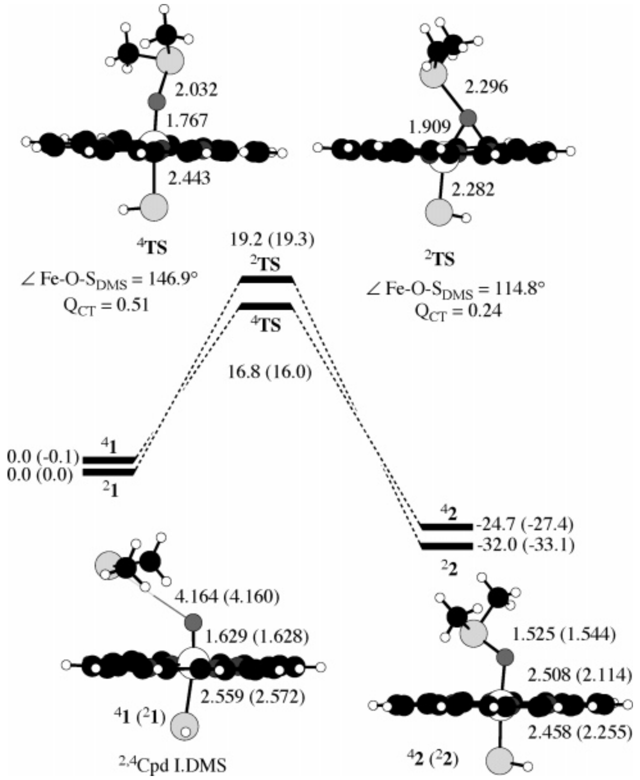

Figure 45. Relative DFT(B3LYP)/LACVP-DZ energies (kcal mol^{-1}) and mechanistic pathways for sulfoxidation of dimethyl sulfide (DMS) by Cpd I. The Q$_{CT}$ values give the charge transfer from DMS to the Cpd I (Por,SH model) moiety in the transition state. (Reprinted with permission from ref 111. Copyright 2003 American Chemical Society.)

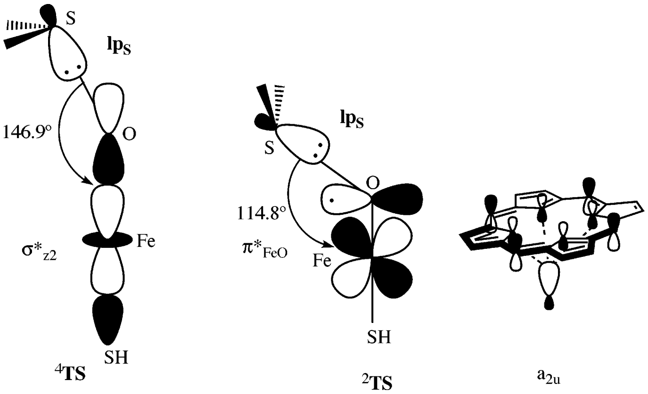

Figure 46. Key orbital interactions in the LS and HS sulfoxidation transition states of Figure 45. These orbital interactions achieve some sulfur−oxygen bonding and transfer of charge to the Cpd I moiety in the TS. Shown also is the a$_{2u}$ orbital that has to be filled during the reaction; its large sulfur contribution causes coalignment with the $\sigma^*_{z^2}$ orbital and facilitates the two-electron reduction of the heme during the process.

S−Fe−O axis, DMS will approach the Fe−O moiety in ^{4}**TS** from the top to achieve a good overlap between the lone pair (lp$_S$) of DMS and the $\sigma^*_{z^2}$ orbital (Figure 46) which leads to the large FeOS$_{DMS}$ angle of 147° in ^{4}**TS** (Figure 45). By contrast, in the LS process filling of the π^*_{xz} orbital requires favorable orbital overlap with the sulfur lone pair, so that DMS approaches Cpd I in a sideways fashion (Figure 46), as verified from the smaller FeOS$_{DMS}$ angle of 115° in ^{2}**TS** (Figure 45). The (lp$_S$)−$\sigma^*_{z^2}$ orbital overlap in ^{4}**TS** is a stabilizing two-electron interaction, while the (lp$_S$)−π^*_{xz} orbital overlap in ^{2}**TS** is a three-electron interaction which is much less stabilizing. Furthermore, and perhaps more important, the overlap of the DMS orbital with the $\sigma^*_{z^2}$ orbital in ^{4}**TS** serves also to fill the a$_{2u}$ orbital since the latter has a large thiolate contribution on the same axis of attack (this requires a three-orbital interaction among lp$_S$, $\sigma^*_{z^2}$, and a$_{2u}$ orbitals). By contrast, the overlap of DMS with the π^*_{xz} orbital in ^{2}**TS** cannot assist the filling of the a$_{2u}$ orbital, which has to be mediated by bending of the Fe−O moiety to create nonzero overlap with the porphyrin orbital. The better overlap stabilization in ^{4}**TS** is apparent by noting the higher degree of charge transfer (Q$_{CT}$) from the DMS to the heme, compared with ^{2}**TS** (see Figure 45). Furthermore, the structure of ^{2}**TS** exhibits a long S$_{DMS}$---O bond, and its Fe−O bond is bent toward the porphyrin; these awkward geometric features of ^{2}**TS** arise from the misalignment of the π^*_{xz} and a$_{2u}$ orbitals and account for the relatively high energy of ^{2}**TS**. The thiolate ligand thus plays a key role in the selection of the lowest transition state for sulfoxidation. This tentative explanation is predictive since with a ligand like imidazole, where the a$_{2u}$ orbital has a smaller ligand contribution, one would expect that now both ^{2}**TS** and ^{4}**TS** will possess awkward geometries. Our preliminary calculations show that this is indeed the case.[238] We emphasize that these ideas are applicable to model mimetic systems, while QM/MM calculations will be required to delineate the role of the protein.

4.12. Regioselectivity in the Reactions of Cpd I

An important function of an enzyme is its ability to carry out regioselective reactions of substrates that have two functionalities. P450 enzymes fulfill this role[1] quite well: they may perform C−H hydroxylations in the presence of double bonds or sulfur or phenyl groups and vice versa (oxidation of these groups in the presence of C−H bonds). Some of these regiochemical problems have been addressed by theory and are discussed below.

4.12.1. Spin-Selective Regiochemistry in Reactions of Cpd I

The emerging picture from all the above reactions involves not only TSR and MSR scenarios but also the possibility of observing *spin-selective regiochemistry*. Thus, as outlined in section 4.4, C−H hydroxylation proceeds via TSR with LS below HS transition states having a radical character on the alkyl group. By contrast, phenyl hydroxylation (section 4.10) proceeds via a dominant LS pathway with electrophilic character. Hence, when two such moieties are present in a substrate, like the one shown in Figure 47a, the two regiochemical processes will proceed via different spin and electromeric states of Cpd I. Since the two processes have different sensitivities to environmental effects and since they may occur in different spin states, the changes in the C−H/Ph ratios are likely to exhibit patterns that would be expected from “two different oxidants”. In addition the spin-selective Ph/C−H competition will affect the product isotope effect observed for the two products of the C−H hydroxylation.[96,202]

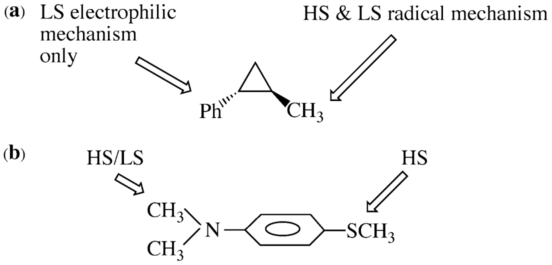

Figure 47. Patterns of spin-selective regiochemistry in two different substrates. (Reprinted with permission from ref 202. Copyright 2004 The Society of Biological Inorganic Chemistry (SBIC).)

Similarly, a substrate like in Figure 47b can undergo competing sulfoxidation and *N*-dealkylation; the latter process occurs via initial C−H hydroxylation. Here too sulfoxidation follows a dominant HS path, while C−H hydroxylation occurs by a TSR scenario with LS below HS situations. In addition, sulfoxidation has a much higher electrophilic character (see Q_{CT} in ^{4}**TS**, Figure 45) than C−H hydroxylation. As such, the sulfoxidation/*N*-dealkylation competition will exhibit patterns that might be taken as evidence for the involvement of two oxidants. Mechanistic observations which can be interpreted as a result of two competent oxidants are widespread in the literature, e.g., Newcomb et al.[196,201] in the case of the substrate in Figure 47a and Volz et al.[239] in the case of the substrate in Figure 47b. However, theory suggests that quite a few of these observations may be caused by spin-selective regiochemistry of a single oxidant. Taking the sulfoxidation/*N*-dealkylation competition reactions as an example, (a) the putative second oxidant, Cpd 0 (ferric−hydroperoxide) is computed to be a very sluggish oxidant,[111] uncompetitive with Cpd I (see Figure 31), (b) Cpd I model species are known to carry out sulfoxidation,[240] and (c) Cpd I is the sole oxidant responsible for the initial C−H hydroxylation en route to the *N*-dealkylation reaction.[159] Thus, if Cpd I is indeed responsible for both sulfoxidation and *N*-dealkylation, the trends that appeared like coming from two oxidants originate in fact from the spin-selective regiochemistry of Cpd I.

4.12.2. Competitive Epoxidation and Allylic Hydroxylation in Propene Oxidation by Cpd I

Using propene as a model substrate de Visser et al.[93,94] studied the competition between C−H hydroxylation and C=C epoxidation. The potential-energy profiles for the two processes are shown in Figure 48. As before (e.g., Figures 21 and 36), the processes follow TSR with effectively concerted LS pathways and stepwise HS mechanisms. The reaction barriers (via ^{4,2}**TS**$_E$ and ^{4,2}**TS**$_H$) with ZPE are compacted within 0.5 kcal mol^{-1}, and as such, Cpd I by itself is completely nonselective in the C=C/C−H competition.

The effect of polarity and hydrogen bonding on the four different bond-activation transition states (^{4,2}**TS**$_E$ and ^{4,2}**TS**$_H$) of propene are shown in Figure 49. The left-hand side depicts the situation in the gas phase where the four species are almost isoenergetic, and hence, no selectivity whatsoever is expected. The addition of two NH---S hydrogen bonds, *ca. 4 Å away from the reaction center*, is sufficient to stabilize the ^{2}**TS**$_H$ species below all others and open a gap of 4.5 kcal mol^{-1} between the four species. Addition of a dielectric medium of low polarity (dielectric constant of $\epsilon = 5.7$) further enhances the differences. Now the hydroxylation transition states are well below those for epoxidation, and for each process the lowest energy species is the LS transition state. Thus, environmental effects are seen to create both regioselectivity and stereoselectivity by strongly preferring C−H hydroxylation over C=C epoxidation as well as favoring the effectively concerted pathways of both processes. This emergent selectivity highlights *the response of a chameleon oxidant to the polarity and hydrogen-bonding capability of the environment*. A more recent study shows[241] that an electric field alone can achieve selectivity in this reaction. This is an exciting result, which raises the possibility that the selectivity of P450 isozymes is controlled at least in part by the electric field of the protein.

Experimental observations of Groves et al.[242] show that epoxidation of propene by P450$_{LM2}$ leads exclusively to the epoxide. By contrast, other alkenes, such as cyclohexene, were found to give competitive hydroxylation and epoxidation reactions.[195,243] Clearly, QM/MM investigations of these reactions will be needed to reveal the interplay of the factors that determine the outcome of C=C/C−H competition inside a protein pocket.

4.13. Miscellaneous Studies

Other theoretical studies were conducted to understand the reactivity of the enzyme heme−oxygenase (HO), which apparently employs a Cpd 0 in the heme degradation mechanism.[244,245] In both studies the concerted mechanism was ruled out. One study[244] proposed stepwise mechanisms that involve initial O−O bond homolysis followed by OH• radical collapse on the meso position of the porphyrin. Lewis et al.[246] studied the metabolism of substrate oxidation by P450$_{2E1}$ using quantitative structure−activity relationship analysis of maximum oxidative rates (V_{max} data) and semiempirically calculated properties of the reactants. Reasonable correlations were obtained between log V_{max} and the HOMO−LUMO gaps or ionization potentials of the substrates, calculated by the AM1 method.

4.14. Overview of Reactivity Features of Cpd I

As shown by the theoretical calculations, Cpd I is a two-state oxidant and therefore generally participates in two-state reactivity involving competitive LS and HS pathways; the LS reactions are nonsynchronous but normally effectively concerted, while the HS processes are stepwise. The reagent has, however, additional features which make it a highly versatile electrophile.

(a) The d-block orbitals, the porphyrin a_{2u} orbital, and the orbitals of the substrate undergoing oxidation form a dense orbital manifold (see Figures 4, 19, and 38), which may lead to multistate reactivity, with state- and spin-specific reactions. The most common

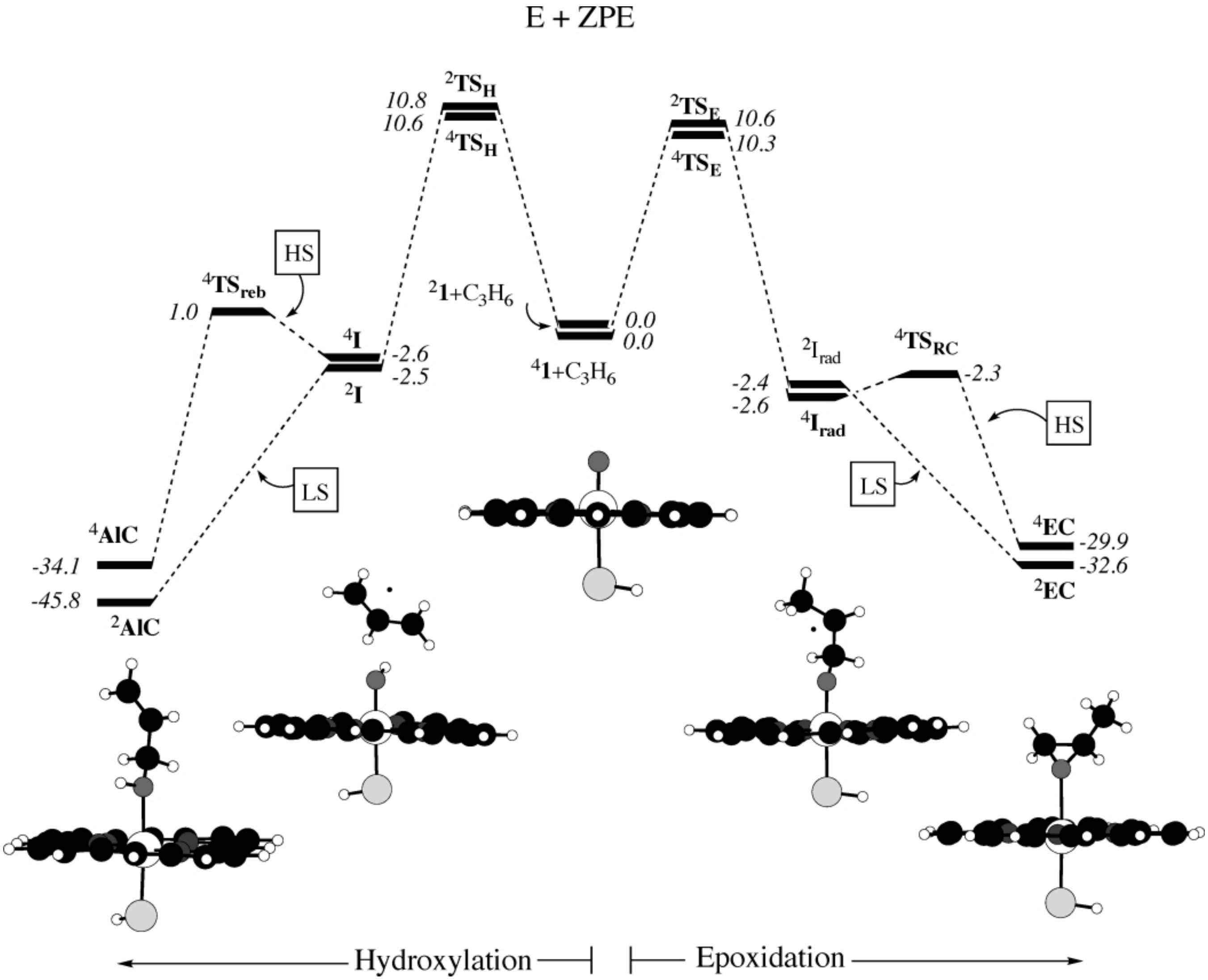

Figure 48. Relative DFT(B3LYP)/LACVP-DZ energies with ZPE correction (kcal mol^{-1}) and mechanistic pathways for hydroxylation and epoxidation of propene by Cpd I (Por,SH model) in the gas phase. (Reprinted with permission from ref 94. Copyright 2002 American Chemical Society.)

intermediate species involve carbon radicals and cations in different spin manifolds (e.g., C−H hydroxylation in *trans*-phenylisopropylcyclopropane, C=C epoxidation in ethene and styrene, benzene hydroxylation).

(b) In some reactions, e.g., benzene hydroxylation and sulfoxidation, one of the spin manifolds (LS and HS, respectively) is dominant. This leads to intriguing spin-selective regiochemistry in substrates which include different moieties that are affected by different spin states, e.g., as in Figure 47.

(c) Cpd I is a chameleon species that adapts its electronic structure to the environment which accommodates it. As such, its reactivity can be tuned by environmental factors, e.g., the polarity and hydrogen bonding. The impact of these factors is apparent in the competition of C−H hydroxylation and C=C epoxidation (Figures 48 and 49).

Another feature extracted from the theoretical calculations regards the function of the heme. Thus, the porphyrin ligand is not an innocent spectator but plays the role of an electron sink by accepting an electron during the oxidation process. It is also able to abstract and then reshuttle protons, thereby causing rearrangements in the substrate (e.g., aldehyde formation in styrene epoxidation, NIH shift during benzene hydroxylation). Additionally, the heme can be alkylated as a side reaction of epoxidation. The calculations show that the strong electron-donor property of the thiolate ligand protects the porphyrin to some extent against heme alkylation[37,81,181] but enhances its basicity, making it a good proton shuttle.

Much of the available theoretical evidence points to a Cpd I-only scenario in P450 reactivity. While it is true that one often observes reactions of species analogous to Cpd 0, like ferric-alkyl peroxides, in model heme compounds[166] one must remember that Cpd 0 of P450 carries a negative charge and does not favor electrophilic reactivity. Figure 31 further shows that even in the presence of a proton source Cpd 0 is still sluggish and cannot compete with Cpd I. Of course, there might be other possible oxidants that could participate in the P450 chemistry as electrophiles. A candidate is the one-electron-reduced species, so-called Cpd II, which has proven to be reactive

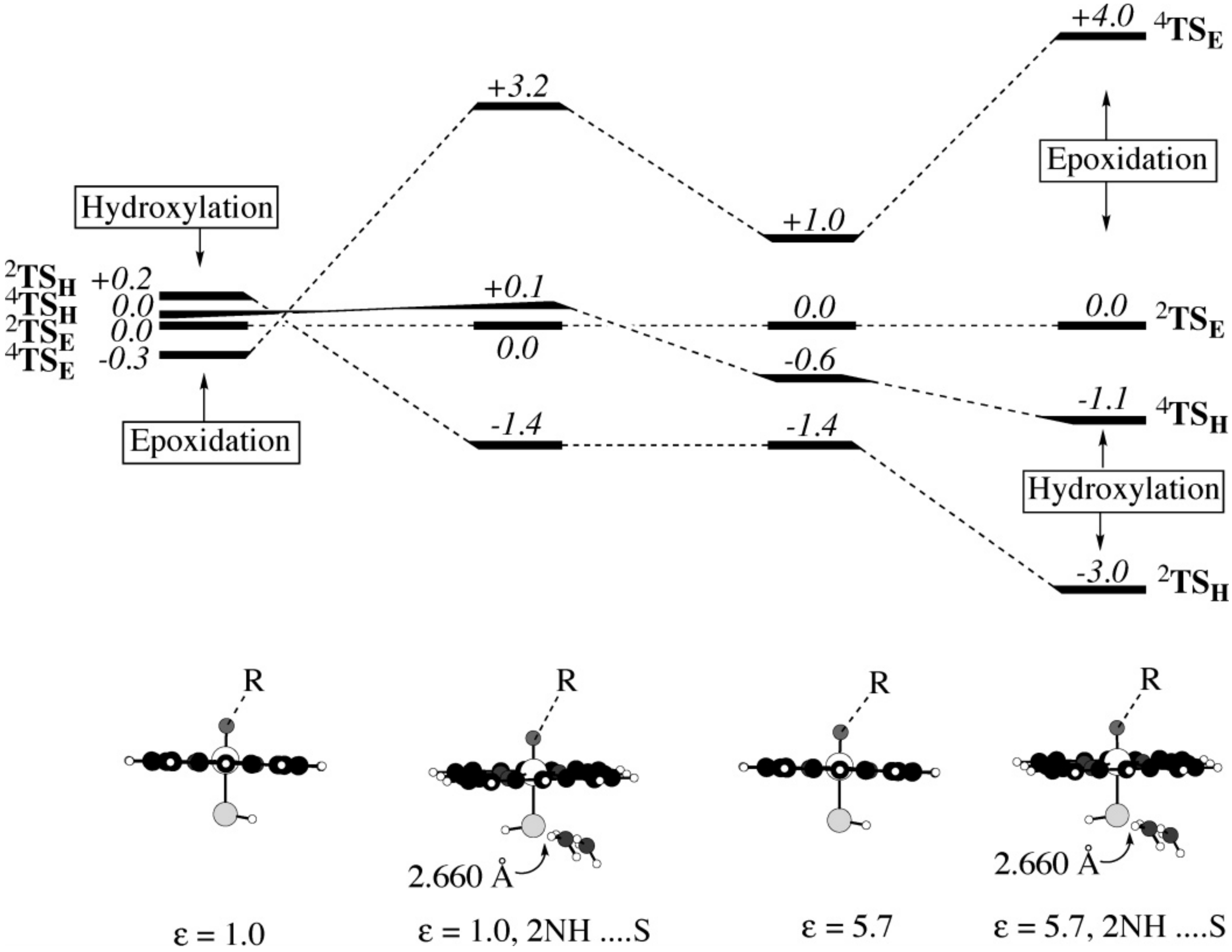

Figure 49. Relative DFT(B3LYP)/LACVP-DZ energies (kcal mol^{-1}) and ZPE corrections for $^{4,2}\mathbf{TS}_E$ and $^{4,2}\mathbf{TS}_H$ transition states (see Figure 48) under different conditions; ϵ is a dielectric constant, and 2NH---S refers to hydrogen bonding to the thiolate ligand. (Reprinted with permission from ref 93. Copyright 2002 Wiley-VCH Verlag GmbH, 69451 Weinheim, Germany.)

even in C−H hydroxylation.[167] Other candidates are protonated forms of Cpd 0. All these alternatives merit further computational studies.

5. Concluding Remarks

Theoretical treatments of enzymes have advanced to the point that they enable the study of the complete catalytic cycle of cytochrome P450. They afford three-dimensional structures, energies, electron and spin density distributions, and other properties of intermediates and transition states and provide insight about the electronic factors that govern stability and reactivity. DFT calculations can be used to investigate models of cytochrome P450 systems with typically up to about 100 atoms or so (including heme and substrate and possibly also a few neighboring residues and water molecules). They aim at elucidating the intrinsic properties of the active center. DFT/MM calculations on P450 enzymes include the full protein and water environment, with thousands of atoms (typically around 25 000), and thereby allow a detailed analysis of how the environment affects and modulates the electronic structure, stability, and reactivity of the species in the P450 catalytic cycle.

The accuracy of the DFT and DFT/MM results is obviously limited by the currently available functionals and the necessity to use rather small basis sets for the relatively large P450 systems. Moreover, as discussed in the preceding sections, there is not yet a universally accepted canonical procedure for DFT/MM calculations, and different possible choices in the setup of such calculations introduce some additional uncertainty. While the capabilities of DFT and DFT/MM will undoubtedly improve with time through further methodological developments, it has also become apparent by extensive validation studies in several groups that the current technology is good enough for meaningful investigations of metalloenzymes such as cytochrome P450, for example, using B3LYP and B3LYP/CHARMM with LACVP-type basis sets and an electronic QM/MM embedding. Given the above caveats, one should not overestimate the quantitative accuracy of DFT and DFT/MM treatments but rather focus on the qualitative conclusions that emerge from these calculations.

One such qualitative finding is two-state and multistate reactivity in cytochrome P450 enzymes. The calculations invariably find two or more low-lying spin states with energies that are lower than the typical barriers for enzymatic transformations, so that there can be no doubt about the energetic accessibility of these spin states during the catalytic cycle. It has indeed been shown that TSR and MSR scenarios can rationalize many puzzling experimental observations on P450 reactivity.[247] The DFT and DFT/MM studies indicate state-selective and spin-selective reactions and for some substrates even spin-selective regiochemistry. The actual kinetics of these processes will depend on the probability of spin crossover, which is normally (tacitly) assumed not to constitute a bottleneck in P450 reactions. There is a clear need for more quantitative theoretical studies of spin crossover in order to better assess the role of TSR and MSR in P450 chemistry.

Several other qualitative features have been elucidated through recent DFT and DFT/MM calculations. These include the "push" effect of the axial thiolate ligand that gates the catalytic cycle, the proton-relay machinery (Thr_{252}, Glu_{366}, Asp_{251}) that is essential for Cpd I formation, the hydrogen-bonding machinery (Leu_{358}, Gly_{359}, Gln_{360}) that stabilizes Cpd I, and the role of the porphyrin ligand that acts as an electron sink during the oxidation of the substrate by Cpd I. The DFT/MM investigations indicate that the protein environment often has a decisive influence, for example, on the structure of the resting state (orientation of the water ligand), the nature of the electronic ground state of the pentacoordinated ferrous complex (quintet electromer $^5\mathbf{3}_{x^2-y^2}$), and the electronic structure and spin density distribution in Cpd I (porphyrin-centered radical in the enzyme). The protein environment is also instrumental for achieving stereoselectivity in C−H hydroxylation of camphor (through hydrogen bonding to Tyr_{96} and other interactions), while the role of residues near the heme side-chain propionates is still being debated for this reaction (proposed differential stabilization of the transition state through electrostatic interactions between Arg_{299} and propionate).

While much understanding of P450 chemistry has already been achieved in recent years through theoretical calculations, much remains to be done, of course. Many examples have been given throughout the text where it would be most desirable to complement the existing DFT model studies by DFT/MM investigations in order to assess the influence of the protein environment more reliably. There are many experimental studies of P450 mutants that are relevant mechanistically, and it would clearly be appropriate to perform the corresponding theoretical work. Dynamical aspects in P450 have generally only been addressed at the classical force-field level up to now, and it would certainly be of interest to study them also at higher levels, for example, with regard to the role of water molecules in the pocket and the various proton-relay mechanisms. Finally, there is a need for a thorough thermodynamical analysis of the whole catalytic cycle in the enzyme, which may also involve, in the reduction step, a treatment of the interactions with the reductase protein. These and other open issues call for further theoretical work.

6. Abbreviations

AC	aldehyde complex
Alk	alkyl
AlkH	alkane
AM1	Austin Model 1 (a semiempirical method)
Arg	arginine
Asp	aspartic acid
B3LYP	hybrid functional used in DFT consisting of 20% Hartree−Fock and 80% Becke88 exchange combined with the Lee−Yang−Parr correlation functional
BDE	bond dissociation energy
BHLYP	hybrid functional used in DFT, consisting of one-half Hartree−Fock and one-half Becke88 exchange combined with the Lee−Yang−Parr correlation functional
BO	ferric benzene oxide complex
BP86	pure gradient-corrected functional used in DFT consisting of Becke88 exchange and Perdew86 correlation functional
BPW91	pure gradient-corrected functional used in DFT consisting of Becke88 exchange and Perdew−Wang91 correlation functional
CASSCF	complete active space self-consistent field method
CCSD(T)	coupled cluster method with single and double excitations and a perturbative treatment of triple excitations
CI	configuration interaction
Cpd I	active species of heme enzymes, Compound I, involving Fe(IV)O and a porphyrin radical cation
D251N	mutant of $\mathrm{P450}_{\mathrm{cam}}$ in which Asp251 is replaced by asparagine (N)
DFT	density functional theory
DFT/MM	density functional/molecular mechanical method, a variant of QM/MM
DMS	dimethyl sulfide
DZ	double-ζ basis set
DZVP	double-ζ basis set with valence polarization
EC	ferric epoxide complex
$\mathrm{E_nC}$	enol complex of ferric heme and 1-hydroxo styrene
EPR/ENDOR	electron paramagnetic resonance/electron−nuclear double resonance
ESEEM	electron spin−echo envelope modulation spectroscopy
fs	femtosecond
Gln	glutamine
Glu	glutamic acid
HO	heme-oxygenase
HOMO	highest occupied molecular orbital
HRP	horseradish peroxidase
HS	high spin
INDO	intermediate neglect of differential overlap (a semiempirical method)
KIE	kinetic isotope effect
KSIE	kinetic solvent isotope effect
LACV3P+*	triple-ζ basis set augmented with diffuse and polarization functions describing the valence orbitals on the transition metal (the core is described by an effective core potential) combined with 6-311+G* for other atoms

LACVP	double-ζ basis set describing the valence orbitals on the transition metal (the core is described by an effective core potential) combined with 6-31G on all other atoms
LS	low spin
LUMO	lowest unoccupied molecular orbital
MD	molecular dynamics
MM	molecular mechanics
MSR	multistate reactivity
P	products
P450	cytochrome P450 enzymes
PIE	product isotope effect = the ratio of KIE for different products
pK_a	p$K_a = -\log K_a$, K_a is the dissociation constant of an acid
Por	porphyrin or porphine
PPIX	protoporphyrin IX, the native porphyrin for heme enzymes
ps	picoseconds
Q_{CT}	charge transfer
QM	quantum mechanics
QM/MM	hybrid method that couples a quantum mechanical (QM) method and a molecular mechanical (MM) method. The QM method can be DFT, hence QM(DFT)/MM
RC	reactant complex
ROB3LYP	restricted open-shell B3LYP
ROHF	restricted open-shell Hartree–Fock
SAM1	semiempirical method based on AM1
SC	suicidal complex
SCys	cysteinate
SMe	methyl mercaptide
T252A	$P450_{cam}$ mutant created by replacement of threonine 252 (Thr252) by alanine
Thr	threonine
TS	transition state
TS_E	epoxidation transition state
TS_H	hydroxylation transition state
TSR	two-state reactivity
Tyr	tyrosine
TZ	triple-ζ basis set
UB3LYP	unrestricted B3LYP
W	water molecule
WT	wild type (native enzyme)
ZPE	zero-point energy
τ_{app}	apparent radical lifetime
τ_{real}	real radical lifetime

7. Acknowledgements

The research at the Hebrew university is supported in part by an ISF grant to S.S.. The joint research of W.T. and S.S. is supported by a common GIF grant.

8. References

(1) (a) *Cytochrome P450: structure, mechanism and biochemistry,* 2nd ed.; Ortiz de Montellano, P. R., Ed.; Plenum Press: New York, 1995. (b) *Cytochrome P450: structure, mechanism and biochemistry*, 3rd ed.; Ortiz de Montellano, P. R., Ed.; Kluwer Academic/Plenum Publishers: New York, 2004.

(2) Dawson, J. H.; Sono, M. *Chem. Rev.* **1987**, *87*, 1255.

(3) Sono, M.; Roach, M. P.; Coulter, E. D.; Dawson, J. H. *Chem. Rev.* **1996**, *96*, 2841.

(4) Woggon, W.-D. *Top. Curr. Chem.* **1996**, *184*, 39.

(5) Groves, J. T.; Han, Y.-Z. Models and mechanisms of Cytochrome P450 action. In *Cytochrome P450: structure, mechanism and biochemistry,* 2nd ed.; Ortiz de Montellano, P. R., Ed.; Plenum Press: New York, 1995; Chapter 1, p 3.

(6) Groves, J. T. *J. Chem. Educ.* **1985**, *62*, 928.

(7) Ortiz de Montellano, P. R. Oxygen Activation and Reactivity. In *Cytochrome P450: structure, mechanism and biochemistry,* 2nd ed.; Ortiz de Montellano, P. R., Ed.; Plenum Press: New York, 1995; Chapter 8, p 245.

(8) Ortiz de Montellano, P. R. *Trends Pharm. Sci.* **1989**, *10*, 354.

(9) Ortiz de Montellano, P. R.; De Voss, J. J. *Natl. Prod. Rep.* **2002**, *19*, 477.

(10) Sligar, S. G. *Essays Biochem.* **1999**, *34*, 71.

(11) Guengerich, F. P.; McDonald, T. L. *FASEB J.* **1990**, *4*, 2453.

(12) Watanabe, Y. *J. Biol. Inorg. Chem.* **2001**, *6*, 846.

(13) Guengerich, F. P. Human Cytochrome P450 Enzymes. In *Cytochrome P450: structure, mechanism and biochemistry,* 2nd ed.; Ortiz de Montellano, P. R., Ed.; Plenum Press: New York, 1995; Chapter 14, p 473.

(14) Poulos, T. L.; Cupp-Vickery, J.; Li, H. Structural Studies on Prokaryotic Cytochromes P450. In *Cytochrome P450: structure, mechanism and biochemistry,* 2nd ed.; Ortiz de Montellano, P. R., Ed.; Plenum Press: New York, 1995; Chapter 4, p 125.

(15) Lewis, D. F. V. *Guide to cytochromes P450*. Taylor and Francis: New York, 2001.

(16) Guengerich, F. P. *Annu. Rev. Pharmacol. Toxicol.* **1999**, *39*, 1.

(17) (a) See *Book of Abstracts*; The 13th International Conference on Cytochromes P450: Biochemistry, Biophysics and Drug Metabolism, Prague, June 29–July 3, 2003. (b) For corresponding proceedings, see: *Proceedings of the 13th International Conference on Cytochrome P450. Biochemistry, Biophysics and Drug Metabolism*; Anzenbacher, P., Hudecek, J., Eds.; Monduzzi Editore: Bologna, Italy, 2003.

(18) Harris, D. L. *Curr. Opin. Drug Discov*. **2004**, *7*, 43.

(19) (a) Schröder, D.; Schwarz, H. *Angew. Chem., Int. Ed. Engl.* **1995**, *34*, 1973. (b) Neumann, R. *Prog. Inorg. Chem.* **1998**, *47*, 317. (c) Sheldon, R. A.; Kochi, J. K. *Metal-Catalyzed Oxidations of Organic Compounds;* Academic Press: New York, 1981. (d) McLain, J. L.; Lee, J.; Groves, J. T. In *Biomimetic Oxidations Catalyzed by Transition Metal Complexes*; Meunier, B., Ed.; Imperial College Press: London, 1999; Chapter 3. (e) Schröder, D.; Schwarz, H.; Shaik, S. In *Structure and Bonding*; Meunier, B., Ed.; Springer-Verlag: Heidelberg, Germany, 2000; Vol. 97, p 92.

(20) (a) Groves, J. T.; Shalyaev, K.; Lee, J. In *The Porphyrin Handbook*; Kadish, K. M., Smith, K. M., Guilard, R., Eds.; Academic Press: New York, 2000; Vol. 4, p 17. (b) Groves, J. T. *J. Porphyrins Phthalocyanines* **2000**, *4*, 350. (c) Meunier, B. *J. Porphyrins Phthalocyanines* **2000**, *4*, 353. (d) Watanabe, Y. In *The Porphyrin Handbook*; Kadish, K. M., Smith, K. M., Guilard, R., Eds.; Academic Press: New York, 2000; Vol. 4, p 97. (e) Meunier, B.; Bernadou, J. *Struct. Bonding* **2000**, *97*, 1. (f) Meunier, B.; Bernadou, J. *Top. Catal.* **2002**, *21*, 47. (g) Feiters, M. C.; Rowan, A. E.; Nolte, R. J. M. *Chem. Soc. Rev.* **2000**, *29,* 375. (h) Wagenknecht, H.-A.; Woggon, W.-D. *Angew. Chem., Int. Ed. Engl.* **1997**, *36*, 390. (i) Staubli, B.; Fretz, H.; Piantini, U.; Woggon, W.-D. *Helv. Chim. Acta* **1987**, *70*, 1173. (j) Woggon, W.-D.; Wagenknecht, H. A.; Claude, C. *J. Inorg. Biochem.* **2001**, *83*, 289. (k) Chen, K.; Costas, M.; Que, L., Jr. *J. Chem. Soc., Dalton Trans.* **2002**, *5*, 672.

(21) Meunier, B.; de Visser, S. P.; Shaik, S. *Chem. Rev*. **2004**, *104*, 3947.

(22) See http://drnelson.utmem.edu/CytochromeP450.html.

(23) See the surprising substrate binding by $P450_{3A4}$: Williams, P. A.; Cosme, J.; Vonkovic, M. D.; Ward, A.; Angove, H. C.; Day, P. J.; Vonrhein, I. J.; Jhoti, T. H. *Science* **2004**, *305*, 683.

(24) Poulos, T. L. *J. Biol. Inorg. Chem.* **1996**, *1*, 356.

(25) Poulos, T. L.; Finzel, B. C.; Howard, A. J. *Biochemistry* **1986**, *25*, 5314.

(26) Poulos, T. L.; Finzel, B. C.; Howard, A. J. *J. Mol. Biol.* **1987**, *195*, 687.

(27) Poulos, T. L. In *The Porphyrin Handbook*; Kadish, K. M., Smith, K. M., Guilard, R., Eds.; Academic Press: New York, 2000; Vol 4, p 190.

(28) Schlichting, I.; Berendzen, J.; Chu, K.; Stock, A. M.; Maves, S. A.; Benson, D. E.; Sweet, R. M.; Ringe, D.; Petsko, G. A.; Sligar, S. G. *Science* **2000**, *287*, 1615.

(29) Loew, G. H.; Kert, C. J.; Hjelmeland, L. M.; Kirchner, R. F. *J. Am. Chem. Soc.* **1977**, *99*, 3534.

(30) Yamamoto, S.; Teraoka, J.; Kashiwagi, H. *J. Chem. Phys.* **1988**, *88*, 303.

(31) Yamamoto, S.; Kashiwagi, H. *Chem. Phys. Lett.* **1989**, *161*, 85.

(32) For some reviews, see: (a) Aqvist, J.; Warshel, *A. Chem. Rev.* **1993**, *93*, 2523. (b) Gao, J. in *Reviews in Computational Chemistry;* Lipkowitz, K. B., Boyd, D. B., Eds.; VCH: Weinheim, 1995; Vol 7, p 119. (c) Mordasini, T. Z.; Thiel, W. *Chimia* **1998**, *52*, 288. (d) Monard, G.; Merz, K. M., Jr. *Acc. Chem. Res.* **1999**, *32*, 904. (e) Sherwood, P. In *Modern Methods and Algorithms of Quantum Chemistry;* Grotendorst, J., Ed.; NIC Series 3; John von Neumann Institute for Computing: Jülich, 2000; p 285. (f) Gao, J.; Truhlar, D. G. *Annu. Rev. Phys. Chem.* **2002**, *53*, 467. (g) Field, M. J. *J. Comput. Chem.* **2002**, *23*, 48. (h) Monard, G.; Prat-Resina, X.; Gonzalez-Lafont, A.; Lluch, J. M. *Int. J. Quantum Chem.* **2003**, *93*, 229. (i) Ridder, L.; Mulholland, A. *Curr. Top. Med. Chem.* **2003**, *3*, 1241.

(33) Loew, G. H.; Harris, D. L. *Chem. Rev.* **2000**, *100*, 407.

(34) Harris, D. L. *Curr. Opin. Chem. Biol.* **2001**, *5*, 724.

(35) Shaik, S.; de Visser, S. P.; Ogliaro, F.; Schwarz, H.; Schröder, D. *Curr. Opin. Chem. Biol.* **2002**, *6*, 556.

(36) Shaik, S.; Cohen, S.; de Visser, S. P.; Sharma, P. K.; Kumar, D.; Kozuch, S.; Ogliaro, F.; Danovich, D. *Eur. J. Inorg. Chem.* **2004**, *35*, 207.

(37) Shaik, S.; de Visser, S. P. *Computational Approaches To Cytochrome P450 Function*. In *Cytochrome P450: structure, mechanism and biochemistry*, 3rd ed.; Ortiz de Montellano, P. R., Ed.; Kluwer Academic/Plenum Publishers: New York, 2004; Chapter 2, p 45.

(38) Cramer, C. J. *Essentials of Computational Chemistry: Theories and Models;* Wiley: Chichester, 2002.

(39) Loew, G. H.; Dupuis, M. *J. Am. Chem. Soc*. **1997**, *119*, 9848.

(40) Ghosh, A.; Presson, B. J.; Taylor, P. R. *J. Biol. Inorg. Chem.* **2003**, *8*, 507.

(41) Ghosh, A.; Taylor, P. R. *Curr. Opin. Chem. Biol.* **2003**, *7*, 113.

(42) Himo, F.; Siegbahn, P. E. M. *Chem. Rev.* **2003**, *103*, 2421.

(43) Siegbahn, P. E. M.; Blomberg, M. R. A *Chem. Rev*. **2000**, *100*, 421.

(44) Curtiss, L. A.; Raghavachari, K.; Redfern, P. C.; Pople, J. A. *J. Chem. Phys.* **2000**, *112*, 7374.

(45) Koch, W.; Holthausen, M. C. *A Chemist's Guide to Density Functional Theory*; Wiley-VCH: Weinheim, 2000.

(46) Pople, J. A.; Gill, P. M. W.; Handy, N. C. *Int. J. Quantum Chem.* **1995**, *56*, 303.

(47) Mohr, M.; McNamara, J. P.; Wang, H.; Rajeev, S. A.; Ge, J.; Morgado, C. A.; Hillier, I. H. *Faraday Discuss.* **2003**, *124*, 413.

(48) Göller, A. H.; Clark, T. *J. Mol. Struct. (THEOCHEM)* **2001**, *541*, 263.

(49) Harris, D. L.; Loew, G. H. *J. Am. Chem. Soc.* **1993**, *115*, 8775.

(50) (a) Lüdemann, S. K.; Lounnas, V.; Wade, R. C. *J. Mol. Biol.* **2000**, *303*, 797. (b) Lüdemann, S. K.; Lounnas, V.; Wade, R. C. *J. Mol. Biol.* **2000**, *303*, 813.

(51) Helms, V.; Wade, R. C. *Proteins* **1998**, *32*, 381.

(52) Wade, R. C.; Winn, P. J.; Schlichting, I.; Sudarko *J. Inorg. Biochem.* **2004**, *98*, 1175.

(53) Winn, P. J.; Lüdemann, S. K.; Gauges, R.; Lounnas, V.; Wade, R. C. *Proc. Natl. Acad. Sci. U.S.A.* **2002**, *99*, 5361.

(54) Das, B.; Helms, V.; Lounnas, V.; Wade, R. C. *J. Inorg. Biochem.* **2000**, *81*, 121.

(55) Hermans, J.; Wang. L. *J. Am. Chem. Soc.* **1997**, *119*, 2707.

(56) Kairys, V.; Gilson, M. K. *J. Comput. Chem.* **2002**, *23*, 1656.

(57) De Voss, J. J.; Sibbesen, O.; Zhang, Z.; Ortiz de Montellano, P. R. *J. Am. Chem. Soc.* **1997**, *119*, 5489.

(58) Warshel, A.; Levitt, M. *J. Mol. Biol.* **1976**, *103*, 227.

(59) Field, M. J.; Bash, P. A.; Karplus, M. *J. Comput. Chem.* **1990**, *11*, 700.

(60) Bakowies, D.; Thiel, W. *J. Phys. Chem.* **1996**, *100*, 10580.

(61) Gao, J.; Xia, X. *Science* **1992**, *258*, 631.

(62) Ryde, U. *Curr. Opin. Chem. Biol.* **2003**, *7*, 136.

(63) Singh, U. C.; Kollman, P. A. *J. Comput. Chem.* **1986**, *7*, 718.

(64) Antes, I.; Thiel, W. *J. Phys. Chem. A* **1999**, *103*, 9290.

(65) Zhang, Y.; Lee, T.-S.; Yang, Y. *J. Chem. Phys.* **1999**, *110*, 46.

(66) Thery, V.; Rinaldi, D.; Rivail, J.-L.; Maigret, B.; Ferenczy, G. *J. Comput. Chem.* **1994**, *15*, 269.

(67) Gao, J.; Amara, P.; Alhambra, C.; Field, M. J. *J. Phys. Chem. A* **1998**, *102*, 4714.

(68) Murphy, R. B.; Philipp, D. M.; Friesner, R. A. *J. Comput. Chem.* **2000**, *21*, 1442.

(69) Murphy, R. B.; Philipp, D. M.; Friesner, R. A. *Chem. Phys. Lett.* **2000**, *321*, 113.

(70) Antes, I.; Thiel, W. In *Combined Quantum Mechanical and Molecular Mechanical Methods*; Gao, J., Thompson, M. A., Eds.; ACS Symposium Series 712; American Chemical Society: Washington, DC, 1998; p 50.

(71) Reuter, N.; Dejaegere, A.; Maigret, B.; Karplus, M. *J. Phys. Chem. A* **2000**, *104*, 1720.

(72) Sherwood, P.; de Vries, A. H.; Guest, M. F.; Schreckenbach, G.; Catlow, C. R. A.; French, S. A.; Sokol, A. A.; Bromley, S. T.; Thiel, W.; Turner, A. J.; Billeter, S.; Terstegen, F.; Thiel, S.; Kendrick, J.; Rogers, S. C.; Casci, J.; Watson, M.; King, F.; Karlsen, E.; Sjovoll, M.; Fahmi, A.; Schäfer, A.; Lennartz, C. *J. Mol. Struct. (THEOCHEM)*, **2003**, *632*, 1.

(73) Lennartz, C.; Schäfer, A.; Terstegen, F.; Thiel, W. *J. Phys. Chem. B* **2002**, *106*, 1758.

(74) Billeter, S. R.; Turner, A. J.; Thiel, W. *Phys. Chem. Chem. Phys.* **2000**, *2*, 2177.

(75) Lounnas, V.; Wade, R. C. *Biochemistry* **1997**, *36*, 5402.

(76) Hay, J. P.; Wadt, W. R. *J. Chem. Phys.* **1985**, *82*, 299.

(77) Friesner, R. A.; Murphy, R. B.; Beachy, M. D.; Ringlanda, M. N.; Pollard, W. T.; Dunietz, B. D.; Cao, Y. X. *J. Phys. Chem. A* **1999**, *103*, 1913.

(78) Loew, G. H. *Int. J. Quantum Chem.* **2000**, *77*, 54.

(79) Rydberg, P.; Sigfridsson, E.; Ryde, U. *J. Biol. Inorg. Chem.* **2004**, *9*, 203.

(80) Ogliaro, F.; de Visser, S. P.; Cohen, S.; Sharma, P. K.; Shaik, S. *J. Am. Chem. Soc.* **2002**, *124*, 2806.

(81) Ogliaro, F.; de Visser, S. P.; Shaik, S. *J. Inorg. Biochem.* **2002**, *91*, 554.

(82) Hata, M.; Hirano, Y.; Hoshino, T.; Nishida, R.; Tsuda, M. *J. Phys. Chem. B* **2004**, *108*, 1189.

(83) Schöneboom, J. C.; Lin, H.; Reuter, N.; Thiel, W.; Cohen, S.; Ogliaro, F.; Shaik, S. *J. Am. Chem. Soc.* **2002**, *124*, 8142.

(84) Schöneboom, J. C.; Cohen, S.; Lin, H.; Shaik, S.; Thiel, W. *J. Am. Chem. Soc.* **2004**, *126*, 4017.

(85) Schöneboom, J. C.; Thiel, W. *J. Phys. Chem. B* **2004**, *108*, 7468.

(86) Schöneboom, J. C. Ph.D. Thesis, University of Düsseldorf, Germany, 2003.

(87) Lin, H.; Schöneboom, J. C.; Cohen, S.; Shaik, S.; Thiel, W. *J. Phys. Chem. B* **2004**, *108*, 10083.

(88) Altun, A.; Thiel, W. *J. Phys. Chem. B* **2005**, *109*, 1268.

(89) Guallar, V.; Friesner, R. A. *J. Am. Chem. Soc.* **2004**, *126*, 8501.

(90) Guallar, V.; Baik, M.; Lippard, S. J.; Friesner, R. A. *Proc. Natl. Acad. Sci. U.S.A.* **2003**, *100*, 6998.

(91) Ogliaro, F.; Harris, N.; Cohen, S.; Filatov, M.; de Visser, S. P.; Shaik, S. *J. Am. Chem. Soc.* **2000**, *122*, 8977.

(92) Ogliaro, F.; Filatov, M.; Shaik, S. *Eur. J. Inorg. Chem.* **2000**, 2455.

(93) de Visser, S. P.; Ogliaro, F.; Sharma, P. K.; Shaik, S. *Angew. Chem., Int. Ed.* **2002**, *41*, 1947.

(94) de Visser, S. P.; Ogliaro, F.; Sharma, P. K.; Shaik, S. *J. Am. Chem. Soc.* **2002**, *124*, 11809.

(95) Kumar, D.; de Visser, S. P.; Shaik, S. *J. Am. Chem. Soc.* **2003**, *125*, 13024.

(96) Kumar, D.; de Visser, S. P.; Sharma, P. K.; Cohen, S.; Shaik, S. *J. Am. Chem. Soc.* **2004**, *126*, 1907.

(97) Kumar, D.; de Visser, S. P.; Shaik, S. *J. Am. Chem. Soc.* **2004**, *126*, 5072.

(98) de Visser, S. P.; Kumar, D.; Cohen, S.; Shacham, R.; Shaik, S. *J. Am. Chem. Soc.* **2004**, *126*, 8362.

(99) Yoshizawa, K.; Kamachi, T.; Shiota, Y. *J. Am. Chem. Soc.* **2001**, *123*, 9806.

(100) Yoshizawa, K.; Ohta, T.; Eda, M.; Yamabe, T. *Bull. Chem. Soc. Jpn.* **2000**, *73*, 401.

(101) Yoshizawa, K.; Shiota, Y.; Kagawa, Y. *Bull. Chem. Soc. Jpn.* **2000**, *73*, 2669.

(102) Yoshizawa, K.; Kagawa, Y.; Shiota, Y. *J. Phys. Chem. B* **2000**, *104*, 12365.

(103) Yoshizawa, K. *Coord. Chem. Rev.* **2002**, *226*, 251.

(104) Kamachi, T.; Yoshizawa, K. *J. Am. Chem. Soc.* **2003**, *125*, 4652.

(105) Kamachi, T.; Shiota, Y.; Ohta, T.; Yoshizawa, K. *Bull. Chem. Soc. Jpn.* **2003**, *76*, 721.

(106) de Visser, S. P.; Ogliaro, F.; Harris, N.; Shaik, S. *J. Am. Chem. Soc.* **2001**, *123*, 3037.

(107) de Visser, S. P.; Ogliaro, F.; Shaik, S. *Angew. Chem., Int. Ed.* **2001**, *40*, 2871.

(108) de Visser, S. P.; Ogliaro, F.; Shaik, S. *Chem. Commun.* **2001**, *22*, 2322.

(109) de Visser, S. P.; Shaik, S. *J. Am. Chem. Soc.* **2003**, *125*, 7413.

(110) (a) Bathelt, C. M.; Ridder, L.; Mulholland, A. J.; Harvey, J. N. *J. Am. Chem. Soc.* **2003**, *125*, 15004. (b) Bathelt, C. M.; Ridder, L.; Mulholland, A. J.; Harvey, J. N. *Org. Biomol. Chem.* **2004**, *2*, 2998.

(111) Sharma, P. K.; de Visser, S. P.; Shaik, S. *J. Am. Chem. Soc.* **2003**, *125*, 8698.

(112) Ogliaro, F.; de Visser, S. P.; Cohen, S.; Kaneti, J.; Shaik, S. *ChemBioChem.* **2001**, *2*, 848.

(113) Davydov, R.; Makris, T. M.; Kofman, V.; Werst, D. E.; Sligar, S. G.; Hoffman, B. M. *J. Am. Chem. Soc.* **2001**, *123*, 1403.

(114) Mueller, E. J.; Loida, P. J.; Sligar, S. G. Twenty-five years of P450cam research. In *Cytochrome P450: structure, mechanism and biochemistry,* 2nd ed.; Ortiz de Montellano, P. R., Ed.; Plenum Press: New York, 1995; Chapter 3, p 83.

(115) Dawson, J. H.; Holm, R. H.; Trudell, J. R.; Barth, G.; Linder, R. E.; Bunnenberg, E.; Djerassi, C.; Tang, S. C. *J. Am. Chem. Soc.* **1976**, *98*, 3707.

(116) Vidakovic, M.; Sligar, S. G.; Li, H.; Poulos, T. L. *Biochemistry* **1998**, *37*, 9211.

(117) Raag, R.; Martinis, S. A.; Sligar, S. G.; Poulos, T. L. *Biochemistry* **1991**, *30*, 11420.

(118) Bell, S. G.; Sowden, R. J.; Wong, L.-L. *Chem. Commun.* **2001**, *7*, 635.

(119) Atkins, W. M.; Sligar, S. G. *J. Biol. Chem.* **1988**, *263*, 18842.

(120) Suzuki, N.; Higuchi, T.; Urano, Y.; Kikuchi, K.; Uekusa, H.; Ohashi, Y.; Uchida, T.; Kitagawa, T.; Nagano, T. *J. Am. Chem. Soc.* **1999**, *121*, 11571.

(121) Yoshioka, S.; Takahashi, S.; Ishimori, K.; Morishima, I. *J. Inorg. Biochem.* **2000**, *81*, 141.

(122) Ogliaro, F.; Cohen, S.; Filatov, M.; Harris, N.; Shaik, S. *Angew. Chem., Int. Ed.* **2000**, *39*, 3851.

(123) de Visser, S. P.; Shaik, S.; Sharma, P. K.; Kumar, D.; Thiel, W. *J. Am. Chem. Soc.* **2003**, *125*, 15779.

(124) Thomann, H.; Bernardo, M.; Goldfarb, D.; Kroneck, P. M. H.; Ullrich, V. *J. Am. Chem. Soc.* **1995**, *117*, 8243.

(125) Harris, D. L.; Loew, G. H. *J. Am. Chem. Soc.* **1993**, *115*, 5799.

(126) Aissaoui, H.; Bachmann, R.; Schweiger, A.; Woggon, W.-D. *Angew. Chem., Int. Ed. Engl.* **1998**, *37*, 2998.

(127) Green, M. T. *J. Am. Chem. Soc.* **1998**, *120*, 10772.

(128) Tsai, R.; Yu, C. A.; Gunsalus, I. C.; Peisach, J.; Blumberg, W.; Orme-Johnson, W. H.; Beinert, H. *Proc. Natl. Acad. Sci. U.S.A.* **1970**, *66*, 1157.
(129) Sharrock, M.; Debrunner, P. G.; Schulz, C.; Lipscomb, J. D.; Marshall, V.; Gunsalus, I. C. *Biochim. Biophys. Acta* **1976**, *420*, 8.
(130) Sligar, S. G. *Biochemistry* **1976**, *15*, 5399.
(131) Filatov, M.; Harris, N.; Shaik, S. *J. Chem. Soc., Perkin Trans. 2* **1999**, *3*, 399.
(132) (a) de Visser, S. P.; Kumar, D.; Cohen, S.; Sharma, P. K.; Shaik, S.; Thiel, W. *Proton-relay mechanisms in the catalytic cycle of P450*. Unpublished results. (b) Kumar, D.; de Visser, S. P.; Thiel, W.; Shaik, S. Submitted for publication. See also Supporting Information for this paper.
(133) Reiher, M.; Salomon, O.; Hess, B. A. *Theor. Chem. Acc*. **2001**, *107*, 48.
(134) Salomon, O.; Reiher, M.; Hess, B. A. *J. Chem. Phys.* **2002**, *117*, 4729.
(135) Scherlis, D. A.; Cymeryng, C. B.; Estrin, D. A. *Inorg. Chem.* **2000**, *39*, 2352.
(136) Scherlis, D. A.; Martí, M. A.; Ordejón, P.; Estrin, D. A. *Int. J. Quantum Chem.* **2002**, *90*, 1505.
(137) Auclair, K.; Moënne-Loccoz, P.; Ortiz de Montellano, P. R. *J. Am. Chem. Soc.* **2001**, *123*, 4877.
(138) Champion, P. M.; Lipscomb, J. D.; Munck, E.; Debrunner, P. G.; Gunsalus, I. C. *Biochemistry* **1975**, *14*, 4151.
(139) See Supporting Information to ref 88 for effects of the basis set, etc.
(140) Debrunner, P. G. In *Iron Porphyrins Part 3: Physical Bioinorganic Chemistry Series*; Lever, A. B. P., Gray, H. B., Eds.; VCH: New York, 1989; Vol. 4, Chapter 2.
(141) Reiss, H.; Heller, A. *J. Phys. Chem.* **1985**, *89*, 4207.
(142) Olsson, M. H.; Hong, G.; Warshel, A. *J. Am. Chem. Soc.* **2003**, *125*, 5025.
(143) Li, G. Zhang, X.; Cui, Q. *J. Phys. Chem. B* **2003**, *107*, 8643.
(144) Makris, T.; Denisov, I.; Schlichting, I.; Sligar, S. G. *Activation of Molecular Oxygen by Cytochrome P450*. In *Cytochrome P450: structure, mechanism and biochemistry*, 3rd ed.; Ortiz de Montellano, P. R., Ed.; Kluwer Academic/Plenum Publishers: New York, 2004; Chapter 5, p 151.
(145) Harris, D. L.; Loew, G. H. *J. Am. Chem. Soc.* **1998**, *120*, 8941.
(146) Harris, D. L.; Loew, G. H.; Waskell, L. *J. Am. Chem. Soc.* **1998**, *120*, 4308.
(147) Chottard, G.; Schappacher, M.; Ricard, L.; Weiss, R. *Inorg. Chem.* **1984**, *23*, 4557.
(148) Jensen, K. P.; Ryde, U. *J. Biol. Chem.* **2004**, *279*, 14561.
(149) Harris, D. L.; Loew, G. H. *J. Am. Chem. Soc.* **1994**, *116*, 11671.
(150) Harris, D. L.; Loew, G. H. *J. Am. Chem. Soc.* **1996**, *118*, 6377.
(151) Guallar, V.; Harris, D. L.; Batista, V. S.; Miller, W. H. *J. Am. Chem. Soc.* **2002**, *124*, 1430.
(152) Harris, D. L. *J. Inorg. Biochem.* **2002**, *91*, 568.
(153) Aikens, J.; Sligar, S. G. *J. Am. Chem. Soc.* **1994**, *116*, 1143.
(154) Taraphder, S.; Hummer, G. *J. Am. Chem. Soc.* **2003**, *125*, 3931.
(155) Kimata, Y.; Shimada, H.; Hirose, T.; Ishimura, Y. *Biochem. Biophys. Res. Commun.* **1995**, *208*, 96.
(156) Kellner, D. G.; Hung, S. C.; Weiss, K. E.; Sligar, S. G. *J. Biol. Chem.* **2002**, *277*, 9641.
(157) Denisov, I. G.; Makris, T. M.; Sligar, S. G. *J. Biol. Chem.* **2001**, *276*, 11648.
(158) (a) Egawa, T.; Shimada, H.; Ishimura, Y. *Biophys. Biochem. Res. Commun.* **1994**, *201*, 1464. (b) Hishiki, T.; Shimada, H.; Nagano, S.; Egawa, T.; Kanamori, Y.; Makino, R.; Park, S. Y.; Adachi, S. I.; Shiro, Y.; Ishimiura, Y. *J. Biochem.* **2000**, *128*, 965.
(159) Dowers, T. S.; Rock, D. A.; Jones, J. P. *J. Am. Chem. Soc.* **2004**, *126*, 8868.
(160) Hata, M.; Hoshino, T.; Tsuda, M. *Chem. Commun.* **2000**, *20*, 2037.
(161) Hata, M.; Hirano, Y.; Hoshino, T.; Tsuda, M. *J. Am. Chem. Soc.* **2001**, *123*, 6410.
(162) Du, P.; Axe, F. U.; Loew, G. H.; Canuto, S.; Zerner, M. C. *J. Am. Chem. Soc.* **1991**, *113*, 8614.
(163) Jung, C. *J. Mol. Recognit.* **2000**, *13*, 325.
(164) Jung, C. *Biochim. Biophys. Acta* **2002**, *1595*, 309.
(165) Meilleur, F.; Contzen, J.; Myles, D. A. A.; Jung, C. *Biochemistry* **2004**, *43*, 8744.
(166) Nam, W.; Lee, H. J.; Oh, S.-Y.; Kim, C.; Jang, H. G. *J. Inorg. Biochem*. **2000**, *80*, 219.
(167) Nam, W.; Park, S.-E.; Kim, I. K.; Lim, M. H.; Hong, J.; Kim, J. *J. Am. Chem. Soc*. **2003**, *125*, 14674.
(168) Kaizer, J.; Klinker, E. J.; Oh, N. Y.; Rohde, J.-U.; Song, W. J.; Stubna, A.; Kim, J.; Münck, E.; Nam, W.; Que, L., Jr. *J. Am. Chem. Soc.* **2004**, *126*, 472.
(169) Harris, D. L.; Loew, G. H.; Waskell, L. *J. Inorg. Biochem.* **2001**, *83*, 309.
(170) Filatov, M.; Harris, N.; Shaik, S. *Angew. Chem., Int. Ed. Engl.* **1999**, *38*, 3510.
(171) Ogliaro, F.; de Visser, S. P.; Groves, J. T.; Shaik, S. *Angew. Chem., Int. Ed.* **2001**, *40*, 2874.
(172) Antony, J.; Grodzicki, M.; Trautwein, A. X. *J. Phys. Chem. A* **1997**, *101*, 2692.
(173) Green, M. T. *J. Am. Chem. Soc.* **1999**, *121*, 7939.
(174) Green, M. T. *J. Am. Chem. Soc.* **2000**, *122*, 9495.
(175) Green, M. T. *J. Am. Chem. Soc.* **2001**, *123*, 9218.
(176) Ohta, T.; Matsuura, K.; Yoshizawa, K.; Morishima, I. *J. Inorg. Biochem.* **2000**, *82*, 141.
(177) Ogliaro, F.; Cohen, S.; de Visser, S. P.; Shaik, S. *J. Am. Chem. Soc.* **2000**, *122*, 12892.
(178) Rutter, R.; Hager, L. P.; Dhonau, H.; Hendrich, M.; Valentine, M.; Debrunner, P. *Biochemistry* **1984**, *23*, 6809.
(179) Cohen, S. Ph.D. Thesis, Hebrew University of Jerusalem, Israel, in preparation.
(180) de Visser, S. P.; Ogliaro, F.; Gross, Z.; Shaik, S. *Chem. Eur. J.* **2001**, *7*, 4954.
(181) Sharma, P. K.; de Visser, S. P.; Ogliaro, F.; Shaik, S. *J. Am. Chem. Soc.* **2003**, *125*, 2291.
(182) Kuramochi, H.; Noodleman, L.; Case, D. A. *J. Am. Chem. Soc.* **1997**, *119*, 11442.
(183) Deeth, R. J. *J. Am. Chem. Soc.* **1999**, *121*, 6074.
(184) Wirstam, M.; Blomberg, M. R. A.; Siegbahn, P. E. M. *J. Am. Chem. Soc.* **1999**, *121*, 10178.
(185) Green, M. T.; Dawson, J. D.; Gray, H. B. *Science* **2004**, *304*, 1653.
(186) Miyahara, T.; Tokita, Y.; Nakatsuji, H. *J. Phys. Chem. B* **2001**, *105*, 7341.
(187) Ghosh, A.; Wondimagegn, T. *J. Am. Chem. Soc.* **2000**, *122*, 8101.
(188) Wondimagegn, T.; Ghosh, A. *J. Am. Chem. Soc.* **2001**, *123*, 5680.
(189) Jensen, K. P.; Ryde, U. *Mol. Phys.* **2003**, *101*, 2003.
(190) Ghosh, A. *Acc. Chem. Res.* **1998**, *31*, 189.
(191) Ghosh, A.; Almlöf, J.; Que, L., Jr. *J. Phys. Chem.* **1994**, *98*, 5576.
(192) Cheng, R.-J.; Chen, P.-Y.; Lovell, T.; Liu, T.; Noodleman, L.; Case, D. A. *J. Am. Chem. Soc.* **2003**, *125*, 6774.
(193) Ghosh, A.; Gonzalez, E. *Isr. J. Chem.* **2000**, *40*, 1.
(194) Jensen, K. P.; Ryde, U. *ChemBioChem.* **2003**, *4*, 413.
(195) Vaz, A. D. N.; McGinnity, D. F.; Coon, M. J. *Proc. Natl. Acad. Sci. U.S.A.* **1998**, *95*, 3555.
(196) Newcomb, M.; Toy, P. H. *Acc. Chem. Res.* **2000**, *33*, 449.
(197) Jin, S.; Makris, T. M.; Bryson, T. A.; Sligar, S. G.; Dawson, J. H. *J. Am. Chem. Soc.* **2003**, *125*, 3406.
(198) Groves, J. T. *Proc. Natl. Acad. Sci. U.S.A.* **2003**, *100*, 3569.
(199) Groves, J. T.; McClusky, G. A. *J. Am. Chem. Soc.* **1976**, *98*, 859.
(200) Ortiz de Montellano, P. R.; Stearns, R. A. *J. Am. Chem. Soc.* **1987**, *109*, 3415.
(201) Newcomb, M.; Shen, R.; Choi, S.-Y.; Toy, P. H.; Hollenberg, P. F.; Vaz, A. D. N.; Coon, M. J. *J. Am. Chem. Soc.* **2000**, *122*, 2677.
(202) Shaik, S.; de Visser, S. P.; Kumar, D. *J. Biol. Inorg. Chem.* **2004**, *9*, 661.
(203) Shaik, S.; Filatov, M.; Schröder, D.; Schwarz, H. *Chem. Eur. J.* **1998**, *4*, 193.
(204) Schröder, D.; Shaik, S.; Schwarz, H. *Acc. Chem. Res.* **2000**, *33*, 139.
(205) de Visser, S. P.; Kumar, D.; Shaik, S. *J. Inorg. Biochem.* **2004**, *98*, 1183.
(206) Sevin, A.; Fontecave, M. *J. Am. Chem. Soc.* **1986**, *108*, 3266.
(207) Harris, N.; Cohen, S.; Filatov, M.; Ogliaro, F.; Shaik, S. *Angew. Chem., Int. Ed.* **2000**, *39*, 2003.
(208) (a) Altun, A.; Cohen, S.; Friesner, R. A.; Guallar, V.; Shaik, S.; Thiel, W. Unpublished work, 2004. (b) Guallar, V. Private communication.
(209) Truhlar, D. G.; Gao, J.; Alhambra, C.; Garcia-Viloca, M.; Corchado, J.; Sanchez, M. L.; Villa, J. I. *Acc. Chem. Res*. **2002**, *35*, 341.
(210) Gelb, M. H.; Heimbrook, D. C.; Malkonen, P.; Sligar, S. G. *Biochemistry* **1982**, *21*, 370.
(211) Groves, J. T.; McClusky, G. A.; White, R. E.; Coon, M. J. *Biochem. Biophys. Res. Commun.* **1978**, *81*, 154.
(212) Li, H.; Narasimhulu, S.; Havran, L. M.; Winkler, J. D.; Poulos, T. L. *J. Am. Chem. Soc.* **1995**, *117*, 6297.
(213) Newcomb, M.; Aebisher, D.; Shen, R.; Chandrasena, R. E. P.; Hollenberg, P. F.; Coon, M. J. *J. Am. Chem. Soc.* **2003**, *125*, 6064.
(214) Melander, L.; Saunders, W. H., Jr. In *Reaction rates of isotopic molecules;* Robert E. Krieger Publishing Co.: Malabar, FL, 1987.
(215) Audergon, C.; Iyer, K. R.; Jones, J. P.; Darbyshire, J. F.; Trager, W. F. *J. Am. Chem. Soc.* **1999**, *121*, 41.
(216) Mayer, J. M. *Acc. Chem. Res.* **1998**, *31*, 441.
(217) Mayer, J. M. In *Biomimetic Oxidations Catalyzed by Transition Metal Complexes;* Meunier, B., Ed.: Imperial College Press: London, 1999; p 1.
(218) Shaik, S.; Shurki, A. *Angew. Chem., Int. Ed. Engl.* **1999**, *38*, 586.
(219) Korzekwa, K. R.; Jones, J. P.; Gillette, J. R. *J. Am. Chem. Soc.* **1990**, *112*, 7042.
(220) Park, J.-Y.; Harris, D. L. *J. Med. Chem.* **2003**, *46*, 1645.
(221) Zhang, R.; Newcomb, M. *J. Am. Chem. Soc.* **2003**, *125*, 12418.
(222) Brewer, C. B.; Peterson, J. A. *J. Biol. Chem.* **1988**, *263*, 791.
(223) Guengerich, F. P.; Brian, W. R.; Iwasaki, M.; Sari, M.-A.; Bäärnhielm, C.; Berntsson, P. *J. Med. Chem.* **1991**, *34*, 1838.
(224) Guengerich, F. P. *Chem. Res. Toxicol.* **2001**, *14*, 611.
(225) Rettie, A. E.; Boberg, M.; Rettenmeire, A. W.; Baillie, T. A. *J. Biol. Chem.* **1988**, *263*, 13733.

(226) Lee, J. S.; Jacobsen, N. E.; Ortiz de Montellano, P. R. *Biochemistry*, **1988**, *27,* 7703.

(227) Lee, H.; Ortiz de Montellano, P. R.; McDermott, A. E. *Biochemistry* **1999**, *38*, 10808.

(228) Wand, M. D.; Thompson, J. A. *J. Biol. Chem.* **1986**, *261*, 14049.

(229) Atkins, W. M.; Sligar, S. G. *J. Am. Chem. Soc.* **1987**, *109*, 3754.

(230) Guengerich, F. P.; MacDonald, T. L. *Acc. Chem. Res*. **1984**, *17*, 9.

(231) Groves, J. T.; Gross, Z.; Stern, M. K. *Inorg. Chem.* **1994**, *33*, 5065.

(232) Groves, J. T.; Nemo, T. E. *J. Am. Chem. Soc.* **1983**, *105*, 5786.

(233) Gross, Z.; Nimri, S.; Barzilay, C. M.; Simkhovich, L. *J. Biol. Inorg. Chem.* **1997**, *2*, 492.

(234) Kumar, D.; de Visser, S. P.; Shaik, S. *Chem.—Eur. J.*, published online Mar 2, http://dx.doi.org/10.1002/chem.200401044.

(235) Groves, J. T.; Ahn, K.-H.; Quinn, R. *J. Am. Chem. Soc.* **1988**, *110*, 4217.

(236) Korzekwa, K. R.; Swinney, D. C.; Trager, W. F. *Biochemistry* **1989**, *28*, 9019.

(237) Rietjens, I. M. C. M.; Soffers, A. E. M. F.; Veeger, C.; Vervoort, J. *Biochemistry* **1993**, *32*, 4801.

(238) Kumar, D.; de Visser, S. P.; Sharma, P. K.; Hirao, H.; Shaik, S. *Biochemistry*, submitted for publication.

(239) Volz, T. J.; Rock, D. A.; Jones, J. P. *J. Am. Chem. Soc.* **2002**, *124*, 9724.

(240) Goto, Y.; Matsui, T.; Ozaki, S.-I.; Watanabe, Y.; Fukuzumi, S. *J. Am. Chem. Soc.* **1999**, *121*, 9497.

(241) Shaik, S.; de Visser, S. P.; Kumar, D. *J. Am. Chem. Soc.* **2004**, *126*, 11746.

(242) Groves, J. T.; Avaria-Neisser, G. E.; Fish, K. M.; Imachi, M.; Kuczkowski, R. L. *J. Am. Chem. Soc.* **1986**, *108*, 3837.

(243) Groves, J. T.; Subramanian, D. V. *J. Am. Chem. Soc.* **1984**, *106*, 2177.

(244) Sharma, P. K.; Kevorkiants, R.; de Visser, S. P.; Kumar, D.; Shaik, S. *Angew. Chem., Int. Ed.* **2004**, *43*, 1129.

(245) Kamachi, T.; Shestakov, A. F.; Yoshizawa, K. *J. Am. Chem. Soc.* **2004**, *126*, 3672.

(246) Lewis, D. F. V.; Craig, S.; Loizou, G. D. *J. Biochem. Mol. Toxicol.* **2003**, *17*, 47.

(247) For recent experimental support of TSR, see: (a) Cryle, M. J.; Stuthe, J. M. U.; Ortiz de Montellano, P. R.; de Voss, J. J. *Chem. Commun.* **2004**, 512. (b) He, X.; Ortiz de Montellano, P. R. *J. Biol. Chem.* **2004**, *279,* 39479.

CR030722J